SLAC-PUB-1330
(T/E)
October 1973

DIFFRACTIVE PROCESSES*

David W. G. S. Leith

Stanford Linear Accelerator Center
Stanford University, Stanford, Calif. 94305

ABSTRACT

New data on diffractive processes from current experiments at NAL and the ISR is reviewed.

(Invited paper presented at the 1973 Meeting of the Division of Particles and Fields of the APS, Berkeley, California, August 13-17, 1973).

* Work supported by the U.S. Atomic Energy Commission.

INTRODUCTION

Let us briefly review some ideas on diffraction phenomena,[1] and then examine the new data presented to this meeting.

There are two pictures of diffraction in high energy particle scattering: an s-channel picture in which the process is seen in geometric terms, where the incident particle is scattered by an absorbing disc of a given radius and a given opacity — here the diffraction scattering is seen as the shadow of all the inelastic processes; a t-channel picture in which the scattering is mediated by the exchange of a Regge trajectory — the Pomeron, where properties are given by the energy dependence of the total cross-section and the slope of the forward differential cross-section. The trajectory is usually written

$$\alpha(t) \doteq \alpha(0) + \alpha' t$$

The flat asymptotic s-dependence of the total cross-section implies $\alpha(0) = 1$, and the shrinkage of the forward differential cross-section gives $\alpha' \sim 1/3$. The Pomeron trajectory has no known particle associated with it. In all the above properties the Pomeron is quite different from the other known Regge trajectories.

Beyond these pictures we have no good theoretical description of the dynamics of diffractive processes and we rather identify diffractive reactions as those which obey some or all of the following set of empirical rules.

1. Energy independent cross sections (to factors of log s).
2. Sharp forward peak in $d\sigma/dt$.
3. Particle cross sections equal to anti-particle cross sections.
4. Factorization.
5. Mainly imaginary amplitude.
6. exchange processes characterized by the quantum numbers of the vacuum in the t-channel (i.e., I=0, C= +1). Also, the change in parity in the scattering process follows the natural spin-parity series $(-1)^J$, or $P_f = P_i \cdot (-1)^{\Delta J}$, where ΔJ is spin change.
7. The spin structure in the scattering is s-channel helicity conserving (SCHC).

The diffraction phenomenon may be studied in the following processes:

AB → AB — elastic scattering, and through the optical theorem the total cross section

*Work supported in part by the U. S. Atomic Energy Commission.

$AB \rightarrow \begin{matrix} A^*B \\ AB^* \end{matrix}$ — diffraction dissociation

$AB \rightarrow \begin{matrix} AX \\ XB \end{matrix}$ — inclusive scattering

Let us now examine the new data presented to this meeting on these various diffractive reactions.

TOTAL CROSS-SECTION AND ELASTIC SCATTERING

A. Total Cross-Section in pp Collisions

Up through 30 GeV all the measured total cross-sections appeared to have an energy dependence of the form $a + b\ s^{-1/2}$. However, measurements through the Serpukov energy range, (20-70) GeV, showed most of the cross-sections flattening out, (pp, $\pi^{\pm}p$, K^-p), and the K^+p cross-section actually rising by almost 2 mb. These data are summarized in Fig. 1.

About a year ago we had the first indications that the pp total cross-section was rising in the ISR energy region (200-3000 GeV/c equivalent lab momentum). The results are now quite firm and clearly show a 4 mb rise—see Fig. 2. The data came from two groups measuring the pp total cross-sections at the ISR by two quite different methods:

(1) CERN-Rome[2] measure the forward scattering angular distribution $d\sigma/dt$, with a scintillation counter telescope and extrapolate to find the forward cross-section, $\left.\frac{d\sigma}{dt}\right|_{t=0}$. They also measure the real part of the forward scattering amplitude in this energy range and find it small and essentially negligible. From the optical theorem, they can then determine the total cross-section

$$\sigma_T^2 = 16\pi \left.\frac{d\sigma}{dt}\right|_{t=0}$$

This experiment normalizes their total cross-section measurement two ways — (a) internally, by observing the coulomb p-p scattering cross-section, and (b) externally, by using the Van der Meer luminosity measurement of the circulating ISR proton beams. Both methods agree well.

(2) Pisa-Stonybrook[3] measure the reaction rate in pp collisions with an almost 4π counter hodoscope. This experiment is normalized using two external methods — the Van der Meer beam displacement measurement and the actual measurement of the individual beam profiles. Again both methods agree well. Figure 2 shows the most recent measurement by this group at the highest energy of the ISR.

Both experiments agree well on the cross-section rise of $\sim$4 mb through the ISR region. It is interesting to note that the two experiments depend very differently on the luminosity of the ISR

CERN-Rome	$\left.\frac{d\sigma}{dt}\right\|_0 \propto \sigma_T^2 \cdot L$
Pisa-Stonybrook	Rate $\propto \sigma_T \cdot L$

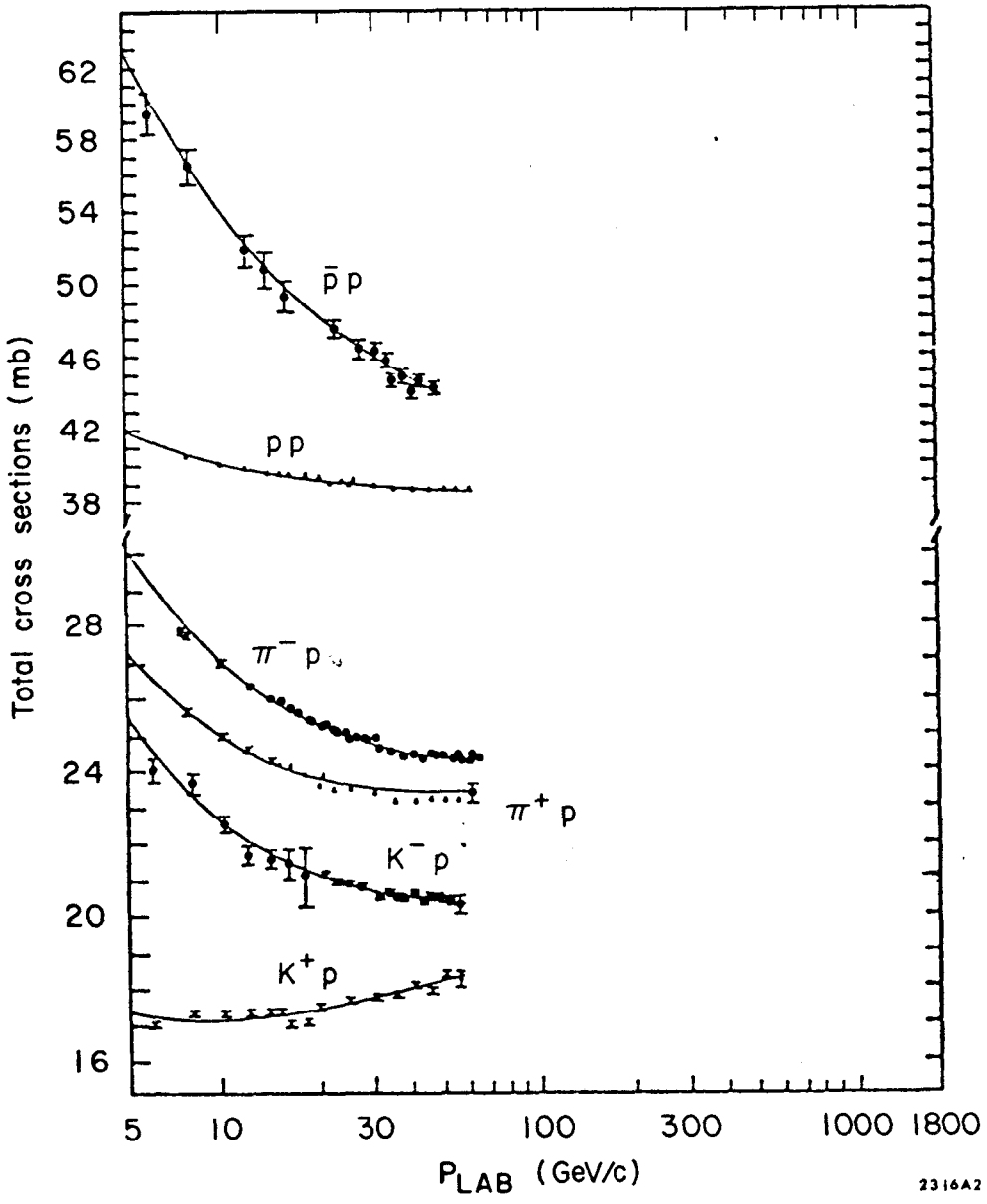

FIG. 1--Energy dependence of the p, $\bar{p}$, $K^{\pm}$, $\pi^{\pm}$ cross-sections on hydrogen.

i.e., the CERN-Rome experiment is sensitive to $\sqrt{L}$, while the Pisa-Stonybrook experiment is sensitive to L. The agreement between the resultant total cross section measurements is evidence that the ISR luminosity has been well measured.

A further interesting comment should be made on the independence of the cross section rise on the ISR luminosity measurements.[4] It is clear from the above discussion that the ratio of the measured quantity in the two ISR experiments is a measure of the total cross-section, completely

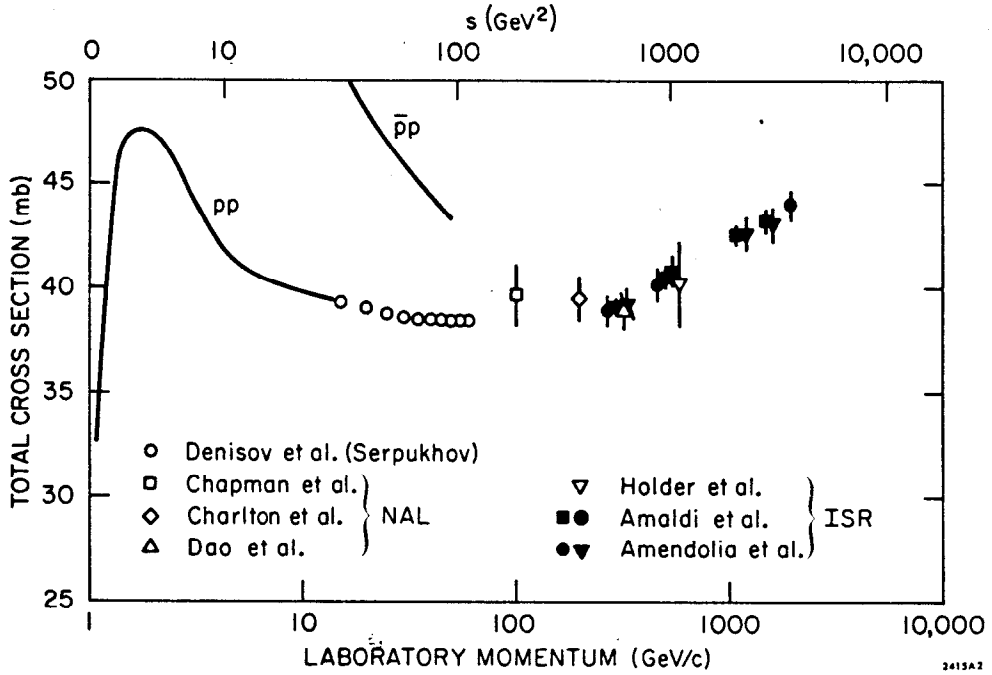

FIG. 2--Energy dependence of the total p-p cross-section.

independent of the luminosity, L.

$$\left[\frac{dt/dt|_{t=0}}{\text{Rate}} \propto \frac{\sigma_T^2 \cdot L}{\sigma_T \cdot L} = \sigma_T\right]$$

Such an experiment is planned in the near future. However, both groups ran for an appreciable time together in obtaining their respective cross-section data. If one assumes that the beam phase space and luminosity does not change round the ISR ring, then we could go through the exercise of taking the ratio of the measured quantities and derive an L-independent measurement of σ_T despite the fact that the experiments were performed in different interaction regions. The result of this interesting exercise is to confirm the detailed systematic measurements — the cross-section rises $\sim$ 3 mb with somewhat larger errors than in the two independent experiments.

In summary, the luminosity measurements seem to be well understood and in good agreement, and the rise in the pp total cross-section an established fact.

The CERN-Rome group[2] have also measured the elastic pp cross-section by integrating out their angular distribution data. They find the elastic cross-section rises by the same fraction as the total cross-section (i.e., $\sim$10%).

In Fig. 3 the total, elastic and inelastic cross-sections are plotted as function of energy.[5] It is interesting to note the inelastic cross-section rises very rapidly at first as new channels open up, and then increases smoothly above 6 GeV/c.

The cross-section data may be fit, through this energy region to $s^{0.04}$, although clearly such an overall energy dependence cannot continue. Thus

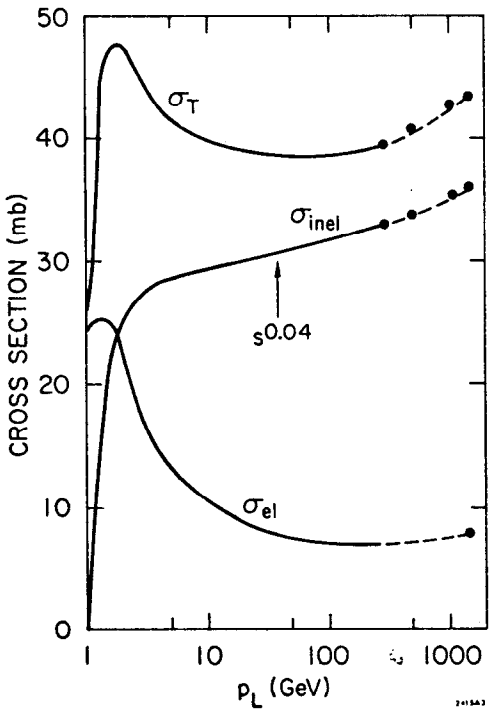

FIG. 3--Energy dependence of the total, elastic and inelastic cross-section for proton-proton collisions.

one could have predicted the increase in the total cross-section from studies of the pp inelastic cross-section at lower energies.

B. Differential Cross-Section in pp Scattering

The forward angular distribution in pp elastic scattering is sharply peaked as expected in a diffractive process, but the recent very accurate measurements at the ISR have shown the presence of some interesting structure, around $t \sim 0.15$ GeV^2.[6]

The small t region ($t < .15$ GeV^2) has been studied by CERN-Rome[7] and ACGHT[6] at ISR and the US-USSR[8] collaboration at NAL. The general conclusion is that this region has a steep slope, (12-13 GeV^{-2}), which shrinks like log s.

The large t region, ($(.2 < t < .5)$ GeV^2), has been studied by the ACGHT group[6] at the ISR. This region has a somewhat flatter angular distribution, (about 2 units flatter than the small t region) and exhibits essentially no energy dependence.

Typical data is shown in Fig. 4. (a) shows data from the highest energy ISR studies of the ACGHT group[6]— the two regions of the scattering distribution are clearly visible. (b) shows data from the US-USSR collaboration[8] at one of the energies in their NAL experiment — this experiment measures entirely in the "small t region" discussed above. Notice in the very forward direction the observation of p-p coulomb scattering.

New results are available on the small t region from CERN-Rome and the NAL collaboration.

There has been much discussion as to whether there really are two distinct regions or whether the slope smoothly decreases as the scattering angle increases. New data from CERN-Rome[7] at $\sqrt{s} = 53$ GeV show that the slope is not continuously changing through the "small t region" but that one value of the slope parameter describes all of the data. If the cross-section within this small t interval is fit with $\frac{d\sigma}{dt} = \left.\frac{d\sigma}{dt}\right|_0 e^{bt}$, then for

$$0.01 < t < 0.06 \text{ GeV}^2, \quad \text{they find} \quad b = 13.1 \pm .3 \text{ GeV}^{-2}$$

$$0.04 < t < 0.16 \text{ GeV}^2, \quad \text{they find} \quad b = 13.0 \pm .3 \text{ GeV}^{-2} .$$

Also the question of the variation of the parameter b as a function of energy has been studied by the US-USSR experiment[8] at NAL. This

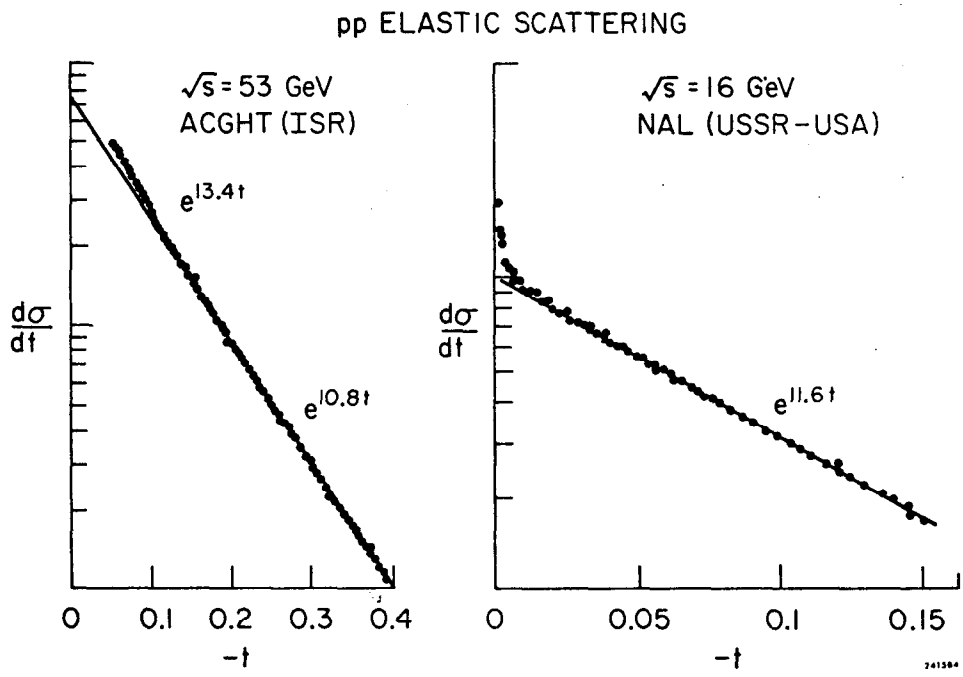

FIG. 4--Differential cross-sections, $d\sigma/dt$, taken at (a) the ISR by the ACGHT group, and (b) at NAL by the US-USSR collaboration.

experiment detects the recoil proton from beam-hydrogen gas jet collisions in an array of solid state counters. The results of this experiment are shown together with existing data for the small t region, in Fig. 5. The slope parameter b varies rapidly at small energy but for $s > 100$ GeV^2 the variation seems to settle down, and is consistent with a logarithmic growth. Fitting to data with $s > 100$ GeV^2 to the form

$$b(s) = b_0 + 2\alpha' \log s$$

the NAL group find

$$b_0 = 8.23 \pm 0.27 \text{ GeV}^2$$

$$\alpha' = 0.278 \pm 0.024 \text{ GeV}^2$$

The ACGHT group[9] have extended their studies of elastic pp scattering out to larger t by using a double arm wire chamber spectrometer with momentum analysis in both arms. This setup provides enough discrimination against the inelastic background that they can follow the cross-section down seven orders of magnitude. The scattering distributions are shown in Fig. 6. The break in the pp scattering cross-section at $t \sim 1.2$ GeV^2 observed at lower energies now becomes a sharp dip. The position of the dip and the height of the second peak are essentially independent of energy and have the properties of a diffractive dip and secondary maximum.

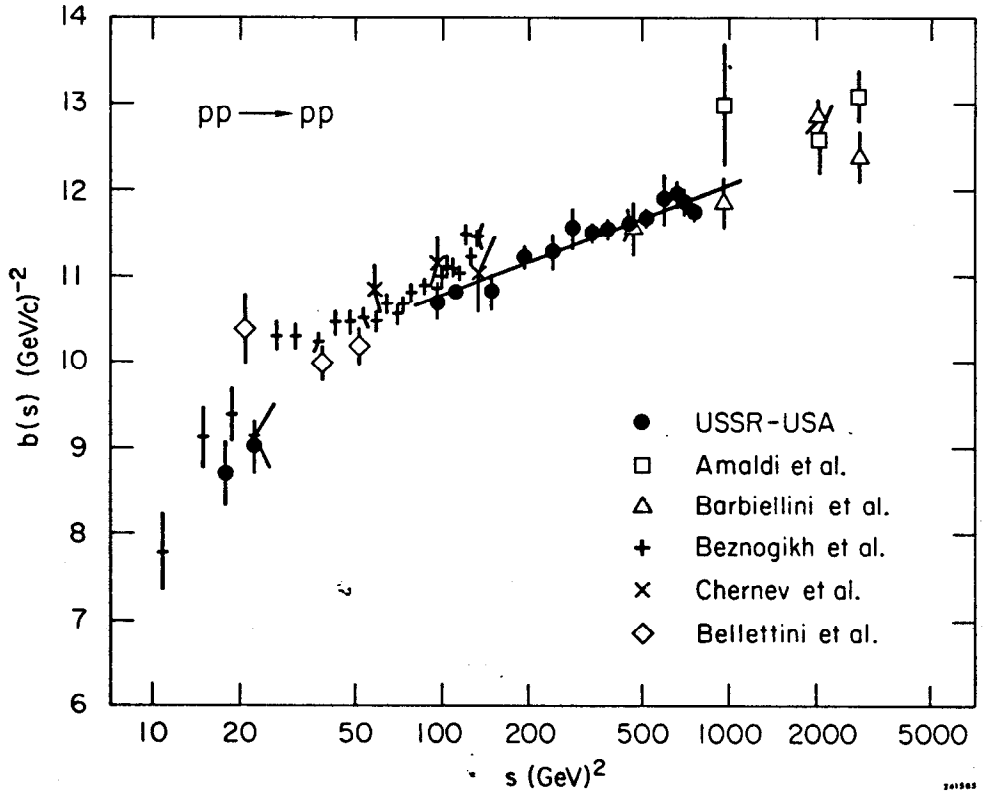

FIG. 5--The energy dependence of the slope of the differential cross-section, $d\sigma/dt$, in p-p elastic scattering.

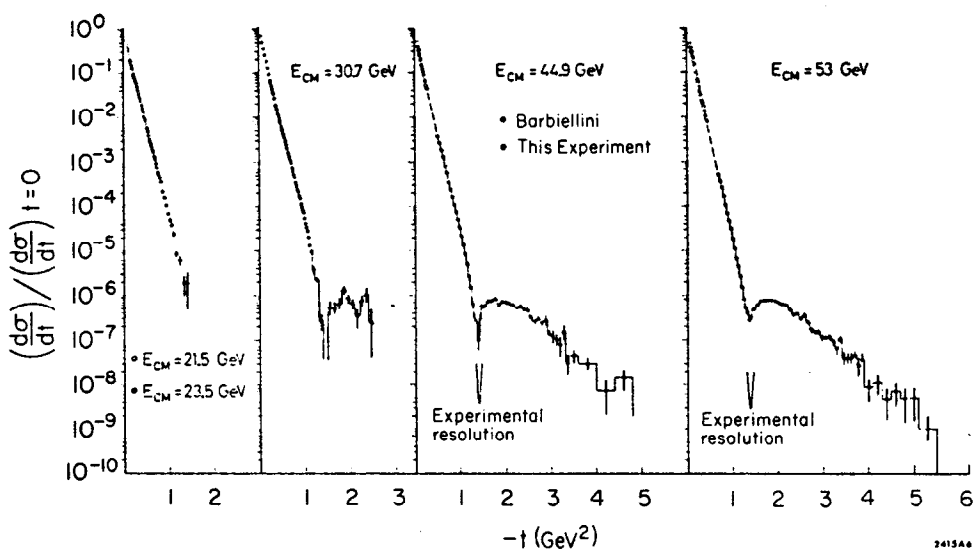

FIG. 6--The differential cross-section, $d\sigma/dt$, in pp elastic scattering out to very large t, as measured by the ACGHT group at the ISR.

These data on the total cross-section and differential cross-section provide an interesting picture of the structure of the proton: the small t data on $d\sigma/dt$ exhibiting the steep slope with fairly rapid shrinkage implies that the outer "shell" of the proton is growing as a function of energy, or more specifically that the radius is growing logarithmically; the large t data on $d\sigma/dt$ imply that the "core" of the proton is rather constant in size showing no appreciable dependence on energy; the total cross-section being very flat in the (20-200) GeV/c region implies a curious compensation between the growing size of the proton and a decreasing opacity, while the high energy rise in the cross-section indicates an end to this compensation with the opacity becoming constant or even increasing slightly with energy.

HIGH ENERGY INCLUSIVE pp SCATTERING

A. Missing Mass Distribution

It has been known for some time that inclusive pp scattering at high energy is characterized by a large quasi-elastic peak which is associated with the diffractive production of high mass states[10] (see Fig. 7). It is interesting to study the energy, mass and momentum transfer dependencies of this process to learn more of the dynamics of diffraction. A considerable amount of new data on this topic has become available recently.

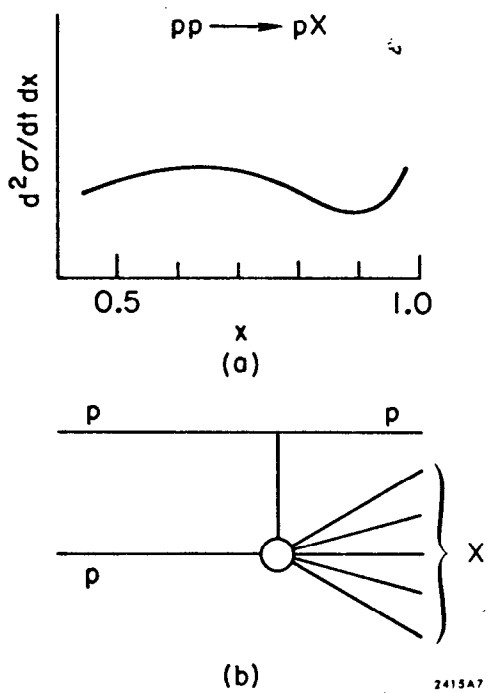

FIG. 7--(a) The invariant cross-section $d^2\sigma/dtdx$, as a function of x, for the process $pp \rightarrow pX$. The cross-section exhibits a large hump for $0.2 < x < .8$ which is characteristic of the multiparticle production region, then a minimum for $0.8 < x < .9$, followed by a sharp peak for $0.9 < x < 1.0$ which is characteristic of diffractive quasi-elastic scattering shown diagrammatically in (b).

In Fig. 8 the missing mass plots from the NAL bubble chamber experiments[11] are given. The HBC pictures are scanned for slow protons which can be identified by their ionisation; for those events so identified the missing mass is then calculated. The lowest masses are seen to be produced with almost constant cross-section between 100 and 400 GeV/c.[12] For larger masses the cross-section is falling almost linearly with energy. An alternative display is in terms of the Feynman x variable, the fractional longitudinal momentum, p_L/p_{max} or $x = (1 - M^2/s)$. The 100 and 400 GeV/c data are shown, plotted as a function of x, in Fig.9.[13] From this plot, we see the cross-section for $x \approx 1$ increasing with energy, as it must if the cross section at small masses is constant in energy. This region is presumably the classical diffraction dissociation region. For $x \sim .6$ to $.8$ region the cross-section scales in x.

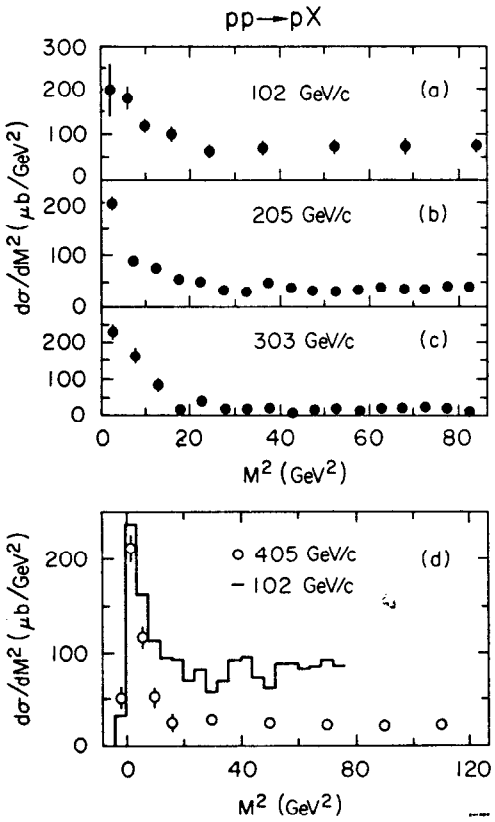

FIG. 8--The missing mass distribution in pp→pX at 100, 200, 300 and 400 GeV/c, as measured in the NAL HBC experiments.

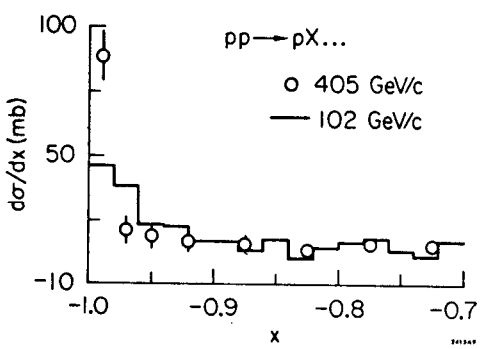

FIG. 9--The invariant cross-section for pp→pX as a function of X for the 100 and 400 GeV/c NAL HBC experiments.

The intermediate region of x ~ .95 seems to show some energy dependence indicating that the quasi-elastic peak does not quite scale in x at these energies.

The 200 GeV/c missing mass data[14] is shown again in Fig. 10 and broken down in the various topological contributions in Fig. 11. The cross-sections in the small mass region (up to masses of 4 GeV), is seen

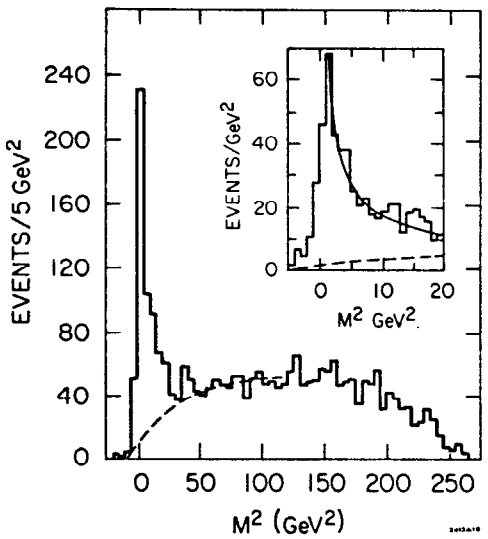

FIG. 10--The missing mass distribution in pp→pX at 200 GeV/c as measured in the NAL HBC experiment.

to fall off like M^{-2} and the diffraction peak is developed by peaks in each of the lower topological cross-sections. It also appears that the mean mass of the diffractive peak increases as the topology or multiplicity, n, increases. The total cross-section of this low mass diffraction peak is estimated at ~6 mb, independent of energy.

The same behavior is observed at ISR energies where the CHLM[10, 15] and ACGHT[16] groups have demonstrated the existence of the low mass diffractive enhancement. In Fig. 12 the missing mass distribution from

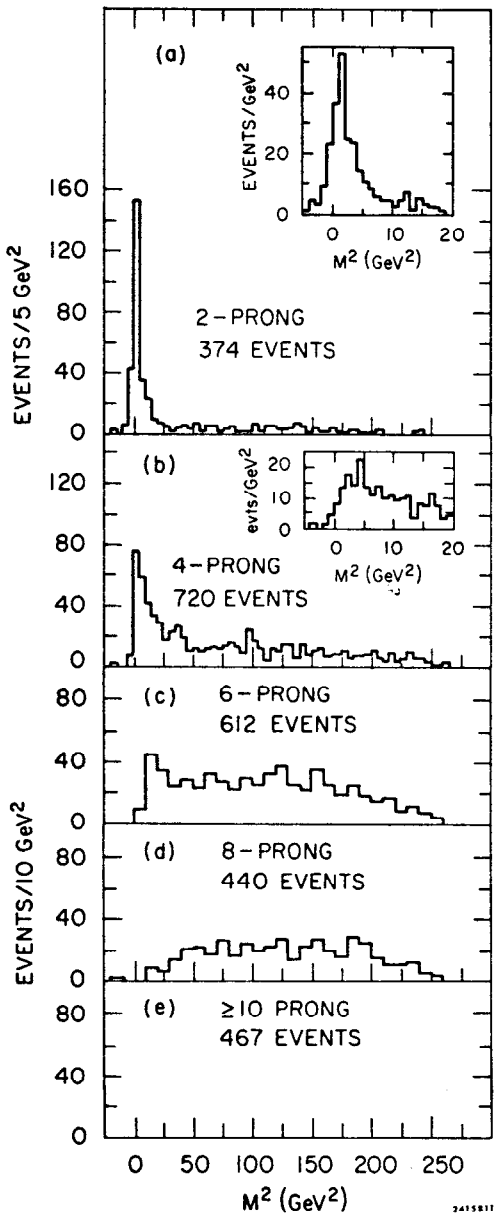

FIG. 11--The missing mass distribution in pp→pX at 200 GeV/c, for each topology, as measured in the 200 GeV/c NAL HBC experiment.

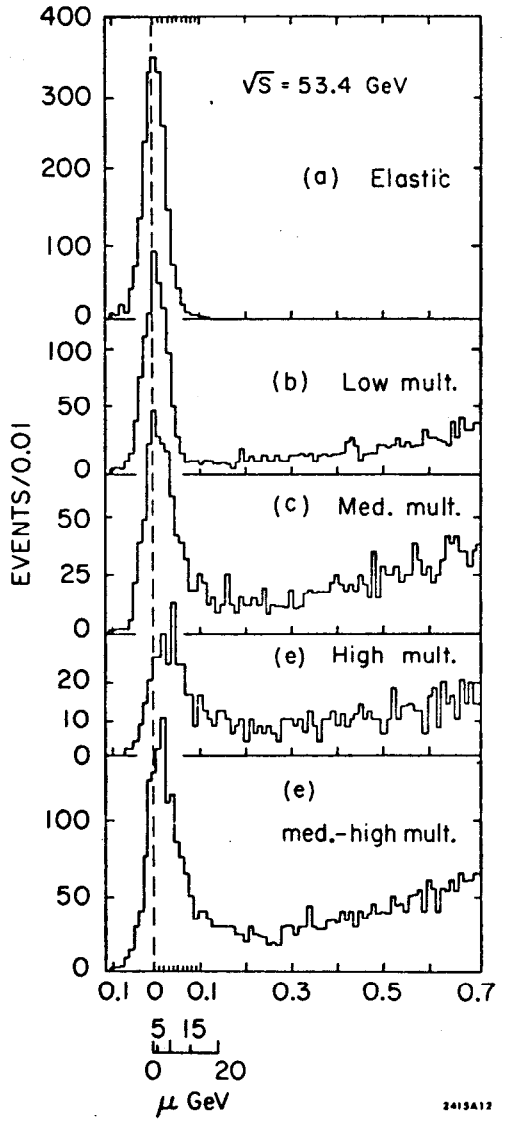

FIG. 12--The missing mass distribution in pp→pX at the ISR, as measured by the ACGHT group.

the two arm spectrometer ACGHT experiment, is shown. They are able to make a rough multiplicity assignment using a scintillation counter hodoscope round the aperture of each spectrometer. There is clear evidence for the increase of mean mass in the diffractive peak as the multiplicity increases.

It is interesting to note that the term "low mass" peak is purely relative and that these diffractive peaks include masses up to 7 GeV.

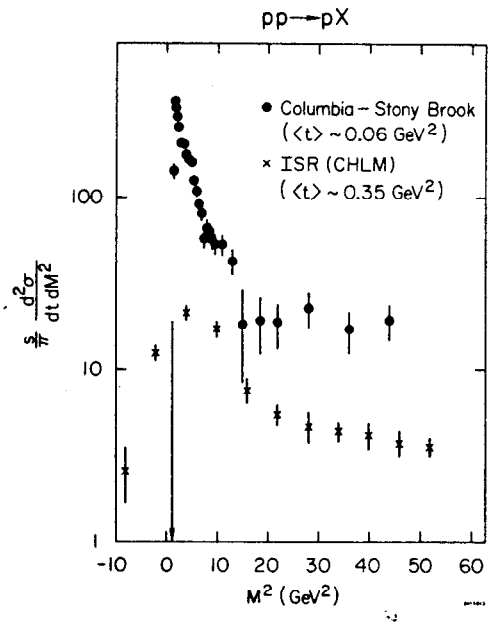

FIG. 13--The missing mass distribution in pp → pX at 300 GeV/c as measured by the Columbia-Stonybrook collaboration.

Figure 13 shows the missing mass spectrum from the Columbia-Stonybrook experiment at NAL.[17] This experiment uses polyethelene and carbon targets and detects the recoil proton in an array of solid state counters. The normalization is effected by counting the d, T, He^3 and He^4 production in both the polyethelene and carbon targets simultaneously with the protons, thus allowing for a very accurate subtraction and hence reliable proton cross-sections.[18] The resolution in missing mass squared is very good, being of order of 1 GeV^2 near $x \sim 1$, whereas the CHLM group has $\delta M^2 \sim 9$ GeV^2 and the ACGHT group has $\delta M^2 \sim 20$ GeV^2. Their missing mass plot shows a very sharp peak with some structure around 3-4 GeV^2 and becoming essentially flat for masses above 16 GeV^2.

This missing mass distribution is quite different from the ISR data. Part of this difference is due to the missing mass resolution of the different experiments, but part is also due to the fact that the measurements have been made at different t values; the ISR experiment has typically $t \sim 0.8$ GeV^2, while the NAL experiment had $t \sim 0.06$ GeV^2. We will come back to this point later.

B. Energy Dependence, or Scaling

The energy dependence of the quasi-elastic pp scattering has been studied at NAL from (50-400) GeV/c by the Rutgers-Imperial College group.[19] The recoil proton is detected and identified in a scintillation counter telescope with a total absorption counter. The momentum of the proton is determined from time of flight measurements over 186 cm flight path.

The invariant cross-section for four different t values is given in Fig. 14 for five energies between 50 and 400 GeV. For x values close to 0.8 there is very little energy dependence, while for x values around 0.9, close to the quasi-elastic peak, quite considerable variation is observed through this energy region. In Fig. 15 the invariant cross-section is plotted against $s^{-1/2}$ for the four t ranges measured, for x values of 0.83 and 0.91. Again substantial s-dependence is clearly visible.

They fit the data to the form

$$s \frac{d2\sigma}{dtdM^2} = A(x)\, e^{b(x)t}\, [1 + B(X)\, s^{-1/2}].$$

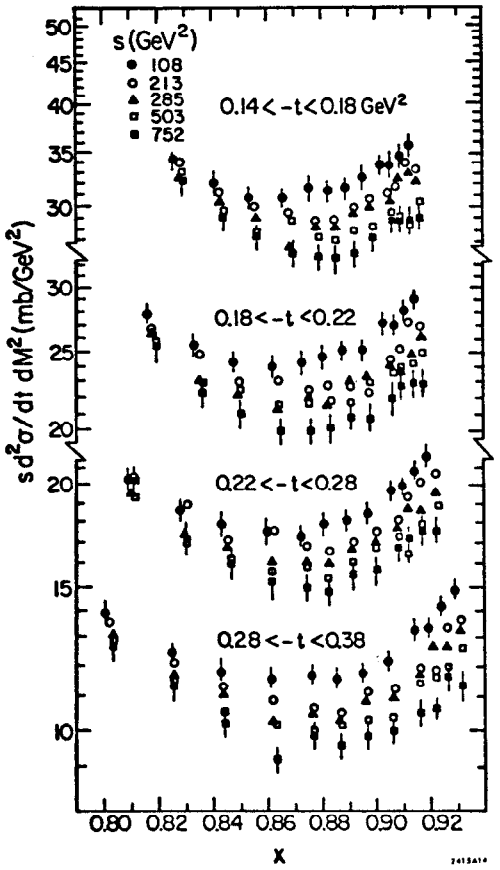

FIG. 14--The invariant cross-section for pp → pX as a function of x, for $100 \leq s \leq 750$ GeV^2, as measured by the Rutgers-Imperial College group. Data is presented in four t intervals.

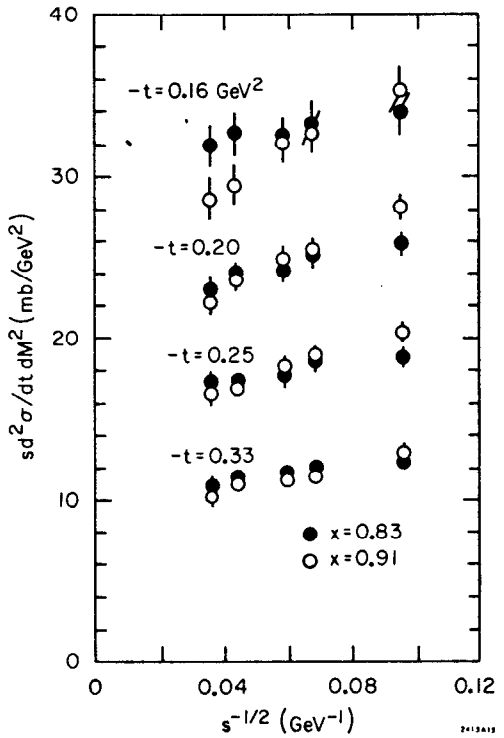

FIG. 15--The invariant cross-section for pp → pX as a function of $s^{-1/2}$ for x = 0.83 and 0.91.

This form represents the data well, with b being essentially independent of x and having a value of ~ 6 GeV^{-2}. The best fit to the data gave

x = 0.83	A = 71 ± 7 mb/GeV^2	B = 1.9 ± .7 GeV
x = 0.91	A = 66 ± 3 mb/GeV^2	B = 4.3 ± .4 GeV

Through the NAL energy range, there is $\sim 20\%$ change in the cross-section for x values near unity, and the fits to the data imply that the variation remaining in the cross-section through the ISR energy range will be less than 10%.

The fall-off in the cross-section for x $\sim$ .95 as measured in the four NAL HBC experiments and discussed above in Fig. 9 is also compatible with this s-dependence.

The experimental results from the CHLM group[15] at the ISR are given in Fig. 16, and show that in this region the cross-section is observed to

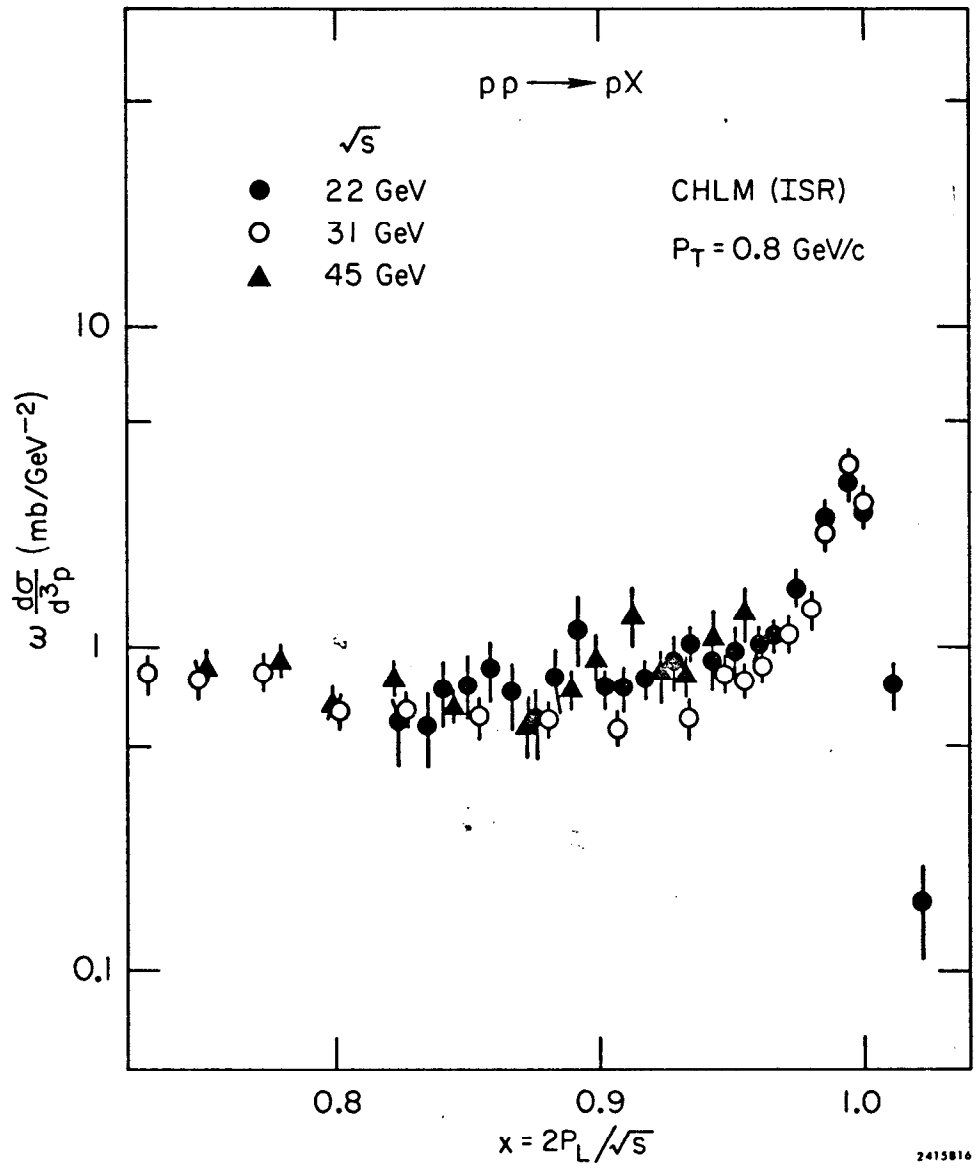

FIG. 16--The invariant cross-section for $pp \rightarrow pX$ as a function of x, for a fixed $P_T = 0.8$ GeV^2. Data comes from the CHLM group at the ISR, for $\sqrt{s} = 22$, 31 and 45 GeV.

scale to within 10%. Note that both the ISR and NAL experiments are performed at intermediate t values.

In summary then, the invariant cross-section $s(d2\sigma/dtdM^2)$ is observed to be almost energy independent for x values of order 0.8 from 50 GeV/c through 2500 GeV/c; for x $\sim$ 0.9 the cross-section is observed to have a component with $s^{-1/2}$ dependence which amounts to a 20% effect through the NAL energy region ((50-400) GeV/c), but which is <10% effect through the ISR range (200-2500 GeV/c).

C. Momentum Transfer Dependence

The momentum transfer dependence of the production of the diffraction peak has been studied at NAL by the bubble chamber experiments[11] and the Columbia-Stonybrook experiment[17] and at the ISR by the CHLM[15] and ACGHT[16] groups.

The t-dependence as a function of the missing mass squared, ($x=1-M^2/s$), is shown in Fig. 17 from the 200 GeV/c HBC experiment.[14] For small masses, the slope of the inelastic diffractive scattering is close to, but a little less than, the elastic scattering slope. As the masses increase,

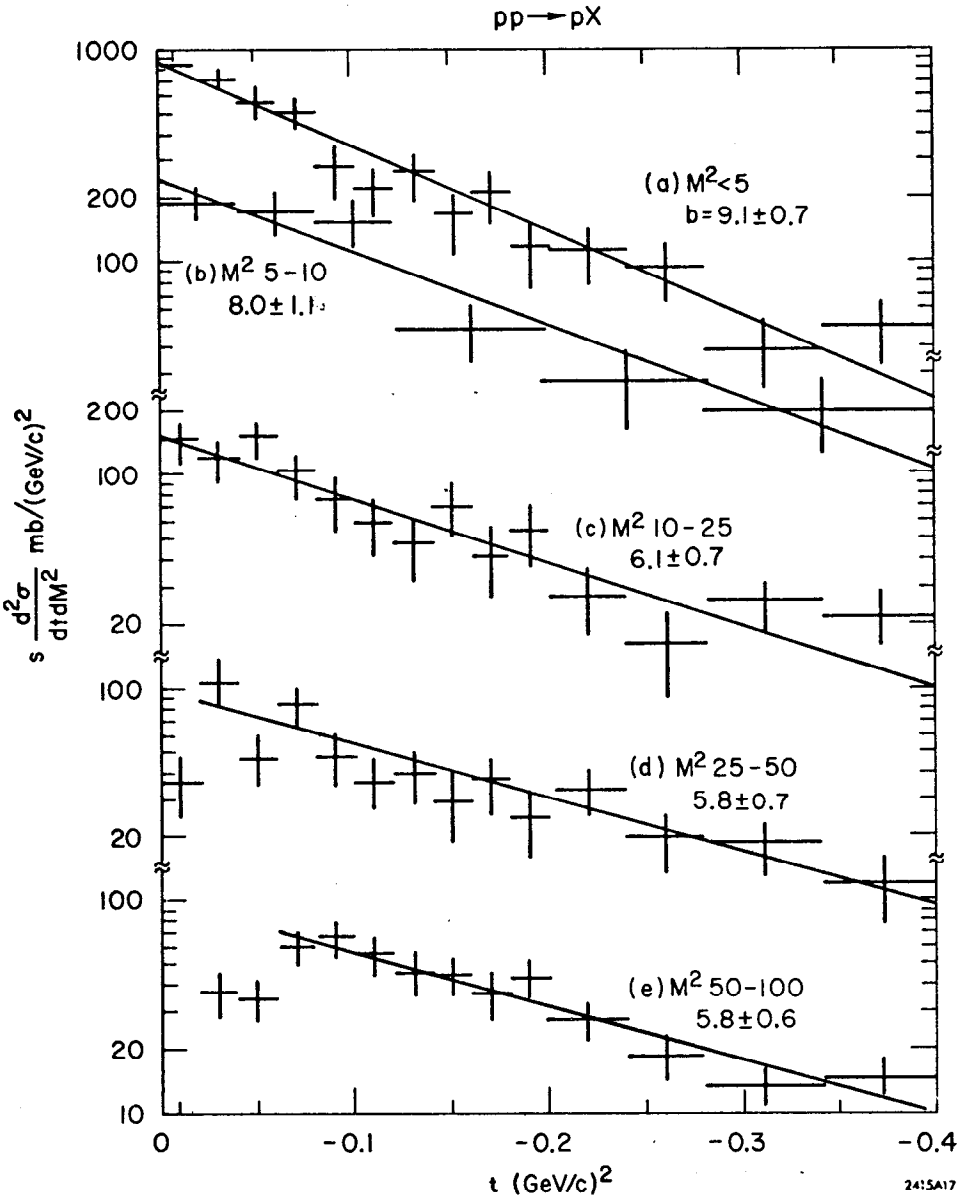

FIG. 17--The differential cross-section, $d\sigma/dt$, for $pp \rightarrow pX$, as a function of the missing mass. Data comes from the 200 GeV/c NAL HBC experiment.

the slope decreases, until one reaches masses corresponding to an x value of ~ 0.9. For masses beyond that there seems to be only a weak M dependence left.

In Fig. 18 the t-dependence of the diffraction peak is shown, from experiments at NAL and the ISR. The cross-section is exponential but with at least two slopes. The dashed line shows a fit which behaves like e^{-7t} at small t and e^{-4t} at large t.

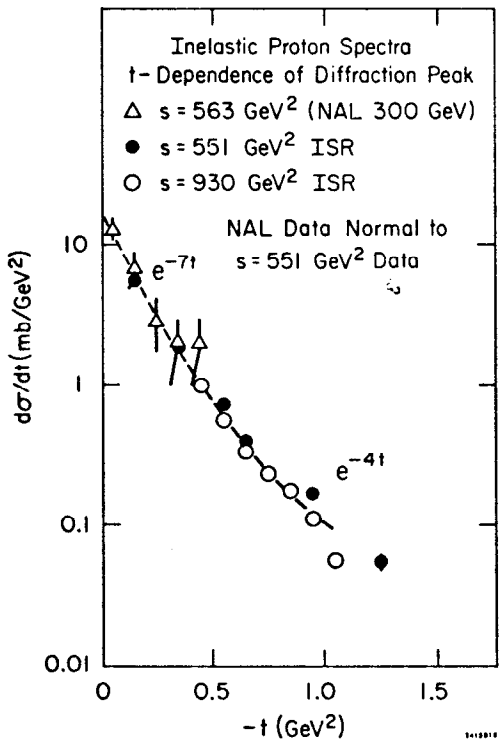

FIG. 18--The t-dependence for the production of the diffraction peak in $pp \rightarrow pX$.

D. Aside on the Missing Mass Distribution

From the above discussion it seems plausible that the differential cross-section, $d\sigma/dt$, is mass dependent. The diffraction peak studied in Fig. 18 contains a wide range of masses (up to $M^2 \sim 50$ GeV^2) and the two exponential shape of that $d\sigma/dt$ may be just a reflection of this mass dependence. Such a dependence would imply that the shape of the missing mass distribution would change for different t values, and perhaps account for some of the difference between the ISR[15, 16] and NAL (Columbia-Stonybrook)[17] mass plots (Fig. 13). Indeed, if one assigns an e^{-7t} dependence to the peak masses, and an e^{-4t} dependence to the large mass region ($M^2 \sim 20$ GeV^2) then quantitative agreement between the measured missing mass distributions results.

Further, if such a dependence exists then the peak to shoulder ratio (low mass to high mass ratio) should be seen to change for measurements at different t. In Fig. 19, 20 the missing mass squared distribution as measured by the CHLM group[15] at the ISR, for four different t ranges is shown. Clear evidence of this effect is observed.

Thus it seems that in fact the different missing mass distributions are in good agreement — there exist three separate regions in the mass plot:

1. The threshold region ($x \approx 1.0$) where the cross-section, $d^2\sigma/dtdx$, is growing linearly with s (i.e., scaling in M^2) and has a steep t dependence;
2. The diffraction peak ($1.0 > x > .9$) where the cross-section is nearly constant in s — some 20% variation in the NAL region (50-400) GeV/c and less than 10% variation at the ISR (200-2500) GeV/c, and with a $d\sigma/dt$ that depends on M^2, becoming flatter as M^2 increases.

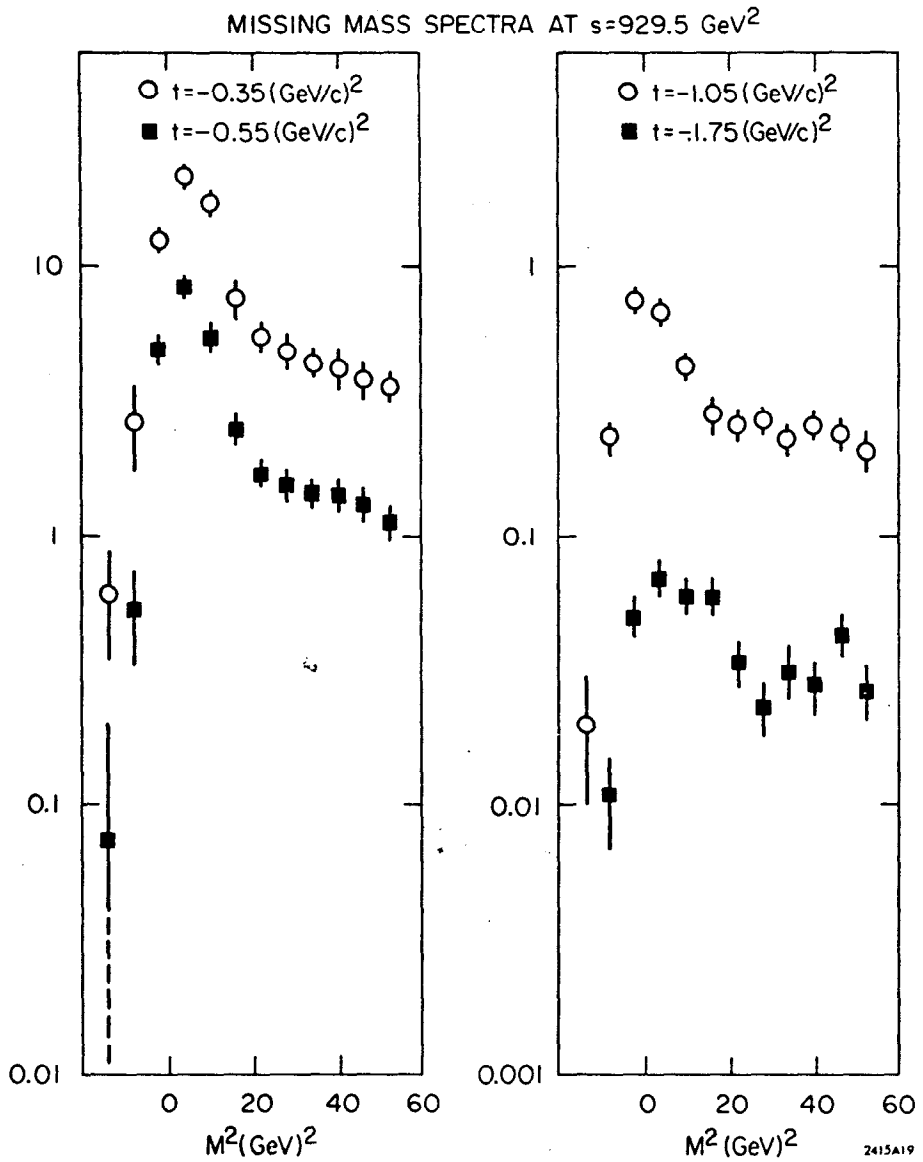

FIG. 19--Missing mass spectra for $pp \rightarrow pX$ as measured by the CHLM group at the ISR, at $s = 930$ GeV^2 and for $t = 0.35$, 0.55, 1.05 and 1.75 GeV^2.

3. Multiparticle production region ($.8 < x < .2$), where the cross-section seems essentially independent of s and where $d\sigma/dt$ is rather flat ($\sim e^{-4t}$) and varying slowly with s and M^2.

The mass dependence in the diffraction peak appears to be compatible with a $1/M^2$ fall off:

1. The 200 GeV/c HBC expt. (Ref. 14)(see Fig. 10).
2. ACGHT group[16] at ISR find $d\sigma/dM^2 \propto (M^{-2})^{1.15 \pm .1}$.
3. CHLM group[17] at ISR find $d\sigma/dM^2 \propto (M^{-2})^{0.98 \pm .1}$.
4. Columbia-Stonybrook[17] at NAL find $d\sigma/dM^2$ compatible with M^{-2}.

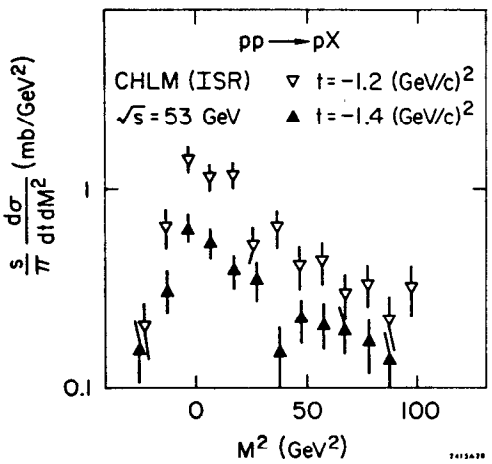

FIG. 20--Missing mass distribution at fixed t, for $\sqrt{s} = 53$ GeV, as measured by the CHLM group at the ISR. Data is presented for t = 1.2 and 1.4 GeV^2.

(This apparent agreement is perhaps a little puzzling in the light of the s- and t-dependence discussed above.)

It is also interesting to note that several high resolution investigations have found evidence for the reaction

$$pp \rightarrow pN^*$$

at high energies, where N* refers to well known nucleon isobars.

Figure 21 shows the missing mass spectrum observed in the NAL US-USSR collaboration experiment.[20] The experimental set-up is the same used to study the elastic p-p scattering,[8] employing solid state detectors to idenfy the recoil proton and a hydrogen gas jet as the target. The missing mass resolution is dominated by the angular resolution of the detectors and is typically ± 100 MeV in the resonance region. The four histograms are the missing mass distributions measured by four different counters placed at different angles (near 90°) to the incident proton beam, and for an incident momentum of 260 GeV/c. Data were taken at 175, 260 and 400 GeV/c. The arrows on each histogram indicate the positions of known isobar which may be diffractively excited — N(1450), N(1560), N(1688), N(1780). A preliminary analysis of the data indicate the cross-section in the resonances region is independent of energy. In particular the cross-section in the 1400 MeV region exhibits a very steep t dependence, e^{-15t}, and that the NAL cross-section is the same as that measured at 20 GeV/c, to within 20%.

Similar observations are reported by a high resolution experiment by the Rutgers-Imperial College group.[21] Their resolution around masses of ~2 GeV is ~10 MeV, and for masses ~7 GeV it is ~50 MeV. Clear signals are observed for the production of N*(1688) and for N*(2190).

The $\pi^- p$[22] and pp HBC[23] experiments at 200 GeV/c both studied the

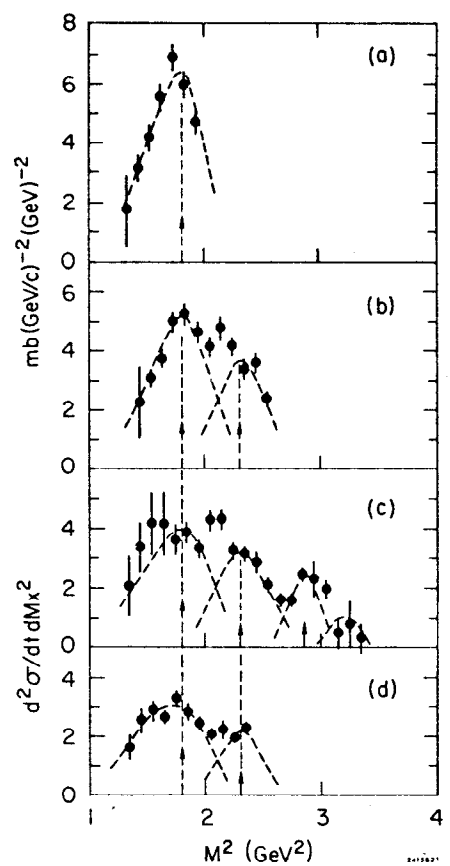

FIG. 21--Missing mass distribution in pp → pN* for an incident proton energy of 260 GeV/c.

exclusive reaction

$$\begin{pmatrix}\pi^- \\ p\end{pmatrix} p \rightarrow \pi^+\pi^- p \begin{pmatrix}\pi^- \\ p\end{pmatrix}$$

The mass distribution for the $p\pi^+\pi^-$ system clearly shows evidence of the production of N(1450) and N(1700) resonances.

In summary then, there is good evidence for the production of low mass isobars in high energy collisions and that their cross-sections seem to roughly scale in M^2 and show steep t dependence.

E. Back to Momentum Transfer Studies

Above we had shown that there was evidence that the slope of the differential cross-section for the diffraction peak became flatter as the diffracted mass increased, and that the $d\sigma/dt$ for the whole peak (averaging over all masses) was exponential but with at least two slopes.

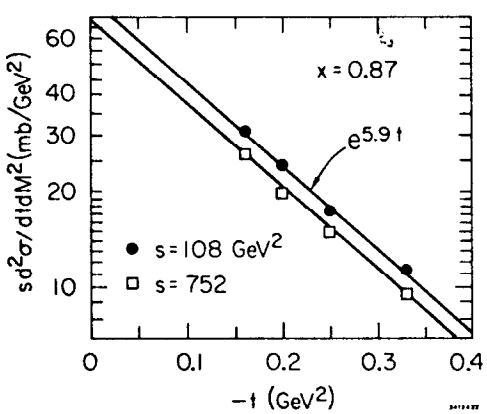

FIG. 22--Differential cross-section for $pp \rightarrow pX$ for x=0.87 and for s = 108 and 752 GeV^2.

In Fig. 22 the s-dependence of the $d\sigma/dt$ is studied. The data comes from the Rutgers-Imperial College group[19] at NAL. For x = 0.87 the differential cross-section, $d\sigma/dt$, is shown for s = 108 and 752 GeV^2. Essentially no energy dependence is observed.

The $d\sigma/dt$ as measured by the Columbia-Stonybrook group[17] at NAL, for missing mass squared around 40 GeV^2 is shown in Fig. 23, together with data from Rutgers-Imperial College[19] and from the CHLM[15] group at ISR. Good agreement is observed between the measurements. A flattening of the cross-section is observed for small t values ($t < .2$ GeV^2). For smaller masses, this effect becomes a turnover in the very forward direction, with a maximum to the cross-section at $t \sim 0.1$ GeV^2, as shown in Fig. 24. Again the data comes from the Columbia-Stonybrook experiment.[17] Corrected data from a previous run by the same group at 200 GeV/c is also shown.[24]

Similar behavior is observed in some preliminary data from the (100 + 400) GeV/c HBC experiments at NAL.[25] In Fig. 25 and 26 the p_T^2 distribution is shown for small masses and large masses respectively. The low mass spectrum shows the same tendency to a forward turnover as the NAL counter experiment, whereas the distribution for large missing masses seems to be quite linear.

F. Multiplicity in Diffractive pp Collisions

As we noted earlier when discussing the structure of the low mass diffractive peak, these events are characterized by a smaller multiplicity, n, than the average. The NAL HBC experiments[11] report that the mean

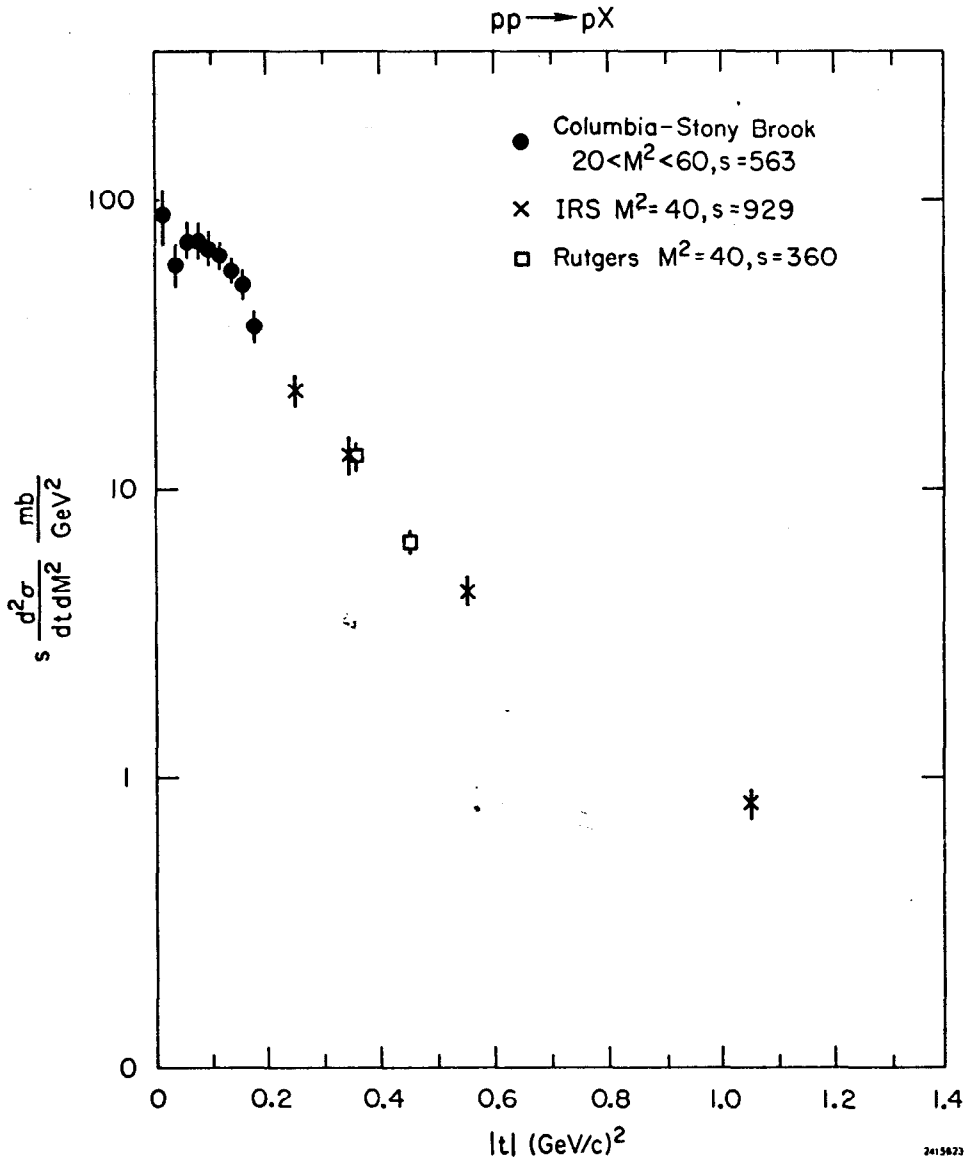

FIG. 23--Differential cross-section for pp→pX for missing mass squared ~40 GeV^2.

diffractive multiplicity, $\langle n_d \rangle$, is about half the total mean multiplicity.

$$\text{i.e.} \quad \langle n_d \rangle \sim \frac{1}{2} \langle n_{all} \rangle$$

At higher energies, the CHLM group[15] at the ISR report

$$\text{for} \quad x > 0.99 \qquad \langle n \rangle \sim 2.8 \pm .5$$

$$x \sim 0.8 \qquad \langle n \rangle \sim 6.7 \pm 1.0$$

is keeping with the NAL observation.

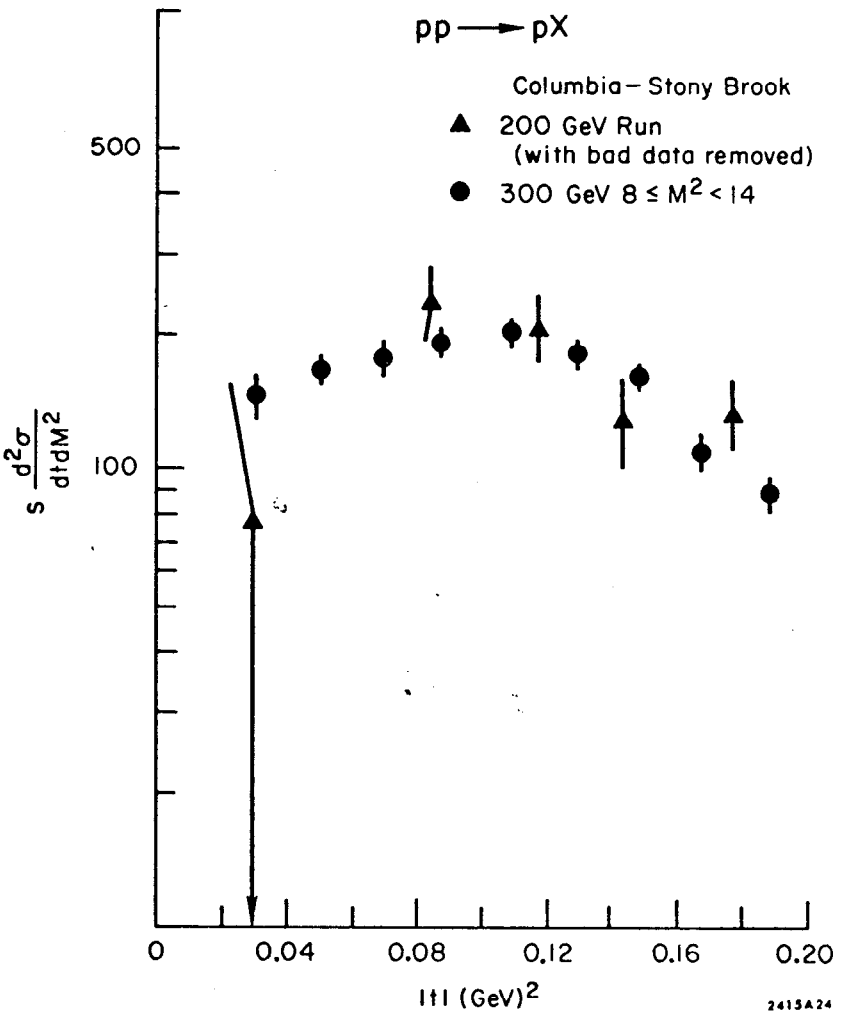

FIG. 24--Differential cross-section for pp → pX for $8 \leq M^2 \leq 14$ GeV^2.

We also noted earlier that the multiplicity increases as the mass in the diffraction peak increases. An interesting comment[14] on this increase is shown in Fig. 27 where the multiplicity in the breakup of the diffractive system is plotted against the mass squared of the system. The solid line is the total multiplicity in pp collisions plotted in such a way that the total energy in the pp collision is called M^2. This implies that the total multiplicity in proton-proton collisions and its energy dependence is similar to that in Pomeron-proton collisions.

PION DIFFRACTION

The first systematic study of high energy pion-proton collisions has been reported to this meeting by the Berkeley-NAL collaboration working on a

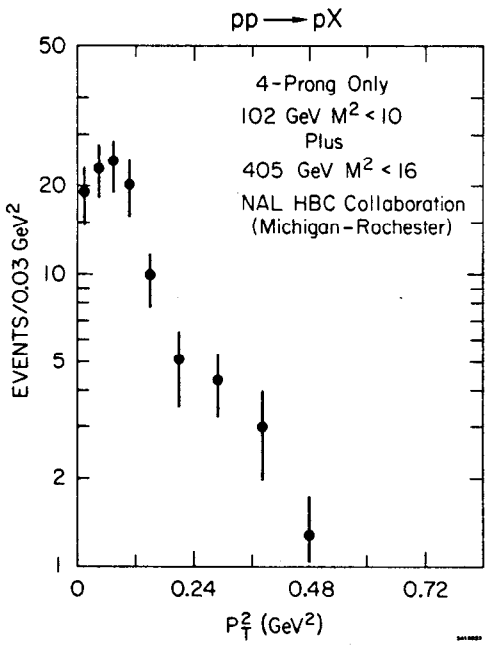

FIG. 25--P_T^2 distributions for small missing masses in pp→pX. Preliminary data from the 100, 400 GeV/c NAL HBC experiments.

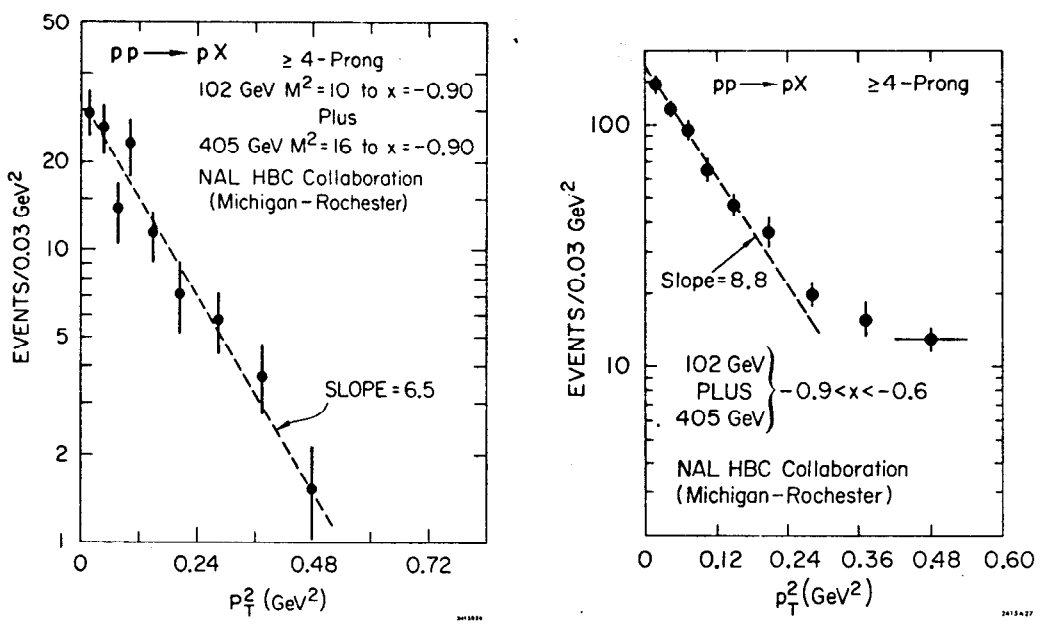

FIG. 26--(a,b) P_T^2 distribution for large missing masses in pp→pX. Preliminary data from the 100, 400 GeV/c NAL HBC experiments.

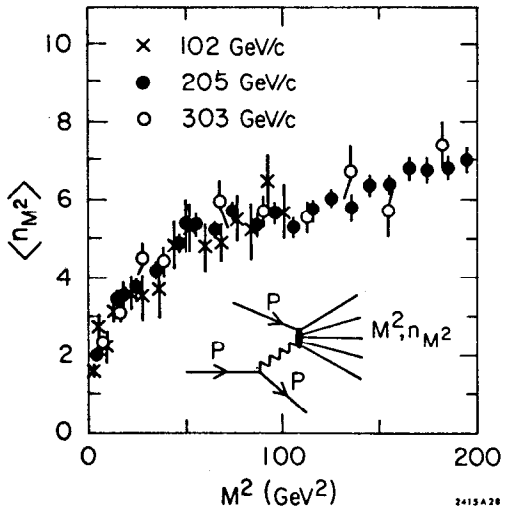

FIG. 27--Multiplicity distribution as a function of the mass of the diffracting system. The solid line is the total multiplicity distribution in pp collisions with the center of mass energy taken equal to M^2.

205 GeV/c $\pi^- p$ exposure of the 30" NAL HBC.[22,26] Their results are briefly outlined below.

They have analyzed the exclusive process

$$\pi^- p \rightarrow \pi^- \pi^+ \pi^- p$$

and claim to have an event sample with less than 25% background. They see strong evidence of the pion diffracting into 3π, and the target proton diffracting into a $(p\pi^+\pi^-)$ system, Fig. 28 and 29. The cross-section for both these processes is estimated to be 1.5 mb.

In addition, the diffraction of a $\pi \rightarrow \pi^*$ has been studied using the same technique as in the p-p HBC experiments. The pictures were scanned for events in which a slow recoil proton could be identified by ionisation. This selection works well for proton momenta up to 1.5 GeV/c.

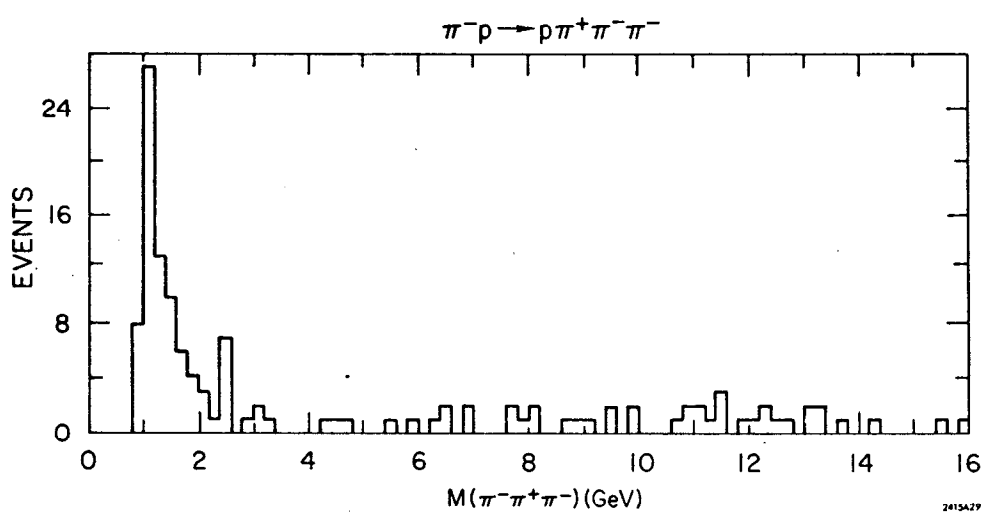

FIG. 28--The effective mass distribution of $(\pi^+\pi^-\pi^-)$ from 200 GeV/c $\pi^- p \rightarrow \pi^+\pi^-\pi^- p$.

The missing mass distribution obtained from these events is shown in Fig. 30. A low mass peak is observed, extending out to $M^2 \sim 20$ GeV^2,

associated with the diffractive excitation of the incoming pion.

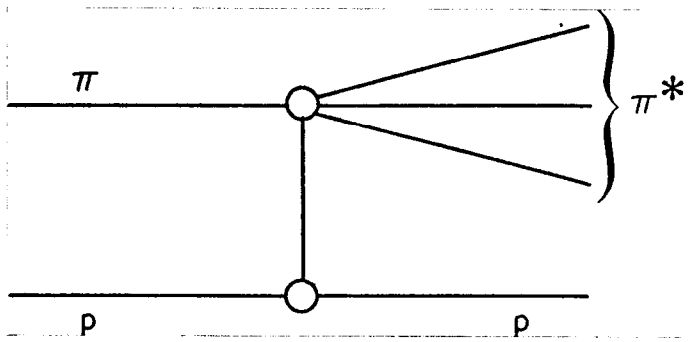

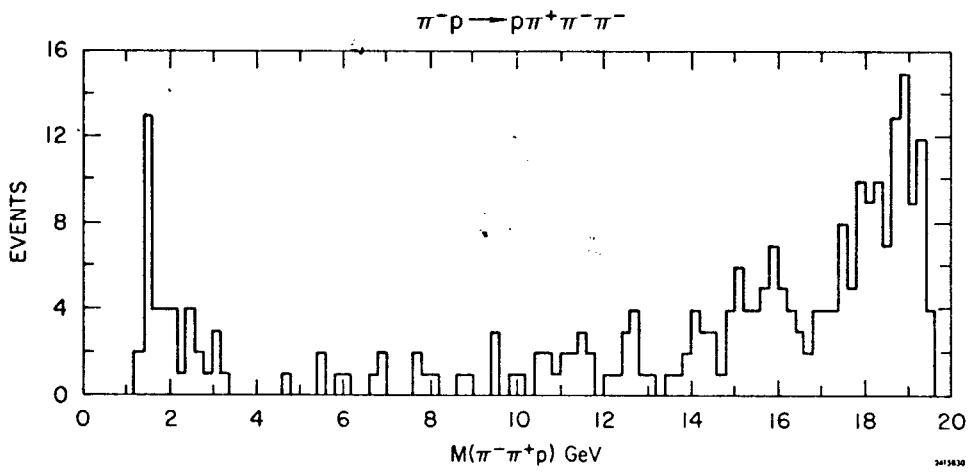

FIG. 29--The effective mass distribution for $(p\pi^+\pi^-)$ from 200 GeV/c $\pi^-p \rightarrow p\pi^+\pi^-\pi^-$.

The mass dependence is shown in Fig. 31, where over a substantial range of masses, the data are consistent with a $1/M^2$ fall-off.

In Fig. 32, the composition of this low mass diffractive peak by topology is presented and as in the p-p studies, one remarks that only the lowest multiplicities contribute to the peak. Again, the central value moves to larger masses as the multiplicity increases. The mean multiplicity in the diffraction peak is about half that of the overall multiplicity ($\langle n_d \rangle^{charged} \sim 4$, $\langle n_{all} \rangle^{charged} \sim 8$) and increases with M^2.

The differential cross-section, $d\sigma/dt$, is shown, by topology in Fig. 33 and for two different mass regions in Fig. 34. No turnover in the forward direction is observed, nor any sizable mass dependence of the slope.

An interesting factorization test has been made possible by the study of the four body exclusive reaction in p-p and π^-p collisions at 205 GeV/c.[27]

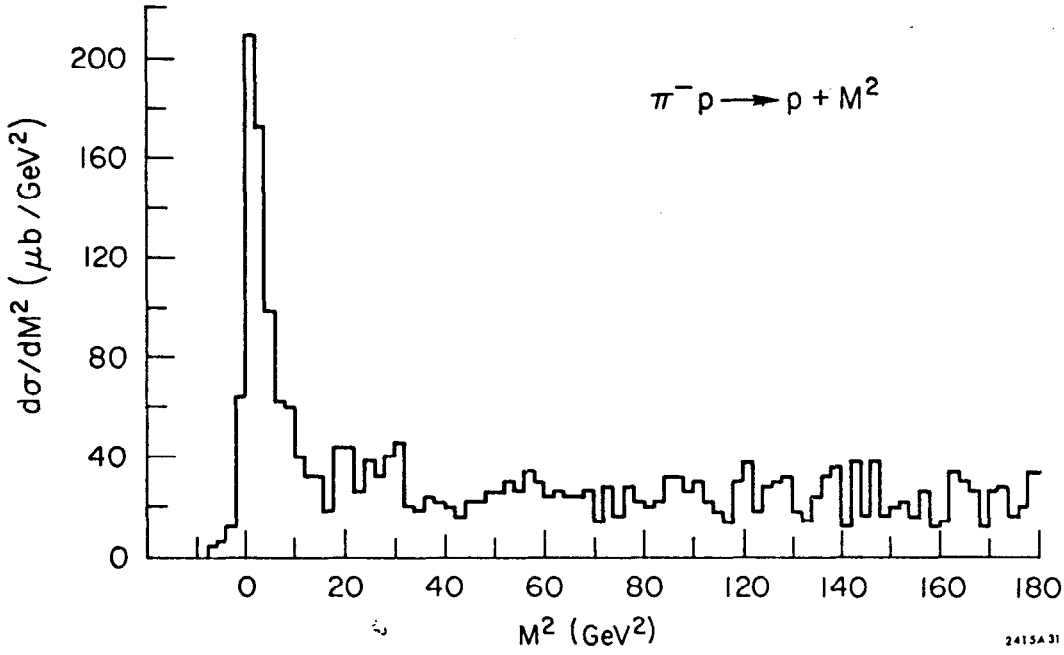

FIG. 30--The missing mass squared distribution for $\pi^- p \rightarrow pX$ at 200 GeV/c.

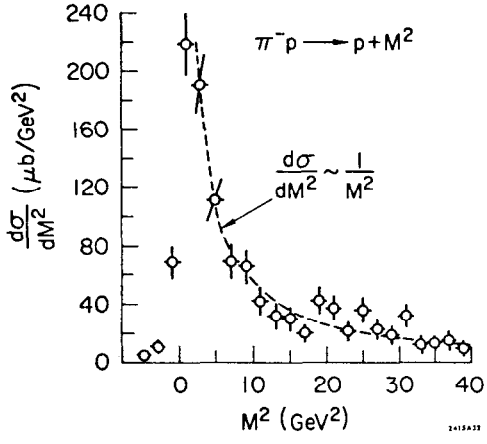

FIG. 31--The missing mass squared distribution for $\pi^- p \rightarrow pX$ at 200 GeV/c.

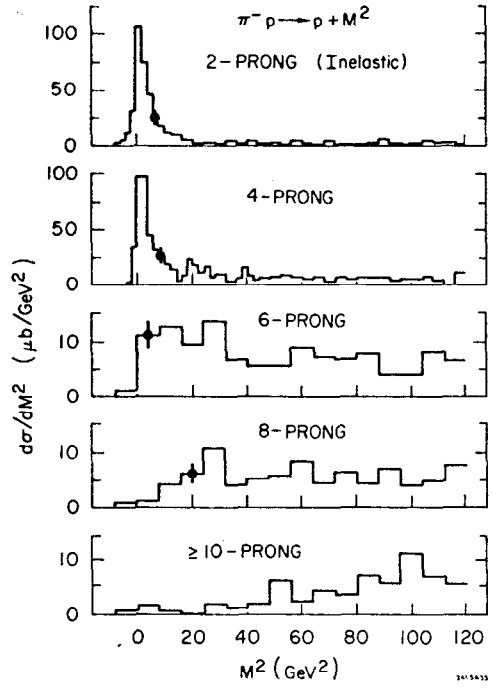

FIG. 32--The missing mass squared distribution, topology by topology, for $\pi^- p \rightarrow pX$ at 200 GeV/c.

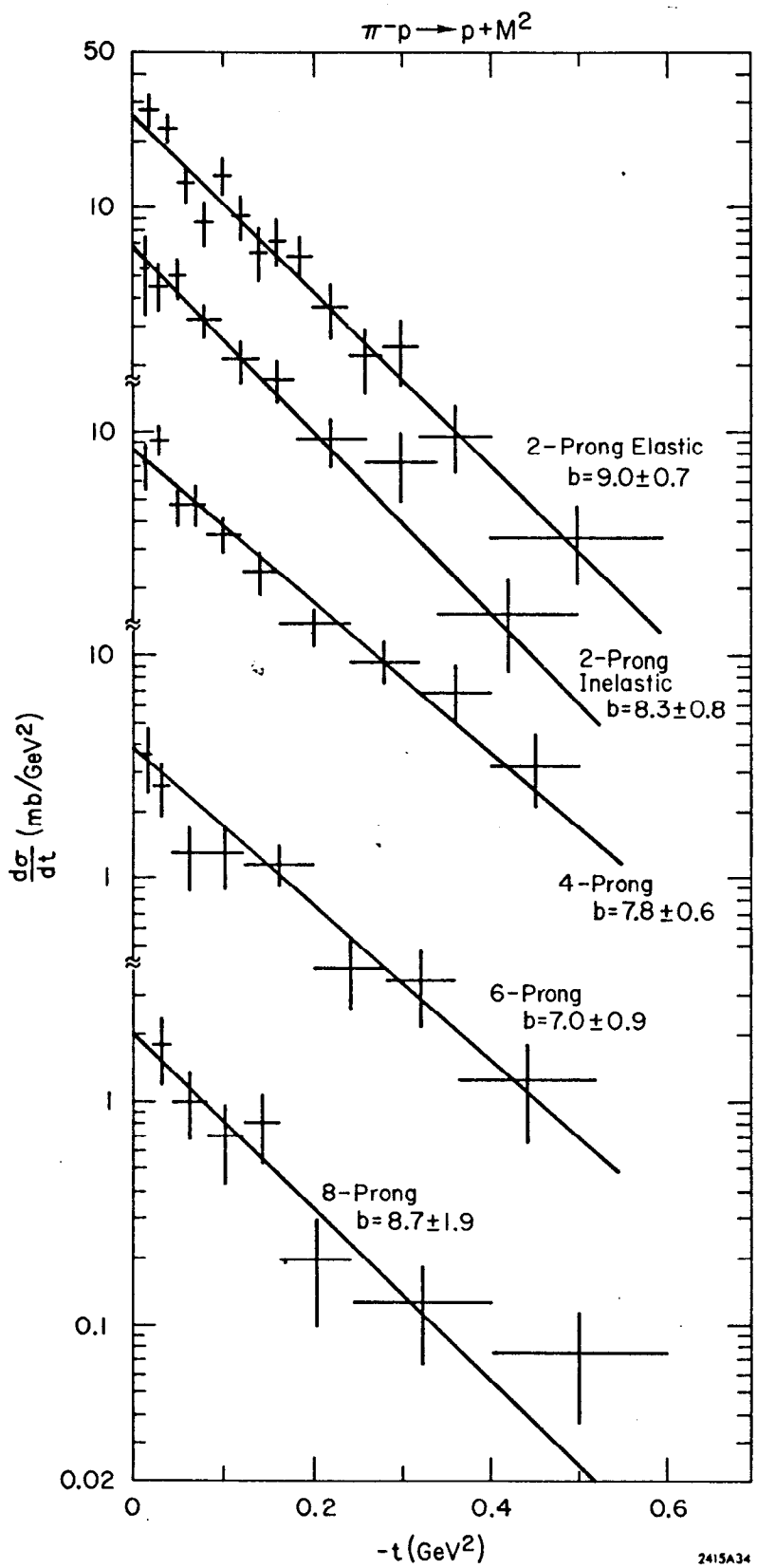

FIG. 33--The momentum transfer distribution, topology by topology, for $\pi^- p \rightarrow pX$ at 200 GeV/c.

The diffraction of the target proton into a $(p\pi^+\pi^-)$ system has been isolated—

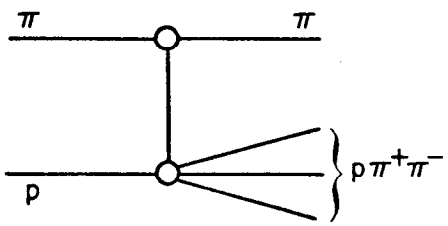

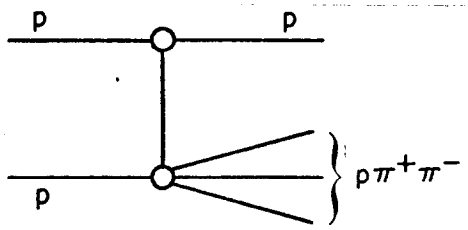

$\sigma_1 = 180 \pm 36\ \mu b$

$\sigma_2 = 370 \pm {}^{40}_{140}\ \mu b$

$\sigma_1 \sim g^2_{\pi\pi\,\mathbb{P}^*}\, g^2_{pp^*\,\mathbb{P}}$

$\sigma_2 \sim g^2_{pp\,\mathbb{P}^*}\, g^2_{pp^*\,\mathbb{P}}$

$$\frac{\sigma_1}{\sigma_2} = \frac{g^2_{\pi\pi\,\mathbb{P}}}{g^2_{pp\,\mathbb{P}}} = \frac{\sigma^{elastic}_{\pi p}}{\sigma^{elastic}_{pp}} = \frac{3.0 \pm 0.3}{6.8 \pm 0.2} = 0.44 \pm 0.05$$

$= 0.5.$

The factorization works remarkably well!

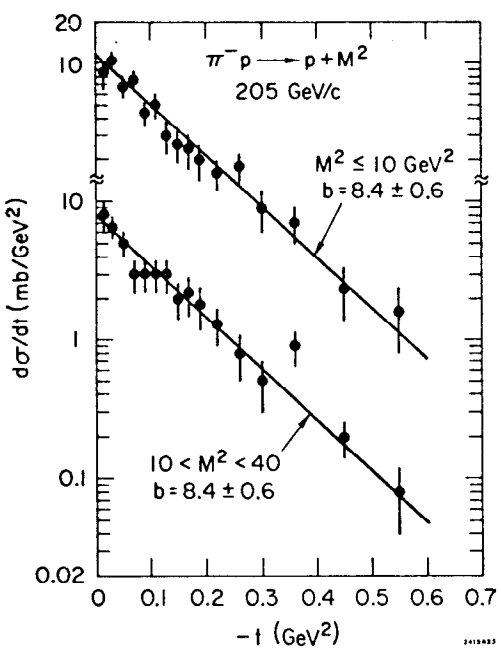

FIG. 34--The momentum transfer distribution for $\pi^- p \to pX$ at 200 GeV/c, for $M^2 < 10$ GeV^2 and $10 < M^2 < 40$ GeV^2.

OTHER COMMENTS

A. Strong Δ^{++} Production Observed at High Energies

The 300 GeV/c NAL HBC collaboration[28] have studied inclusive Δ^{++} production

$$pp \to \Delta^{++} X^0$$

and found a surprisingly large production cross-section. In fact between 6.6 GeV/c and 300 GeV/c the cross-section has only fallen by a factor of two—

$\sigma(pp \to \Delta^{++}X)$ at 6.6 GeV/c is (10 ± 1)mb

and at 300 GeV/c is (4.3 ± 5) mb.

Prompted by the above result the MIT HBC group[29] studied the process

$$\pi^- p \to \Delta^{++} X$$

at 15 GeV/c using the same technique for event selection as the 300 GeV/c pp experiment. In addition they studied the exclusive final states which

gave rise to the Δ^{++} events. Their conclusion, summarized in Fig. 35, is that the Δ^{++} state is produced as a decay product of higher mass N* isobars which are produced diffractively.

This conclusion is supported by the 200 GeV/c pp,[23] and π^-p NAL HBC experiments,[22] in their study of the four body final states

$$pp \rightarrow p\pi^+\pi^-p$$

$$\pi^-p \rightarrow \pi^-\pi^+\pi^-p \ .$$

They observed strong diffractive production of the $(p\pi^+\pi^-)$ system which subsequently decays with $\Delta^{++}\pi^-$.

B. Double Pomeron Exchange

The DESY HBC group[30] have recently searched for evidence of double-Pomeron exchange in 24 GeV/c p-p collisions. They report an upper limit for the cross-section of such a process to be $\leq 30\ \mu b$.

New information is presented to this meeting on two careful studies of the double-Pomeron contribution to $\pi^-p \rightarrow \pi^-\pi^+\pi^-p$,[31] and $pp \rightarrow p\pi^+\pi^-p$[32] final states at 200 GeV/c. A few events are isolated with the correct charge ordering and large rapidity gaps between the dipion system and the projectile and target particles, which could be associated with this production mechanism (see Fig. 36). An upper limit of 50 μb cross-section is reported in both experiments.

C. Triple Regge Phenomenology

Analysis of the single particle distributions at high energies may be done through the application of triple-Regge theory. One wants to calculate the cross-section for processes of the type (a) in Fig. 37. Applying an equivalent of the optical theorem in $2 \rightarrow 2$ body scattering, the total cross-section is then given by the square of the forward scattering amplitude — so for processes of the type (a) we square the forward amplitude by multiplying by itself, shown diagramatically in Fig. 37(b). This is then approximated by the triple-Regge diagram — Fig. 37(c).

The cross-section obtained from this exercise is then written as

$$s\frac{d^2\sigma}{dtdM^2} = \sum_{1,2,3} \frac{R_{123}(t)}{s} \left(\frac{s}{M^2}\right)^{\alpha_1(t) + \alpha_2(t)} M^{2\alpha_3(0)}$$

$$= \sum_{1,2,3} \left(\frac{1}{s}\right)^{1-\alpha_3(0)} R_{123}(t) \left(\frac{s}{M^2}\right)^{\alpha_1(t) + \alpha_2(t) - \alpha_3(0)}$$

It is supposed that such a description should be valid for (s/M^2) and M^2 large.

One then tries to fit the data as a function of s, M^2 and t with an appropriate selection of the trajectories α_1, α_2 and α_3 (see Fig. 37). For Pomeron exchanges, P, $\alpha(0)$ is taken to be 1, and for Regge terms, R,

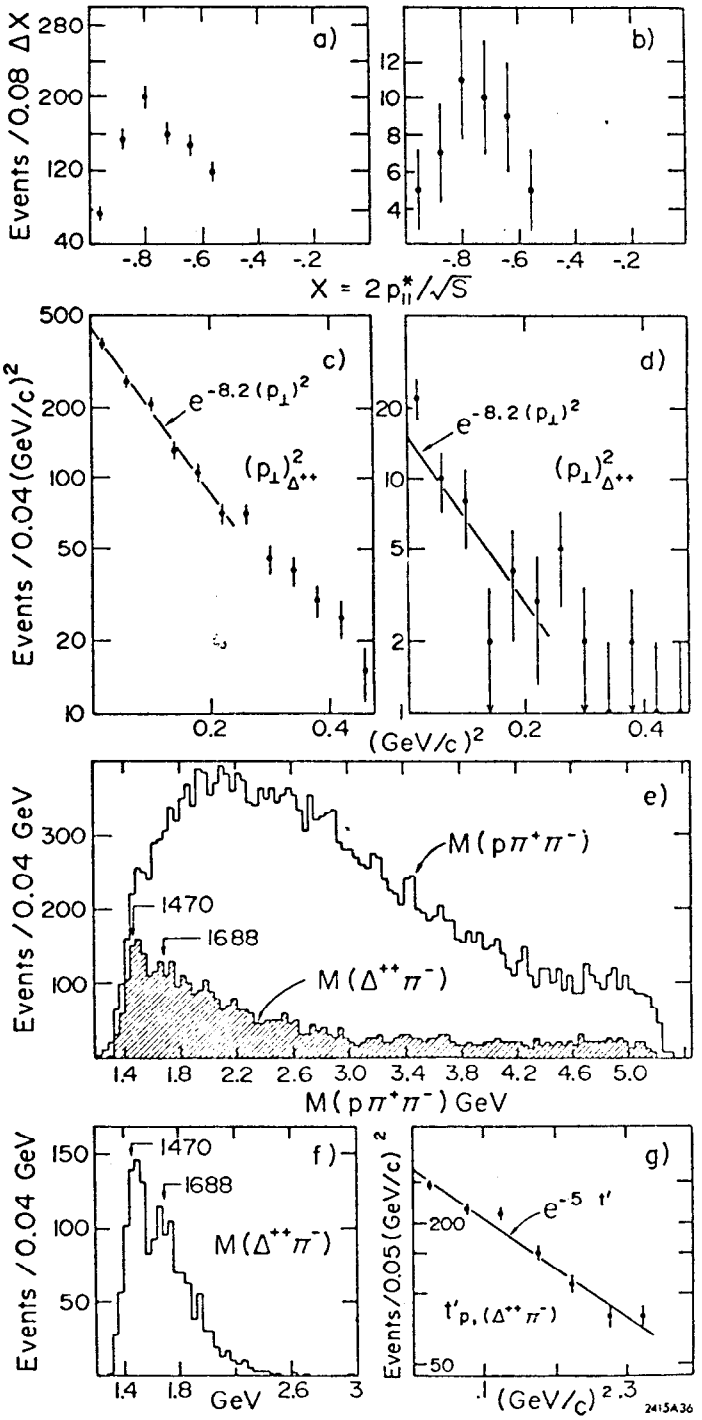

FIG. 35--Figures 2a and 2b compare the x distribution for Δ^{++} produced at 15 GeV/c and 303 GeV/c respectively. Figures 2c and 2d compare the $(P_T)^2_\Delta$ for 15 GeV/c and 303 GeV/c respectively. Figure 2e is the invariant mass of the $p\pi^+\pi^-$ system. The shaded area in the invariant mass of the $\Delta^{++}\pi^-$ system. Figure 2f displays the invariant mass of $\Delta^{++}\pi^-$ where the x of the π^- is between -0.2 and +0.05. Figure 2g is the t' distribution for the events in Fig. 2f.

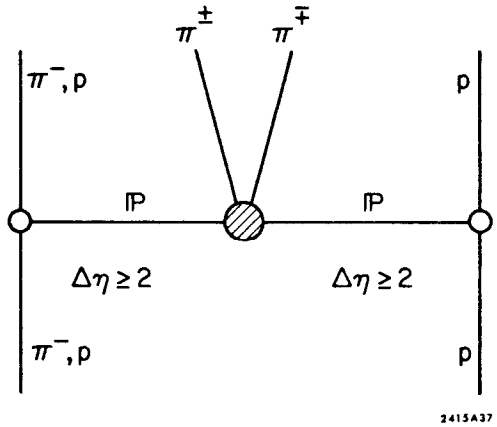

FIG. 36--Diagramatic representation of the Double Pomeron Exchange process for $\pi^-p + \pi^-\pi^+\pi^-p$ and $pp \rightarrow p\pi^+\pi^-p$.

$\alpha(0)$ is taken to be 1/2. Excluding interference terms, there are four leading terms to be used in fitting the data — PPP, PPR, RRP, and RRR. The s-dependence for fixed x and M^2-dependence of each is summarized in the table and in Fig. 38.

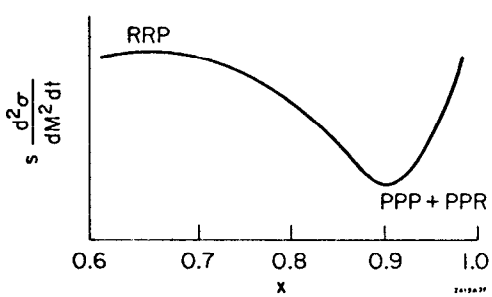

FIG. 38--A qualitative map of the s- and x-dependence of the four triple-Regge terms.

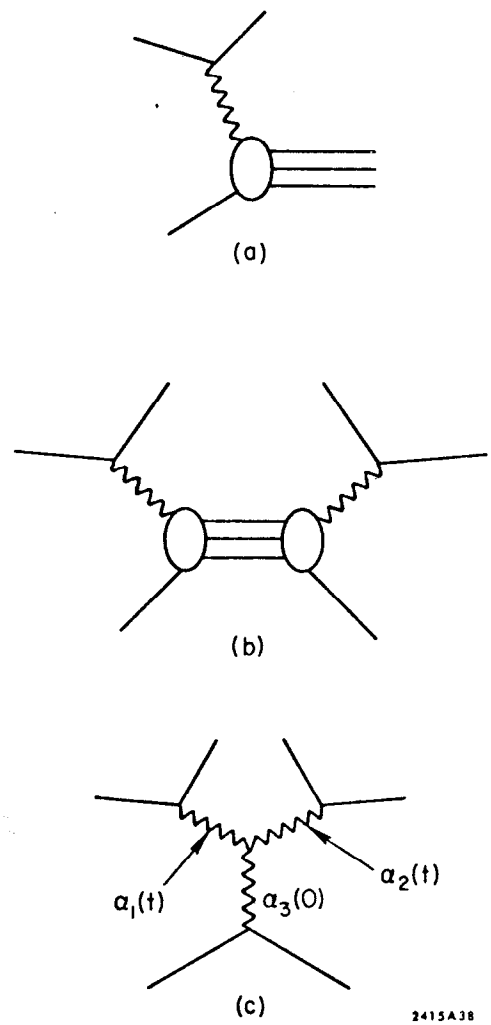

FIG. 37--The triple-Regge calculation of the single particle inclusive cross-section. (a) is the forward scattering amplitude for the single particle inclusive process, and (b) represents diagramatically the square of that amplitude. (c) is the triple-Regge generalization of diagram (b).

If the PPP contribution is not zero,[33] it is expected to dominate at large s and large M^2. Fits to the ISR data[34] show that the data is compatible with substantial PPP coupling, but important contributions from the other trajectories are also required and the fits are by no means unique.

The most systematic attempt to study the triple-Regge question has been performed by the Rutgers-Imperial College group at NAL.[17,35] Their data on the single particle inclusive cross-section spans a large range in the

Triple Regge Term	s-dependence (fixed x)	M^2-dependence, (x-dependence) (fixed s, t)	
PPP	constant	$1/M^2$,	$1/(1-x)$
PPR	$1/\sqrt{s}$	$1/M^3$,	$1/(1-x)^{3/2}$
RRP	constant	constant,	(constant)
RRR	$1/\sqrt{s}$	$1/M$, $M^2=(1-x)s$	$(1/(1-x)^{+1/2})$

important variables:

$$100 \leq s \leq 750 \text{ GeV}^2$$
$$0.14 \leq t \leq 0.38 \text{ GeV}^2$$
$$5 \leq s/M^2 \leq 12.5$$

and has already been discussed (see Fig. 14 and 15) with respect to the scaling behavior of the cross-section. The wide energy range available in this experiment allows a clean separation of the energy dependent terms, PPR and RRR, from the energy independent terms, PPP and RRP.

The data was divided into four t intervals — $0.14 < t < 0.18$, $0.18 < t < 0.22$, $0.22 < t < 0.28$, $0.28 < t < 0.38$ GeV^2, and fit to the triple-Regge cross-section formula given above, with the couplings being left free in each t interval.

Five fits were attempted: (1) in which the four leading triple-Regge terms were used with $\alpha_P = 1 + 0.25t$ and $\alpha_R = 0.5 + t$. This fit was quite poor, not reproducing the dip structure for $x \sim 0.88$. It is interesting to note that the PPP term exhibits a dip in the forward direction with a maximum at $t \sim 0.2$ GeV^2 — see Fig. 39; (2) which uses the same trajectories as in fit (1) but only fits the data for $x > 0.84$. This fit is much better but still not very good. The PPP term still shows the forward turnover; (3) in which the trajectory of the RRP terms is taken to be $\alpha = 0.2 + t$ (after Miettinen and Roberts)[36] to allow for the effects of lower lying trajectories. This provides a much better fit to the data, but now the PPP term has no forward turnover — see Fig. 39; (4) is very similar to fit (3) but an explicit parametrization is used for a $\pi\pi P$ term, (due to Bishari)[37], together with the four leading triple Regge terms with conventional trajectories. This gives a rather good fit to the data, and no forward structure to the PPP term; (5) in which the RRP term is replaced by an exponential e^{-cx}, as suggested by Capella et al.[38] This provides the steeper x-dependence required by the data and indeed this parametrization gives the best fit. Again, the PPP term shows no forward turnover — see Fig. 39.

It is interesting to note that despite the uncertainty and variation in the PPP term between the several fits tried, the energy dependent term — PPR — seems very stable, quite model independent and rather well determined.

In summary, a clear separation between the s-dependent and s-independent terms has been observed. For the s-dependent terms the RRR contribution is small and negligible, while the PPR contribution is well

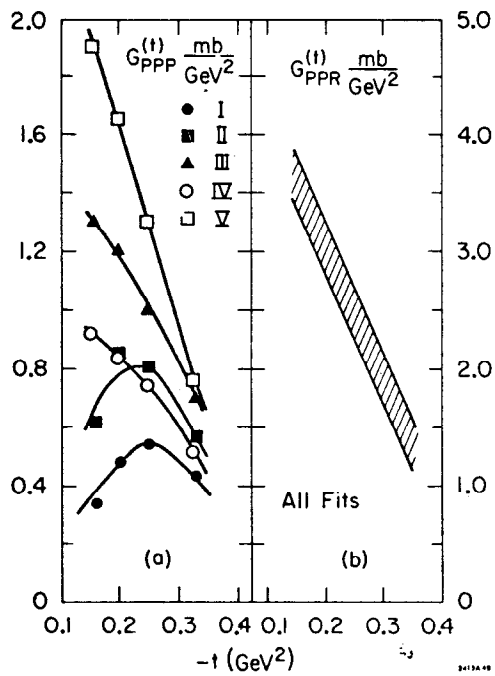

FIG. 39--Plot of G_{PPP} and G_{PPR} versus t for the five fits discussed in the text. For all fits $G_{PPR}(t)$ lies within the shaded band. The shape and magnitude of $G_{PPP}(t)$ depends on the fit assumption.

determined. The energy independent part requires both the PPP and RRP terms, and no unambiguous isolation of the PPP coupling seems possible at this time. Fits with conventional trajectories yielded a PPP coupling which peaked for $t \sim 0.2$ GeV^2 and turned over in the forward direction, while better fits to the data (with modified trajectories) had a quite structureless PPP t-dependence. Therefore not much light can be shed on the question of whether g_{PPP} vanishes at $t = 0$. To make more progress in studying the triple-Regge phenomenology and in particular to identify unambiguously the PPP contribution new data extending further into the diffraction peak, to x values nearer 1, are urgently required.

CONCLUSIONS

It has been interesting to see the new results from NAL providing detailed systematic data on high energy collisions and nicely complimenting the ISR data to give new and exciting insights on the structure of the proton.

The results on the s- and t-dependence of the elastic pp scattering and the s-dependence of the total cross section provide an interesting picture of the proton structure. It will be very interesting to see the total cross-section, elastic cross-section and real part measurements for K^+p scattering at NAL, where the features we have observed in pp scattering should also emerge.

The single particle inclusive studies have shown the existence of a large energy independent cross-section for the production of a low-mass peak. This process is assumed to be diffractive excitation of the target or projectile particle and has a cross-section almost equal to the elastic scattering cross-section, viz $\sigma_d \sim 6$ mb. At high energies the "low" mass peak in fact includes quite large masses (e.g., it extends up to masses of 5-7 GeV). This diffractive peak is made up mainly from the low multiplicity events, the mean multiplicity for events in the peak being about half the mean multiplicity for all events. The multiplicity increases with the mass of the diffracted system. Very similar properties are observed for the diffraction of pions or protons. The s-dependence and the x-dependence of the data is quite consistent with a strong PPP coupling, but no unambiguous determinations of the PPP properties has been achieved.

ACKNOWLEDGMENTS

I would like to thank Prof. F. Gilman and Dr. R. Cashmore for reading the manuscript and for their helpful comments.

REFERENCES

1. D.W.G.S. Leith, "Diffraction Dissociation" SLAC report no. SLAC-PUB-1141, Review talk presented at XVI International Conference on High Energy Physics, Batavia, Illinois; D.W.G.S. Leith "Diffraction Phenomena" SLAC report no. SLAC-PUB-1263; G. Kane "Phenomenology of Diffractive Reactions" Rutherford Preprint RPP/T/20; H. Lubatti, "Diffraction Dissociation of Hadrons", Washington University Preprint VTL PUB 9.
2. U. Amaldi, et al., Phys. Letters 44 B, 112 (1973).
3. S. R. Amendolia, et al., Phys. Letters 44 B, 119 (1973).
4. U. Amaldi and G. Bellettini, (private communication).
5. U. Amaldi, private communication on a comment by D.R.O. Morrison.
6. G. Barbiellini, et al., Phys. Letters B 39, 663 (1972) and Phys. Letters B 35, 355 (1971).
7. U. Amaldi, et al., paper submitted to the APS Division of Particles and Fields Meeting, Berkeley, August 1973.
8. V. Bartenev, et al., NAL Pub 73/54. Paper submitted to the APS Division of Particles and Fields Meeting, Berkeley, August 1973.
9. G. Giacomelli, Rapporteur's talk at XVI International Conference on High Energy Physics, Chicago-Batavia, 1972.
10. M. G. Albrow, et al., CERN preprint and submitted to the XVI International Conference on High Energy Physics, Chicago-Batavia, 1972.
11. There are four HBC pp experiments at NAL: (a) 102 GeV/c — Michigan-Rochester collaboration; (b) 205 GeV/c — ANL-NAL collaboration; (c) 303 GeV/c — NAL-UCLA collaboration; (d) 405 GeV/c — Michigan-Rochester collaboration.
12. From a compilation by J. Whitmore (private communication).
13. J. Vander Velde, (private communication).
14. S. J. Barish, et al., ANL/HEP 7338 and paper presented to the APS Division of Particles and Fields Meeting, Berkeley, August, 1972.
15. M. G. Albrow, et al., CERN preprint, Dec., 1972.
16. Aachen-CERN-Harvard-Genoa-Torino report, communicated by G. Goldhaber.
17. R. Schamberger, et al., Paper submitted to the APS Division of Particles and Fields Meeting, Berkeley, August 1973.
18. S. Childress, et al ., Paper submitted to the APS Division of Particles and Fields Meeting, Berkeley, August 1973.
19. K. Abe, et al., "Measurement of $pp \rightarrow pX$ between 50 and 400 GeV/c", paper submitted to the APS Division of Particles and Fields Meeting, Berkeley, August, 1973.
20. B. Bartenev et al., "Diffraction Excitation of Nucleon Resonances in p-p Collisions at Incident Proton Energies from 175 to 400 GeV/c," paper submitted to the APS Division of Particles and Fields Meeting, Berkeley, August, 1973.

21. K. Abe, et al., "Measurement of N* Production in pp→pN* between 9 and 300 GeV/c", paper submitted to the APS Division of Particle Fields Meeting, Berkeley, August, 1973.
22. G. S. Abrams, et al., LBL-2112 and paper submitted to the APS Division of Particles and Fields Meeting, Berkeley, August, 1973.
23. M. Derrick, et al., ANL/HEP-7332 and paper submitted to the APS Division of Particles and Fields Meeting, Berkeley, August, 1973.
24. This data was originally presented in preliminary form at the Vanderbilt Conference on Inclusive Processes at High Energy, 1973. Corrections for instrumented failure have changed the cross-sections in the forward direction.
25. J. Vander Velde, (private communication).
26. F. C. Winkelmann, et al., LBL-2113 and paper submitted to the APS Division of Particles and Fields Meeting, Berkeley, August, 1973.
27. F. C. Winkelmann, (private communication).
28. F. T. Dao, et al., Phys. Rev. Letters 30, 34 (1973).
29. D. Brick, et al., submitted to Phys. Rev. Letters and to the APS Division of Particles and Fields Meeting, Berkeley, August, 1973.
30. V. Idschok, et al., Nucl. Phys. B 53, 282 (1973).
31. D. M. Chew, et al., talk presented at the APS Division of Particles and Fields Meeting, Berkeley, August, 1973.
32. M. Derrick, et al., ANL/HEP-7339 and paper submitted to the APS Division of Particles and Fields Meeting, Berkeley, August, 1973.
33. Abarbanel, et al., Phys. Rev. Letters, 26, 937 (1971); Ellis, et al., Phys. Rev. D 6, 1347 (1972).
34. CERN-Holland-Lancaster-Manchester Group, M. G. Albrow, et al., CERN preprint; A. Capella, et al., SLAC report no. SLAC-PUB-1252. References to earlier work may be found in this paper.
35. K. Abe, et al., "Determination of Triple-Regge Coupling from a Study of Reaction pp→pX between 50 and 400 GeV/c", paper submitted to the II Aix-en-Provence International Conference on Elementary Particles, September, 1973.
36. H. I. Miettinen and R. G. Roberts, Rutherford Lab Preprint RPP/T/40 (1973).
37. M. Bishari, Phys. Letters 38 B, 510 (1972).
38. A. Capella, et al., Orsay Preprint 72/73.

Supplement to
SLAC-PUB-1330
(T/E)
November 1973

DIFFRACTIVE PROCESSES IN THE (5-40) GEV ENERGY RANGE*†

David W.G.S. Leith

Stanford Linear Accelerator Center
Stanford University, Stanford, Calif. 94305

ABSTRACT

Recent data on diffractive processes in the energy range (5-40) GeV/c are summarized. This material was not covered in the Berkeley talk, and is included here for completeness.

* Work supported by the U.S. Atomic Energy Commission.

† Supplement to an Invited paper presented at the 1973 Meeting of the Division of Particles and Fields of the APS, Berkeley, California, August 13-17, 1973.

INTRODUCTION

The data on high energy diffractive processes from the NAL and ISR accelerators (i.e., $p > 50$ GeV/c) was reviewed in an invited talk at the Berkeley APS meeting,[1] but for reasons of time pressure and continuity of material, lower energy data was not included. For completeness, the recent experimental results in the (5-30) GeV/c region are reviewed in this Appendix.

ELASTIC SCATTERING

Several interesting experiments have been reported measuring elastic scattering differential cross-sections.

At Argonne, the Effective Mass Spectrometer group[2] have performed a high statistics study of $\pi^{\pm}$, $K^{\pm}$, $p^{\pm}$ scattering at four energies (3, 3.65, 5 and 6 GeV/c) for $0.02 \leq t \leq 2$ GeV^2. The measured cross-sections are shown in Fig. 1-4. For $t < 0.5$ GeV^2 they find that the $\pi^{\pm}$, $K^{\pm}$ cross-sections have a linear behavior (i.e., $\frac{d\sigma}{dt}$ is well represented by $A e^{bt}$), while the $p^{\pm}$ data exhibit some curvature (i.e., $\frac{d\sigma}{dt} \propto A e^{bt+ct^2}$). The measured values of the slope are shown in Table 1, and together with other available data in Fig. 5. The K^+ and p slopes clearly exhibit shrinkage, while the $\pi^{\pm}$ and p^- are essentially constant and the K^- shows marginal evidence of anti-shrinkage. The momentum dependence of the forward slopes is summarized in Table 2.

The cross-over in the particle, anti-particle cross-sections have been studied for each incident particle and no energy dependence in the position of the cross-over found (see Fig. 6). The cross-over point does, however, depend on the incident particle —

$$\pi: \quad t_c = 0.14 \pm 0.03 \text{ GeV}^2$$

$$K: \quad t_c = 0.19 \pm 0.006 \text{ GeV}^2$$

$$p: \quad t_c = 0.16 \pm 0.004 \text{ GeV}^2$$

The total elastic cross-section for all six reactions are listed in Table 3, for the four energies measured.

At SLAC, a high statistics wire chamber experiment[3] has just been completed, studying $K^{\pm}p$ scattering at 6, 10 and 14 GeV/c and $\pi^{\pm}p$ and $p^{\pm}p$ scattering at 10 GeV/c. Preliminary data on $K^{\pm}p$, $p^{\pm}p$ at 10 GeV/c and $K^{\pm}p$ at 14 GeV/c were presented for the small t region (i.e., $t < .3$ GeV^2).

Figures 7 and 8 show typical measured cross-sections, while the slopes are summarized in Fig. 9, together with those of the two other experiments reported here.

The hyperon beam group at Yale (Hungerbuehler et al.)[4] have studied the slope of the π^-p and Σ^-p elastic scattering at 23.3 GeV/c. Figure 10 shows the two differential cross-sections. The data are well represented by

$$\frac{d\sigma}{dt} = A e^{bt}$$

with

$$b_{\pi} = 7.99 \pm .22 \text{ GeV}^{-2}$$

$$b_{\Sigma} = 8.97 \pm .26 \text{ GeV}^{-2}$$

The slope parameter for the Σp scattering is, not surprisingly, very similar to the slope in p-p scattering at the same energy.

Finally, there is data from the CERN-Serpukov collaboration[5] on particle scattering at 25 and 40 GeV/c. The differential cross-sections are shown in Fig. 11 and the fits to the data to the form $\frac{d\sigma}{dt} = A e^{bt+ct^2}$, are summarized in Table 4.

The shrinkage of the forward elastic peak has been studied by fitting all available data for $10 < s < 76$ GeV^2, at $t = 0.2$ GeV^2 with the slope parameterized

as $b = b_0 + 2\alpha' \ln s$. They find

$$\left.\begin{array}{l} \alpha'(\pi^-) = 0.18 \pm 0.04 \\ \alpha'(K^-) = 0.19 \pm 0.04 \end{array}\right\} \text{small shrinkage}$$

$$\alpha'(p^-) = -0.5 \pm 0.05 \qquad \text{anti-shrinkage}$$

They also observe a rather strong t-dependence to the shrinkage, as shown in Table 5.

The angular distributions have been integrated to give the total elastic cross-section (see Table 4). When compared to the available data in the range $5 < p < 40$ GeV/c they find

$$\sigma^{\pi^-} \propto p^{-0.25 \pm 0.02}$$

$$\sigma^{K^-} \propto p^{-0.26 \pm 0.03}$$

$$\sigma^{\bar{p}} \propto p^{-0.42 \pm 0.03}$$

Some data on π-π and K-π diffraction scattering has recently become available. Walker et al.[6] have studied

$$\pi^- p \rightarrow \pi^+ \pi^- n \qquad \text{at 25 GeV/c}$$

$$\pi^- p \rightarrow \pi^- \pi^- \Delta \qquad \text{for (5-25) GeV/c}$$

The production angular distributions are shown in Fig. 12.

They find that the forward peak is well fit to

$$\frac{d\sigma}{dt} \propto e^{bt} \qquad \text{with}$$

$$b(\pi^+ \pi^-) = 5.9 \pm 0.54 \text{ GeV}^{-2}$$

$$b(\pi^- \pi^-) = 6.1 \pm 0.51 \text{ GeV}^{-2}$$

The integrated data yields $\sigma^{el}(\pi^+\pi^-) \sim \sigma^{el}(\pi^-\pi^-) \sim 1.5$ mb and the total cross-sections are $\sigma_T^{\pi^+\pi^-} \sim \sigma_T^{\pi^-\pi^-} \sim 15$ mb. (See Fig. 13.) Their total cross-section agrees with previous estimates[7] and taken together, all the data implies that

$$\sigma_0 = \sigma_1 = \sigma_2 = (15\text{-}20) \text{ mb}$$

i.e., the 3 isospin cross-sections in π-π scattering are all equal, as expected for a diffractive process.

Also, there is some data from the LBL π^+p 8 GeV/c, and K^+p 12 GeV/c experiments.[8] Diffractive π-π, K-π scattering is isolated by choosing small t for the incident meson scattering, selecting $M(p\pi^+) > 1400$ MeV to remove the strong pion exchange reaction and selecting $M(\pi\text{-}\pi)$ or $M(K\text{-}\pi) > 1600$ MeV to isolate the diffractive π-π, K-π scattering from the s-channel resonance formation processes.

For $t < 0.3$ GeV^2 they find

$$b^{\pi\pi} = 4.14 \pm .22 \text{ GeV}^{-2}$$

$$b^{K\pi} = 4.10 \pm .25 \text{ GeV}^{-2}$$

In summary, the elastic scattering data confirms that the scattering distribution is sharply peaked, and well parameterized as $\frac{d\sigma}{dt} \propto A e^{bt}$ for small t. The slope parameter, (b), is steeper in $\overline{X}p$ scattering than for Xp scattering. This fact together with the equality of the integrated cross-sections (i.e., $\sigma_{el}(Xp) \approx \sigma_{el}(\overline{X}p)$) implies a cross-over in the differential cross-sections. This cross-over phenomena has been investigated in detail in the (3-6) GeV/c region and although a substantial dependence is observed on the nature of the scattering particles, no s-dependence (over this range) is detected. The slopes of the scattering distribution are observed to change with energy — the K^+p and pp

system exhibiting strong shrinkage, the $\pi^{\pm}p$, $K^{-}p$ slopes being essentially flat, and the $\bar{p}p$ scattering showing an anti-shrinkage behavior. This shrinkage phenomenon, observed for the $K^{+}p$ and pp scattering, is normally understood as being due to the slope of the Pomeron trajectory; the effect is masked by strong Regge effects in the other elastic scattering reactions.

THE φ STORY

The data on the photoproduction of the φ meson has been a puzzle for some time. Since the φ-meson decouples from other mesons, we do not expect any strong t-channel amplitudes other than the pomeron. Thus the study of φ photoproduction should be an ideal laboratory to learn of the pomeron's properties — much better, in principle, than the study of $K^{+}p$ or pp where the pomeron dominance depends on cancellations of Regge amplitudes through exchange degeneracy.

The φ is observed to be strongly produced coherently from complex nuclear targets,[9] and the t-channel amplitude in $\gamma p \rightarrow \varphi p$ is essentially purely natural parity.[10] These observations support the pomeron exchange dominance hypothesis.

The data on the differential cross-section is rather sparse and quite inconclusive as to whether there is any shrinkage of the forward slope, never mind any quantitative measure of how much it shrinks!

A recent SLAC experiment of Ritson's Group[11] measured the s-dependence of the φ cross-section for $t = 0.6\ \mathrm{GeV}^2$ and found no shrinkage whatsoever.

New data from a Bonn group[12] at 2 GeV is shown in Fig. 14. The slope of the differential cross-section at $t = .6\ \mathrm{GeV}^2$ is shown in Fig. 15 together with the Ritson data. Clearly the data support the "no-shrinkage" conclusion and more quantitatively find $b = b_0 + 2\alpha' \ln s$ with $\alpha' = 0.14 \pm 0.09\ \mathrm{GeV}^{-2}$.

Why is the φ cross-section so flat, when K^+p and pp data shrink quite considerably in this energy range? (See Fig. 16.)

It is interesting to note that at high energies (i.e., ISR energies) the pp scattering distributions for the same t values show no energy dependence, remarkably like the φ photoproduction data. Fits to the ISR p-p scattering data in this t range yield $\alpha' = 0.10 \pm 0.06$.[13] This prompts the question of whether the s-dependence observed in p-p scattering in the (5-20) GeV/c region (see Fig. 16) is due to Regge effects and that the bare pomeron properties are seen in the very high energy scattering. Then $\gamma \rightarrow \varphi$ data may indeed be showing pomeron like behavior at low energies as expected.

An interesting explanation of the lack of shrinkage is offered in the two component model of the pomeron described by Kane.[14] He introduces a central contribution (the conventional pomeron) and an additional peripheral piece which accounts for the small t shrinkage observed in high energy p-p scattering. These two contributions would then lead to the picture shown in Fig. 17. The central contribution has a slow, (or zero), energy dependence while the peripheral contribution shrinks quite rapidly (like $\ln s$) with its first zero around $t \sim 0.2$ GeV^2. As s increases there is a region in t around 0.5 GeV^2 (at least beyond $t \sim 0.2$ GeV^2) where the peripheral contributions cross for different s, and which therefore displays no s-dependence. This model explains the small t shrinkage in p-p scattering, and the lack of shrinkage in the large t p-p and $\gamma \rightarrow \varphi$ data.

It would be nice to have some good data at small t, to see if the $\gamma \rightarrow \varphi$ cross-section does indeed shrink for small t, as would be predicted by the above model, or the ISR pp data.

Also, if indeed the real pomeron behavior is as described by the Kane model, or by the ISR pp scattering data, what is causing the shrinkage observed

for K^+p and pp scattering in the (5-30) GeV/c range and why the success of the Dual Absorptive Model fits explaining the shrinkage in $\pi^{\pm}p$ elastic scattering[15] and in rho photoproduction?[16]

DIFFRACTION DISSOCIATION PROCESSES

By Diffraction Dissociation we mean the nonelastic processes in which either the incident particle or the target particle is excited into a low mass system. These excitations seem to be strongest near to quasi-two body thresholds and it is far from clear whether they are due to resonant behavior or to some kinematic enhancement like the Deck Effect.[17] There is a growing amount of evidence indicating that at least the dominant effect is due to kinematics.

Preliminary results on diffraction dissociation of the nucleon from a 15 GeV/c $\pi^- n \rightarrow \pi^- p \pi^-$ bubble chamber experiment[18] were reported at this meeting. The mass distribution for the $(p\pi^-)$ system is shown in Fig. 18, for two t regions; (a) for $t < 0.08$ GeV^2, and (b) for $0.08 < t < 1.0$ GeV^2. There is a clear difference between the two spectra — the small t data peaking at masses around 1250 MeV and otherwise quite structureless, while the larger t data shows signs of the well-known nucleon isobars which are produced in diffractive process — (N*(1470), N*(1750)). The production angular distributions reflect that two different mechanisms are responsible for the $n \rightarrow (p\pi^-)$ reactions. In Fig. 19 the t-distributions are shown for (a) $M(p\pi^-) < 1400$ MeV, and (b) for $1400 < M(p\pi^-) < 2000$ MeV. The data with $M(p\pi^-) < 1400$ MeV are produced very peripherally with $\frac{d\sigma}{dt} \propto e^{-15t}$, while the resonance region has a much flatter production distribution, $\frac{d\sigma}{dt} \propto e^{-5.7t}$.

The decay angular distributions of these same two mass regions, are also quite different. The low mass data exhibit essentially isotropic θ and φ distributions while the higher mass region shows evidence of higher partial waves.

These data indicate that the production mechanism for the peripheral low mass enhancement and that for the production of the accepted "diffraction-produced" resonances is not the same.

New data on pion dissociation was presented by the 15 GeV/c $\pi^- d$ bubble chamber collaboration of Seattle-Berkeley[19] and from the 25, 40 GeV/c CERN-Serpukov collaboration.[20]

The Seattle-Berkeley[19] three-pion mass distribution from the reaction $\pi^- d \rightarrow \pi^+ \pi^- \pi^- d$ is shown in Fig. 20. The usual dominating A_1 enhancement is seen at masses around 1100 MeV, together with the A_3 enhancement at 1660 MeV. They also observe a three standard deviation effect at 1960 MeV which they call the A_4. The claim is that the A_1 region is mainly a $(\rho\pi)$ enhancement, the A_3 region is mainly an $(f\pi)$ enhancement, and that the A_4 region is associated with a $(g\pi)$ system. The (2π) mass distribution is shown in Fig. 21 where indeed a small f-, and an even smaller g-meson signal is seen. These f-, and g-meson signals are strongly magnified if mass selection is made on the A_3, and A_4 (3π) mass regions, respectively.

The data from Serpukov[20] for $\pi^- p \rightarrow \pi^+ \pi^- \pi^- p$ at 40 GeV/c is shown in Fig. 22. No sign of the A_4 peak discussed above is seen, nor is there any sign of a g-meson signal in the associated (2π) mass plots. It is not clear whether these differences are questions of apparatus acceptance, or a real physics issue — time will tell!

The s- and t-dependence of the cross-section for this reaction is studied as a function of the (3π) mass. The results are summarized in Table 6. The slope of the production angular distribution gets flatter as the (3π) mass increases, being of order 15 GeV^{-2} for masses near threshold and falling to ~ 5 GeV^{-2} for $M(3\pi) \sim 2000$ MeV. The s-dependence was studied over the interval (11-40) GeV/c

and shows that the cross section falls slowly for all 3π masses — being very similar to the elastic cross-section energy dependence for small 3π masses (i.e., $\sigma \propto p^{-0.31 \pm 0.11}$), and falling just slightly faster for masses in the neighborhood of 2000 MeV, ($\sigma \propto p^{-0.5 \pm 0.1}$).

The energy dependence for the three enhancement regions — the A_1, A_2 and A_3 regions — is given in Figs. 23-25 and is found to be

$$\sigma \propto p^{-n} \quad \text{with}$$

$$n(A_1) = 0.40 \pm 0.06$$

$$n(A_2)^{\text{natural}} = 0.51 \pm 0.05$$

$$n(A_2)^{\text{unnatural}} = 2.1 \pm 0.2$$

$$n(A_3) = 0.57 \pm 0.2$$

It is interesting that the A_2 cross-section (supposedly mainly vector and tensor exchange) has such a similar energy dependence to the A_1 and A_3 regions, (which are thought to be produced by pomeron exchange).

The A_1 region decay distributions were analyzed and the 1100 MeV enhancement confirmed as being associated with $J^P = 1^+$ s-wave $\rho\pi$ decays. The phase of this wave shows almost no energy dependence with any of the background waves — (i.e., it does <u>not</u> look like a Breit-Wigner resonance amplitude). See Fig. 26.

The A_2 region is identified as $J^P = 2^+$, with a d-wave $\rho\pi$ decay mode — see Fig. 27. The phase of this 2^+ wave with respect to background waves moves rapidly through the resonance mass, as would be expected from a Breit-Wigner amplitude. The mass and width are found to be $M = 1315 \pm 5$ MeV and $\Gamma = 115 \pm 15$ MeV. The differential cross-section is shown in Fig. 28 and exhibits a dip in the forward direction. The data seem to fit $\frac{d\sigma}{dt} \propto |t|\, e^{bt}$, with $b = 8.6 \pm 1.2\ \text{GeV}^{-2}$.

A similar analysis in the A_3 region is shown in Fig. 29, where the enhancement is assigned $J^P = 2^-$, and associated with an s-wave $f\pi$ system. The mass and width are given as $M = 1650 \pm 30$ MeV and $\Gamma = 300 \pm 50$ MeV. Again, the phase of the 2^- wave shows no mass dependence, like the A_1 (1^+) wave and <u>not</u> like the A_2 wave. The production distribution for the 2^- events, and the background events are shown in Fig. 30, where the enhancement data is shown to be more peripheral (with $b = 9.9 \pm 1.2$ GeV^{-2}) than the background ($b = 6.4 \pm 0.6$ GeV^{-2}).

We are left with several interesting questions — what are the A_1, A_3 enhancements? What is the production mechanisms for the A_2?

Several papers have appeared recently on the comparable process for incident K-mesons

$$Kp \rightarrow (K\pi\pi)p$$

in which a low mass $K\pi\pi$ enhancement is produced, called the Q-meson. We review below three studies of Q production in K^+p and K^-p reactions.

The $(K\pi\pi)$ mass spectrum from 8 GeV/c $K^{\pm}p$ data from a CERN collaboration bubble chamber experiment[21] is shown in Fig. 31. The mass distributions for strangeness +1 and -1 are very similar. The production angular distribution for the Q region (i.e., $1200 \leq m(K\pi\pi) < 1500$ MeV) is shown in Fig. 32. Marginal evidence for a cross-over in the differential cross-section for the particle and the anti-particle processes is presented. Strong conclusions on this question are hampered by poor statistics. However, they quote a difference in slope between Q^- and Q^+ production of $\Delta b = (1 \pm 1)$ GeV^{-2}.

Another bubble chamber experiment has studied Q^- production in $K^-p \rightarrow Q^-p$ at 14.3 GeV/c.[22] They have also made detailed comparisons with the $K^+p \rightarrow Q^+p$ data from the high statistics LBL 12 GeV/c experiment.[23] Chew-Low plots for

the three reactions studied in the Saclay experiment are shown in Fig. 33 for all the data, and in Fig. 34 with the selection of K* within the $K\pi\pi$ system, being imposed. Clear evidence of the low mass diffraction peak is seen in $K^- \to (K^-\pi^+\pi^-)$ and $K^- \to (\overline{K}^0\pi^-\pi^0)$ and is quite absent in the charge exchange reaction $K^- \to (\overline{K}^0\pi^+\pi^-)$. The $K\pi\pi$ mass spectrum for the two diffractive processes is shown again in Fig. 35, but with the additional selection that $M(p\pi^+) > 1340$ MeV, to reduce the contamination in the data from $K^-p \to K^*\Delta^{++}$.

The energy dependence of the cross-section is summarized in Fig. 36, as a function of $(K\pi\pi)$ mass. As we saw in the $\pi \to (3\pi)$ data, the s-dependence for $K\pi\pi$ masses near threshold is very similar to that observed for KN elastic scattering. The cross-section is observed to fall faster with energy as the $K\pi\pi$ mass increases; this appears to be a stronger effect in the $K \to (K\pi\pi)$ data than for $\pi \to (3\pi)$.

The differential cross-sections for $K^- \to Q^-$ are displayed in Fig. 37, where the distinct difference in slopes between the diffractive Q process and the Regge exchange $K \to K^*(1400)$ reaction is demonstrated. In Fig. 38, the slope dependence on the $(K\pi\pi)$ mass is given. Again this data is very similar to the $\pi \to (3\pi)$ data discussed above.

The $K^- \to Q^-$ cross-section is also compared to the LBL $K^+ \to Q^+$ data and the particle-antiparticle cross-over is observed — see Fig. 39.

Preliminary results were presented to the meeting from the high statistics wire chamber experiment at SLAC.[24] K^+p and K^-p data have been taken at 13 GeV/c with $\sim 40,000$ $K\pi\pi$ events of each strangeness with $M(K\pi\pi) < 1500$ MeV. The data had not been corrected for the acceptance of the spectrometer system and therefore only relative comparisons between K^+p and K^-p data were given. The results are summarized in Table 7.

A final comment on these diffraction dissociation processes. In most of their properties, they behave just like the corresponding elastic scattering reaction.[25] However, the helicity structure of the amplitudes seems to be one major area of difference. The elastic reactions (and the closely related vector meson photoproduction reactions) are observed to conserve s-channel helicity (SCHC) to 80-90% in the amplitude, while all evidence on the diffraction dissociation processes indicate no SCHC (and in fact no TCHC either!).[25] A new study of this phenomenon has been reported by a European bubble chamber collaboration[26] studying the following $\pi^{\pm}p$ interactions at 11 GeV/c:

$$\pi^+ p \rightarrow \pi^+(n\pi^+)$$

$$\pi^+ p \rightarrow \pi^+(p\pi^0)$$

$$\pi^- p \rightarrow \pi^-(p\pi^0)$$

$$\pi^- p \rightarrow (\pi^-\pi^-\pi^+)p$$

$$\pi^+ p \rightarrow (\pi^+\pi^-\pi^+)p$$

From studies of the azimuthal distributions in s-channel and t-channel coordinate systems they examined the validity of SCHC and TCHC for all the above reactions. Their conclusions are summarized in Table 8, and confirm the previous studies — (i.e., D.D. reactions <u>do not</u> conserve s-channel helicity!).

SINGLE PARTICLE INCLUSIVE STUDIES AT LOW ENERGY (i.e., $p < 50$ GeV/c

The high energy single particle inclusive experiments from NAL and the ISR have shown the existence of a large energy independent cross-section for the production of a low mass peak. This process is assumed to be diffractive excitation of the target or projectile and has a cross-section almost equal to the elastic scattering cross-section (i.e., $\sigma_{Diff} \sim 6$ mb). At the highest energies this low

mass peak in fact includes rather large masses — up to 7 GeV. The low mass peak is made up mainly from low multiplicity channels and the mean charged multiplicity is about half the total charge multiplicity for all processes. The multiplicity increases with increasing mass. For recent review see Ref. (27).

It is interesting to see what can be learned in similar processes at lower energies. Two groups have presented such data in the last year — the CERN-Serpukov collaboration[20] on the missing mass studies at 25 and 40 GeV/c for π^- and K^- beams, and a CERN bubble chamber experiment[28] on $\pi^+ p \rightarrow$ anything at 8, 16 and 23 GeV/c.

The x distribution (where $x = p_{11}/p_{11}^{max}$) for the π^+ at all three energies from the CERN HBC experiment[28] are shown in Figs. 40, 41 and 42. One can clearly observe the build up of the diffractive $x \approx 1$ peak as the energy increases, but it is interesting to notice that the peak is fed only by the 2 prong and the 4 prong topologies. They show that indeed only three exclusive reactions make up ~80% of the forward peak cross sections —

$$\pi^+ p \rightarrow n\pi^+\pi^+$$

$$\pi^+ p \rightarrow p\pi^+\pi^o$$

$$\pi^+ p \rightarrow \pi^+\pi^+\pi^- p \, .$$

The x-distributions for these processes are shown in Fig. 43 and 44, where events were selected to emphasize the diffractive phenomena, by choosing only those in which the π^+ is the only particle going forward in the c.m.s. and all other particles are going backwards. These contributions are shown as the heavy lines in Fig. 43 and 44. The shaded area in 44 represents events in which the proton is the only particle going backwards in the c.m.; these events correspond to dissociation of the incoming pion.

The sum of the contributions from the proton diffraction dissociation in the three exclusive reactions studied above, is compared to the diffractive peak obtained in the ISR p-p scattering experiments in Fig. 45. The ISR data were extrapolated to low transverse momenta (where the HBC data exists) under the assumption that

$$E \frac{d^3\sigma}{dp^3} = A(x)\, e^{-B(x)p_\perp^2}$$

and then integrated over the entire $p_\perp$ range. (The ISR data was taken for $0.7 < p_\perp < 1.2$ GeV/c.) They further assumed factorization of the diffraction dissociation process and scaled down the p-p cross-sections by

$$\left(\frac{\sigma^T_{pp}}{\sigma^T_{\pi^+p}}\right)^2 = 3.08$$

to compare to the π^+p cross-sections.

The errors associated with these extrapolations are large and indicated on Fig. 45 as the hatched band. The data indicate that within 20-30% one can observe scaling of the forward peak in energy range s = 31 to 2000 GeV^2.

This scaling conclusion is also verified by the CERN-Serpukov experiment.[20] The missing mass spectrum for π^-p collisions is shown in Fig. 46. Production of peaks in the A_1, A_2 and A_3 regions are observed but no further narrow high mass structure is seen. The invariant cross-sections $\frac{d^2\sigma}{dtdx}$, and $\frac{d\sigma}{dx}$ are compared in Fig. 47. The cross-sections scale (i.e., are seen to be independent of s for a given x) and the ratio $\frac{d\sigma}{dx}$ (25 GeV/c)/ $\frac{d\sigma}{dx}$ (40 GeV/c) for $-0.90 < x < -0.75$ is given as 1.01 ± 0.03. Also the slope of the cross-section in t is observed to be independent of energy — see Fig. 48.

The same apparatus was used in the study of the reaction $K^- p \rightarrow X^- p$ at 25 and 40 GeV/c. The missing mass distribution is shown in Fig. 49. The Q region is the only structure observed. The shape of the cross-section in t is observed to be energy independent and very similar to the $\pi^- p$ distribution (the dashed line) — see Fig. 50. The question of scaling was also addressed for the K^- experiment and the invariant cross-sections are shown in Fig. 51 as a function of x. The scaling hypothesis holds well for this reaction, too. The dashed line represents the invariant cross-section for the pion data and lies somewhat above the K^- cross-section. Howeve , if factorization is assumed then the π and K data are observed to be in good agreement —

$$\frac{\frac{d\sigma}{dx}(\pi^- p)}{\frac{d\sigma}{dx}(K^- p)} = \frac{\sigma^T_{incl}(\pi^- p)}{\sigma^T_{incl}(K^- p)}$$

$$1.20 \pm 0.07 \qquad 1.18 \pm 0.04$$

σ_T MEASUREMENT IN p-p SCATTERING IN PURE SPIN STATES

An interesting result has recently been obtained by a Michigan-ANL collaboration[29] using the new accelerated polarized proton beam at the AGS and a polarized proton target.

The total cross-section was measured in the four possible spin orientations, by alternately flipping the spin of the target and the beam. From rotational invariance principles the total cross-section for the two spin parallel states ($\uparrow\uparrow$ and $\downarrow\downarrow$) must be equal, and similarly for the two antiparallel states ($\uparrow\downarrow$ and $\downarrow\uparrow$). However, measurement of all four states permits studies of systematic errors, accidentals and other counting losses.

The difference between the parallel and anti-parallel configuration total cross-section was measured to be

$$\Delta\sigma = \sigma^T(\uparrow\uparrow) - \sigma^T(\uparrow\downarrow) = -1.7 \pm 2.0 \text{ mb.}$$

Thus they show that to within 5% both spin states have a scattering cross-section of 40 mb. This is the result expected for pomeron exchange dominance.

ACKNOWLEDGMENT

I would like to thank Prof. R. K. Carnegie for reading the manuscript, and for his helpful comments.

REFERENCES

1. D.W.G.S. Leith, "Diffractive Processes." Invited talk at the Berkeley APS Meeting of the Division of Particles and Fields, August, 1973 and Stanford Linear Accelerator Center Report No. SLAC-PUB-1330.
2. I. Ambats, et al., ANL/HEP 7329.
3. R.K. Carnegie, et al., (private communication).
4. V. Hungerbuehler, et al., Paper presented to the Berkeley APS Meeting of the Division of Particles and Fields, August, 1973.
5. Yu. M. Antipov, et al., Paper presented to the II International Conference on Elementary Particles, Aix-en-Provence, September (1973).
6. W.J. Robertson, W.D. Walker, and J.L. Davis, Phys. Rev. 7, 2554
7. P. Caso, et al., Paper submitted to the XIV International Conference on High Energy Physics, Vienna (1968). N.N. Biswas, et al., Phys. Rev. Letters 18, 273 (1967).
8. L. Barbaro Galtieri, private communication.
9. H. Alvensleben, et al., Paper submitted to the XVI International Conference on High Energy Physics, Batavia (1972).
10. R. Anderson, et al., Stanford Linear Accelerator Center Report No. SLAC-PUB-1085. J. Ballam, et al., Paper submitted to the XVI International Conference on High Energy Physics, Batavia (1972).
11. R. Anderson, et al., Stanford Linear Accelerator Center Report No. SLAC-PUB-1086.
12. H.J. Brsch, et al., Paper submitted to the International Symposium on Electron and Photon Interactions, Bonn (1973).
13. D.W.G.S. Leith, Stanford Linear Accelerator Center Report No. SLAC-PUB-1263.

14. G. Kane, Lectures delivered at McGill Summer School (1973).

15. M. Davier, Phys. Letters 40 B, 369 (1972).

16. G. Chadwick, et al., Stanford Linear Accelerator Center Report No. SLAC-PUB-1093.

17. S.D. Drell and K. Hiida, Phys. Letters 7, 199 (1961). R. Deck, Phys. Letters 13, 1969 (1964).

18. H. H. Bingham, et al., Paper submitted to the II International Conference on Elementary Particles at Aix-en-Provence, September (1973).

19. P. Bastien, et al., Paper submitted to the APS Division of Particles and Fields, Berkeley (1973).

20. Yu. M. Antipov, et al., Series of papers summarized by W. Kienzle in a paper presented to Joint CERN-IHEP Scientific Council, IHEP, Protrino, May 1973.

21. A. Apostalakis, et al., CERN/D.PHII/Phys-73-1.

22. R. Barloutaud, et al., D. PHPE 73-01, Saclay preprint.

23. P.J. Davies, et al., Phys. Rev. D 5, 2688 (1972).

24. R.K. Carnegie, et al., (Private communication).

25. D.W.G.S. Leith, "Diffraction Dissociation." Invited talk at the XVI International Conference on High Energy Physics, Batavia (1972) and Stanford Linear Accelerator Center Report No. SLAC-PUB-1141.

26. D. Evans, et al., Nuovo Cimento 14, 651 (1973).

27. D.W.G.S. Leith, "Diffractive Processes." Invited talk at the APS Division of Particles and Fields Meeting, Berkeley (1973). M. Jacob, "Multi-body Phenomena in Strong Interactions," TH-1683-CERN. T. Ferbel, "Recent Results from Hadronic Experiments at NAL," COO-3065-41.

28. R. Stroynowski, CERN 8 D. Ph. II/PHYS-73-13.

29. E.F. Parker, et al., UM-HE-73/23, (University of Michigan preprint).

TABLE 1

Results of fitting the cross sections. Fits of the type A exp(Bt) were made to the $\pi^{\pm}$ and $K^{\pm}$ cross sections for the range $0.05 \leq -t \leq 0.44$ GeV^2; the form A exp(Bt + Ct^2) was used for p and for $\bar{p}$ data over the intervals 0.05 to 1.0 GeV^2 and 0.05 to 0.44 GeV^2, respectively. The superscripts ± refer to the charge of the incident particle. Errors shown include statistical errors and uncertainty in the corrections for single Coulomb scattering.

Beam	p_{beam} (GeV/c)	A^+ mb/GeV^2	B^+ GeV^{-2}	C^+ GeV^{-4}	χ^2 per degree of freedom	A^- mb/GeV^2	B^- GeV^{-2}	C^- GeV^{-4}	χ^2 per degree of freedom
π	3	52.7 ± 1.2	7.03 ± .12		17/19	55.6 ± 1.1	7.61 ± .11		24/19
	3.65	44.8 ± 1.0	6.75 ± .12		20/19	51.5 ± 1.2	7.60 ± .12		14/19
	5	39.4 ± 0.7	6.94 ± .09		24/19	44.1 ± 0.7	7.66 ± .09		32/19
	6	37.1 ± 0.7	7.08 ± .10		14/19	40.2 ± 0.6	7.70 ± .08		33/19
K	3	17.5 ± 0.4	3.64 ± .11		24/19	38.7 ± 0.9	7.96 ± .13		16/19
	3.65	17.1 ± 0.5	4.12 ± .12		29/19	33.9 ± 0.8	7.57 ± .13		22/19
	5	16.2 ± 0.4	4.62 ± .10		23/19	28.9 ± 0.6	7.65 ± .10		24/19
	6	15.7 ± 0.4	4.87 ± .11		12/19	27.0 ± 0.7	7.57 ± .13		18/19
p	3	117.0 ± 2.3	7.80 ± .15	2.66 ± .20	19/26	299 ± 19	12.2 ± .8	-5.7 ± 2.4	28/18
	3.65	110.1 ± 2.4	8.29 ± .16	3.06 ± .22	23/26	264 ± 20	12.1 ± 1.0	-7.6 ± 3.0	12/18
	5	97.3 ± 2.0	8.46 ± .16	2.66 ± .22	22/26	194 ± 14	11.4 ± 1.0	-5.9 ± 2.9	15/18
	6	91.2 ± 1.9	8.63 ± .16	2.50 ± .23	31/26	198 ± 22	12.4 ± 1.5	-2.5 ± 4.0	19/18

TABLE 2

Momentum dependence of the forward slopes, B.

Fits were made to the form $B = B_0 + B' \ln(p_{lab}/4\ \mathrm{GeV/c})$.

Particle	B_0 GeV^{-2}	B' GeV^{-2}
π^+	6.94 ± .06	.18 ± .20
π^-	7.64 ± .05	.14 ± .18
K^+	4.20 ± .06	1.76 ± .20
K^-	7.72 ± .06	-.42 ± .24
p	8.22 ± .08	1.11 ± .29
$\bar{p}$	12.0 ± .5	-.6 ± 2.0

TABLE 3

Total elastic cross sections. The errors shown are dominated by the overall normalization uncertainty of ±4%; the particle-antiparticle relative uncertainty (including statistics) is about ±2.3% for $\pi^{\pm}$ and $K^{\pm}$ and ±3% for p and $\bar{p}$.

p GeV/c	$\sigma(\pi^+p)$ mb	$\sigma(\pi^-p)$ mb	$\sigma(K^+p)$ mb	$\sigma(K^-p)$ mb	σ (pp) mb	$\sigma(\bar{p}p)$ mb
3	7.84 ± .33	7.57 ± .31	4.81 ± .20	5.06 ± .21	17.2 ± .7	23.7 ± 1.0
3.65	6.88 ± .29	6.97 ± .29	4.26 ± .18	4.60 ± .19	15.2 ± .6	20.6 ± .9
5	5.79 ± .24	5.85 ± .24	3.53 ± .15	3.84 ± .16	12.7 ± .5	16.0 ± .7
6	5.33 ± .22	5.30 ± .22	3.26 ± .14	3.62 ± .15	11.5 ± .5	15.6 ± .8

TABLE 4

Parameters of elastic scattering (25 and 40 GeV/c)

	p_{inc}	Events	b	c	χ^2/pts.	$(d\sigma/dt)_{t=0}$	OTP	σ_{el}
π^-	25	8600	9.07 ± 0.32	2.4 ± 0.6	34/38	28.6 ± 2.6	31.6 ± 0.3	3.35 ± 0.06
	40	9300	9.63 ± 0.31	2.9 ± 0.5	38/38	29.8 ± 2.6	30.1 ± 0.3	3.32 ± 0.06
K^-	25	12400	8.71 ± 0.21	2.4 ± 0.4	34/38	19.9 ± 1.6	22.1 ± 0.2	2.46 ± 0.03
	40	15400	8.90 ± 0.23	2.8 ± 0.4	36/38	19.0 ± 1.5	21.2 ± 0.2	2.33 ± 0.03
P^-	25	12000	12.8 ± 0.4	2.3 ± 0.8	25/33	108 ± 9	112 ± 1	8.7 ± 0.2
	40	4400	12.2 ± 0.7	2.0 ± 1.4	28/33	85 ± 9	101 ± 1	7.2 ± 0.3

TABLE 5

t-dependence of shrinkage in elastic $\pi^- p$, $K^- p$, and $\bar{p}p$ scattering (parameter k)

	t = 0	-0.1	-0.2	-0.3	-0.4
π^-	0.72 ± 0.18	0.52 ± 0.12	0.35 ± 0.08	0.23 ± 0.05	0.08 ± 0.06
K^-	0.73 ± 0.16	0.54 ± 0.12	0.38 ± 0.08	0.20 ± 0.06	0.00 ± 0.08
$\bar{P}$	-0.8 ± 0.2	-1.1 ± 0.1	-1.0 ± 0.1	-1.4 ± 0.2	-2.0 ± 0.2

TABLE 6

Slope b of differential cross-section $d\sigma/dt$, integrated cross-section σ and exponent n of the energy dependence for the reaction $\pi^- p \rightarrow \pi^- \pi^- \pi^+ p$ versus 3π mass. The systematic errors are given in parentheses.

	25 GeV/c		40 GeV/c		11-40 GeV/c
$m_{3\pi}$ [GeV]	b [GeV/c^{-2}]	σ [μb]	b [GeV/c^{-2}]	σ [μb]	n [$\sigma \propto p_{inc}^n$]
0.8 - 1.0	14.3 ± 0.8	36.6 ± 3.3 (3.7)	14.9 ± 0.6	37.3 ± 2.2 (3.7)	-0.31 ± 0.11
1.0 - 1.1	11.7 ± 0.5	51.6 ± 3.6 (5.2)	12.6 ± 0.5	50.9 ± 2.3 (5.2)	-0.29 ± 0.10
1.1 - 1.2	10.0 ± 0.4	68.4 ± 3.4 (7.0)	10.7 ± 0.4	64.5 ± 2.2 (6.5)	
1.2 - 1.3	8.3 ± 0.4	71.7 ± 3.1 (7.6)	8.5 ± 0.4	63.5 ± 2.1 (6.4)	-0.29 ± 0.10
1.3 - 1.4	7.3 ± 0.4	56.5 ± 2.6 (7.0)	6.1 ± 0.4	53.9 ± 2.1 (5.5)	
1.4 - 1.5	7.2 ± 0.6	35.6 ± 2.3 (5.0)	7.2 ± 0.5	30.6 ± 1.5 (3.1)	-0.42 ± 0.11
1.5 - 1.6	6.2 ± 0.6	35.3 ± 2.1 (5.2)	7.2 ± 0.5	33.2 ± 1.5 (3.4)	
1.6 - 1.8	6.6 ± 0.5	80.9 ± 3.8 (11.0)	7.2 ± 0.3	72.5 ± 2.1 (7.4)	-0.50 ± 0.11
1.8 - 2.0	5.1 ± 0.6	48.5 ± 3.2 (7.0)	5.6 ± 0.6	44.0 ± 2.1 (4.6)	

TABLE 7

The difference in slope for $K^+p \rightarrow Q^+p$ and $K^-p \rightarrow Q^-p$

Momentum (GeV/c)	Elastic Scattering Slope Difference (GeV^{-2})	Q^+ Slope Difference (GeV^{-2})	Ref.
8	2.70 ± 0.16	1 ± 1	(20)
12-14	1.6 ± 0.1	1.7 ± 0.35	(21)
13		1.1 ± 0.4	(23)

TABLE 8

Study of s-channel and t-channel helicity conservation in inelastic diffractive processes

Reaction	SCHC	TCHC
$\pi^+ p \rightarrow \pi^+ (n\pi^+)$	NO	NO
$\pi^+ p \rightarrow \pi^+ (p\pi^0)$	NO	NO
$\pi^+ p \rightarrow (\pi^+\pi^-\pi^+) p$	NO	NO
$\pi^- p \rightarrow \pi^- (p\pi^0)$	NO	NO
$\pi^- p \rightarrow (\pi^-\pi^+\pi^-) p$	NO	--

FIGURE CAPTIONS

1. Differential cross-section for scattering of $\pi^{\pm}$, $K^{\pm}$, $p^{\pm}$ on protons, at 3 GeV/c.

2. Differential cross-section for scattering of $\pi^{\pm}$, $K^{\pm}$, $p^{\pm}$ on protons, at 3.65 GeV/c.

3. Differential cross-section for scattering of $\pi^{\pm}$, $K^{\pm}$, $p^{\pm}$ on protons, at 5 GeV/c.

4. Differential cross-section for scattering of $\pi^{\pm}$, $K^{\pm}$, $p^{\pm}$ on protons, at 6 GeV/c.

5. Comparison of the t=0 slopes of the differential cross-sections of the ANL experiment (Ref. 2), with all available data.

6. Comparison of the crossover points, t_c, for pions, kaons and protons. The effective radius r (in fermis) was calculated by taking the position of the first zero of $J_0(r(-t)^{1/2})$ at $t = \langle t_c \rangle$. The errors on the plotted points show only the statistical uncertainty, while those for $\langle -t_c \rangle$ and r reflect both statistical and the ±1.5% uncertainty in the relative particle-antiparticle normalization.

7. Production angular distribution for $p^{\pm}p$ elastic scattering at 10.4 GeV/c.

8. Production angular distribution for $K^{\pm}p$ elastic scattering at 10.4 GeV/c.

9. Slope of the elastic differential cross-section for $K^{\pm}p$ scattering in the t-range $0.05 < t < 0.25$ GeV^2. The data comes from an ANL experiment (Ref. 2), a SLAC experiment (Ref. 3) and a CERN-Serupkov collaboration (Ref. 5).

10. Production angular distribution for elastic π^-p and Σ^-p scattering at 23 GeV/c.

11. Differential elastic cross-section for $\pi^- p$, $K^- p$, and $\bar{p}p$ scattering at 25 and 40 GeV/c.

12. π-π scattering angle distributions in the dipion rest system (θ), and invariant four-momentum transfer squared in π-π scattering for the reactions $\pi^- + p \rightarrow \pi^- \pi^+ + n$ and $\pi^- p \rightarrow \pi^- + \pi^- + \Delta^{++}$. Note that the scales for the sections of $M(\pi\pi)$ are nonlinear.

13. Elastic and total cross-section determinations for $\pi^- - \pi^+$ and $\pi^- - \pi^-$ scattering as a function of the dipion invariant mass.

14. The differential cross-section for $\gamma p \rightarrow \varphi p$ at 2 GeV.

15. The energy dependence of the cross-section for $\gamma p \rightarrow \varphi p$ at $t = 0.6$ GeV^2.

16. The elastic pp differential cross-section for momenta between 3 and 16 GeV/c.

17. Schematic representation of the amplitudes in the two-component pomeron model of Kane (Ref. 14).

18. Effective mass distribution for the reaction $\pi^- n \rightarrow \pi^- (p\pi^-)$ at 15 GeV/c for (a) those events with $t' < 0.08$ GeV^2 and (b) for $0.08 < t' < 1.0$ GeV^2.

19. Production angular distributions for the reaction $\pi^- n \rightarrow \pi^- (p\pi^-)$ at 15 GeV/c, with (a) $M(p\pi^-) < 1400$ MeV, and (b) $1400 < M(p\pi^-) < 2000$ MeV.

20. The effective mass spectrum for (3π) in the reaction $\pi^- d \rightarrow \pi^- \pi^+ \pi^- d$ at 15 GeV/c.

21. The $\pi^+ \pi^-$ mass distribution from the reaction $\pi^- d \rightarrow \pi^- \pi^+ \pi^- d$ at 15 GeV/c.

22. The (3π) and (2π) effective mass distributions from the CERN IHEP experiment on $\pi^- p \rightarrow \pi^- \pi^+ \pi^- p$ at 40 GeV/c.

23. The energy dependence of the cross-section for $\pi^- p \rightarrow A_1 p$, where $A_1 \rightarrow \rho\pi$ is defined as $1000 < M(3\pi) < 1200$ MeV.

24. The energy dependence of the cross-section for $\pi^- p \rightarrow A_2 p$, where $A_2 \rightarrow \rho\pi$ is defined as $1200 < M(3\pi) < 1400$ MeV.

25. The energy dependence of the cross-section for $\pi^- p \rightarrow A_3 p$, where $A_3 \rightarrow f\pi$ is defined as $1500 < M(3\pi) < 1800$ MeV.

26. The energy dependence of the 3π amplitudes in the A_1 region.

27. The energy dependence of the 3π amplitudes in the A_2 region.

28. The differential cross-section for $\pi^- p \rightarrow A_2 p$ ($A_2 \rightarrow \rho\pi$) at 25 and 40 GeV/c.

29. The energy dependence of the 3π amplitudes in the A_3 region.

30. The differential cross-section for $\pi^- p \rightarrow A_3 p$ ($A_3 \rightarrow f\pi$) at 40 GeV/c.

31. The effective mass distribution for the ($K\pi\pi$) system in $K^+ p \rightarrow K^{*0}\pi^+ p$ and $K^- p \rightarrow \overline{K}^{*0}\pi^- p$ at 8 GeV/c.

32. The differential cross-section for the processes $K^+ p \rightarrow Q^+ p$ and $K^- p \rightarrow Q^- p$ at 8 GeV/c.

33. The Chew-Low plots for the reactions $K^- p \rightarrow K^- p\pi^+\pi^-$, $\overline{K}^0 p\pi^-\pi^0$ and $\overline{K}^0 n\pi^+\pi^-$ at 14 GeV/c.

34. The Chew-Low plots for the reactions $K^- p \rightarrow K^- p\pi^+\pi^-$, $\overline{K}^0 p\pi^-\pi^0$ and $\overline{K}^0 n\pi^+\pi^-$ at 14 GeV/c, but requiring a K^* within the ($K\pi\pi$) system.

35. The ($K\pi\pi$) mass distribution in $K^- p \rightarrow K^- p\pi^+\pi^-$, $\overline{K}^0 p\pi^-\pi^0$ at 14 GeV/c.

36. The energy dependence of the cross-section of $K^- p \rightarrow K^-\pi^+\pi^- p$ as a function of $M(K\pi\pi)$.

37. The production angular distribution for $K^- p \rightarrow Q^- p$ at 14 GeV/c.

38. The mass dependence of the slope of the differential cross-section in $K^- p \rightarrow Q^- p$ at 14 GeV/c.

39. The differential cross-section for $K^\pm p \rightarrow Q^\pm p$ at energies around 14 GeV/c.

40. The x-distribution for the fast forward π^+, in $\pi^+ p \rightarrow \pi^+$ + (anything) at 8 GeV/c. The distribution is broken down topology by topology.

41. The x-distribution for the fast forward π^+, in $\pi^+ p \rightarrow \pi^+$ + (anything) at 16 GeV/c. The distribution is broken down topology by topology.

42. The x-distribution for the fast forward π^+, in $\pi^+ p \rightarrow \pi^+$ + (anything) at 23 GeV/c. The distribution is broken down topology by topology.

43. The x-distribution for the forward π^+ in the reactions $\pi^+ p \rightarrow p\pi^+\pi^o$, $n\pi^+\pi^+$ at 8, 16 and 23 GeV/c.

44. The x-distribution for the forward π^+ and backward proton in the reaction $\pi^+ p \rightarrow \pi^+\pi^-\pi^+ p$ at 8, 16 and 23 GeV/c.

45. The invariant cross-section, $\frac{d\sigma}{dt}$, for the proton dissociation in $\pi^+ p \rightarrow \pi^+$ (anything) at 8, 16 and 23 GeV/c. The ISR pp data are also shown, after being extrapolated to small $p_\perp$ and adjusted for the difference in $\pi^+ p$ and pp total cross-sections (see text for details).

46. The missing mass distribution in $\pi^- p \rightarrow pX^-$ at 25 and 40 GeV/c.

47. The invariant cross-section as a factor of x, for $\pi^- p \rightarrow pX^-$ at 250 and 40 GeV/c.

48. The slope of the differential cross-section for $\pi^- p \rightarrow pX^-$ at 25 and 40 GeV/c as a function of x.

49. The missing mass distribution in $K^- p \rightarrow pX^-$ at 25 and 40 GeV/c.

50. The slope of the production angular distribution in $K^- p \rightarrow pX^-$ at 25 and 40 GeV/c, as a function of x.

51. The invariant cross-section for the process $K^- p \rightarrow pX^-$ at 25 and 40 GeV/c, as a function of x.

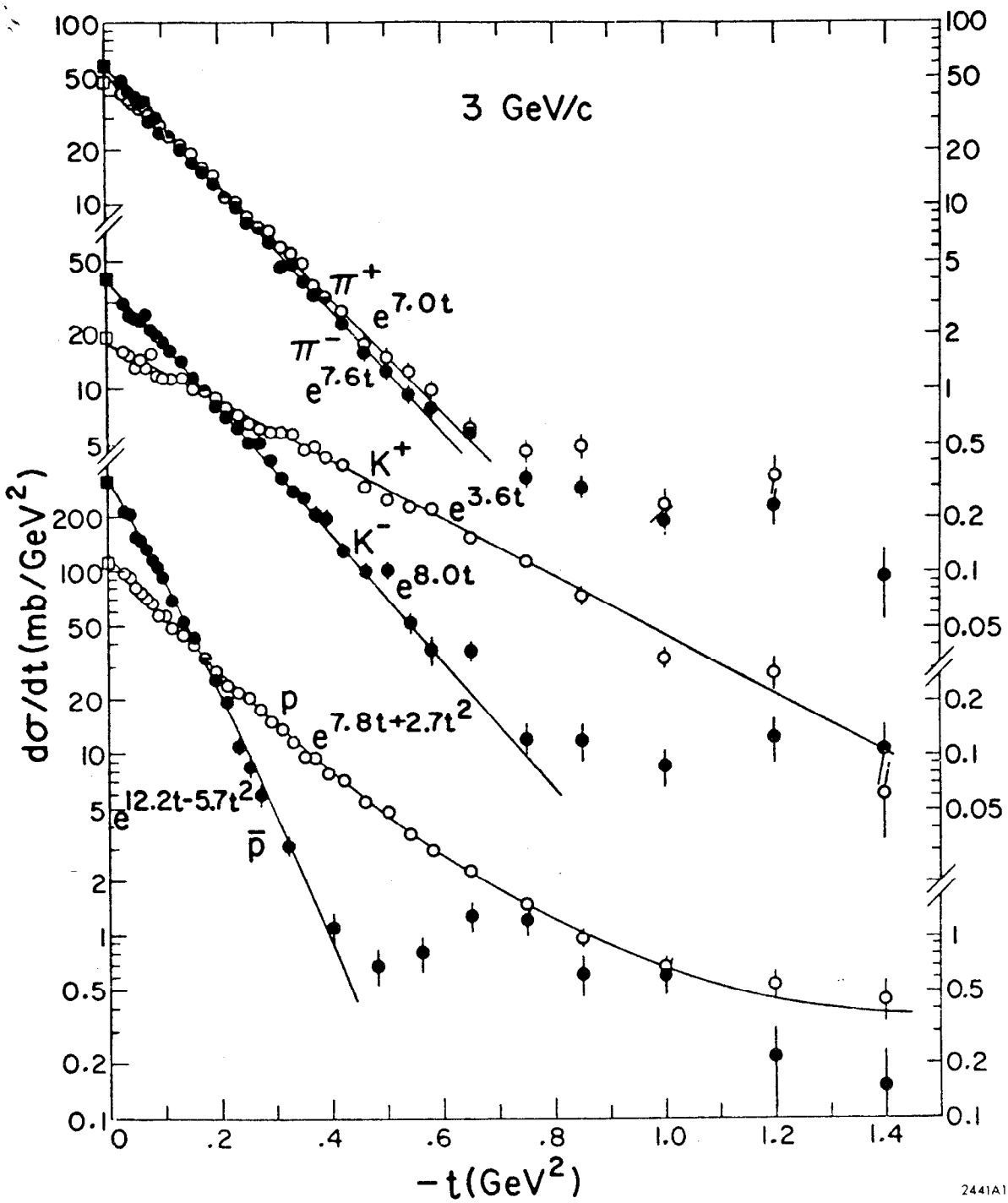
3 GeV/c
π^+
$e^{7.0t}$
π^-
$e^{7.6t}$
K^+
$e^{3.6t}$
K^-
$e^{8.0t}$
p
$e^{7.8t+2.7t^2}$
$\bar{p}$
$e^{12.2t-5.7t^2}$
$d\sigma/dt\,(mb/GeV^2)$
$-t\,(GeV^2)$
2441A1

Fig. 1

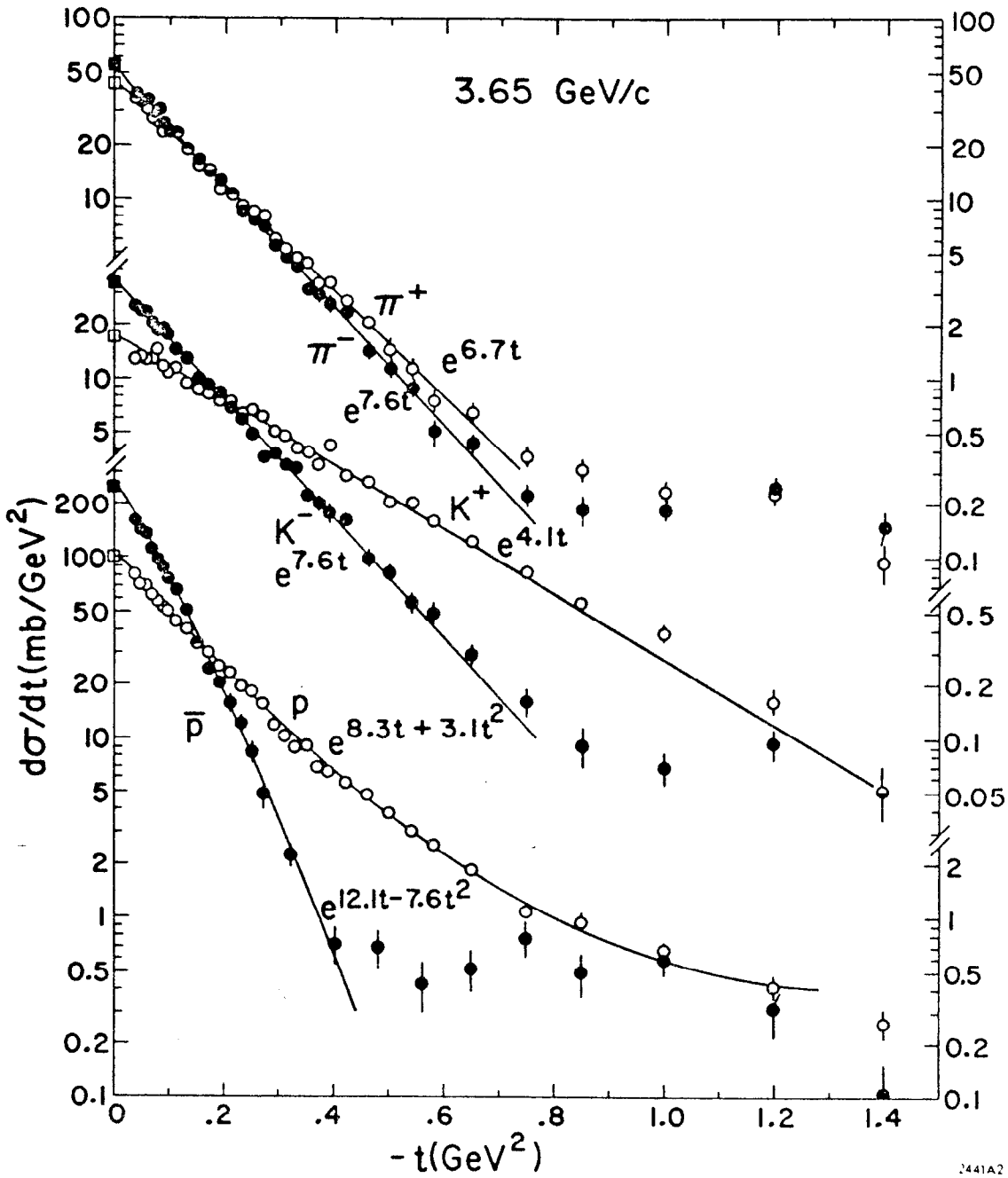
3.65 GeV/c
π^+
π^-
$e^{6.7t}$
$e^{7.6t}$
K^+
K^-
$e^{4.1t}$
$e^{7.6t}$
p
$\bar{p}$
$e^{8.3t+3.1t^2}$
$e^{12.1t-7.6t^2}$
$d\sigma/dt(mb/GeV^2)$
$-t(GeV^2)$
2441A2

Fig. 2

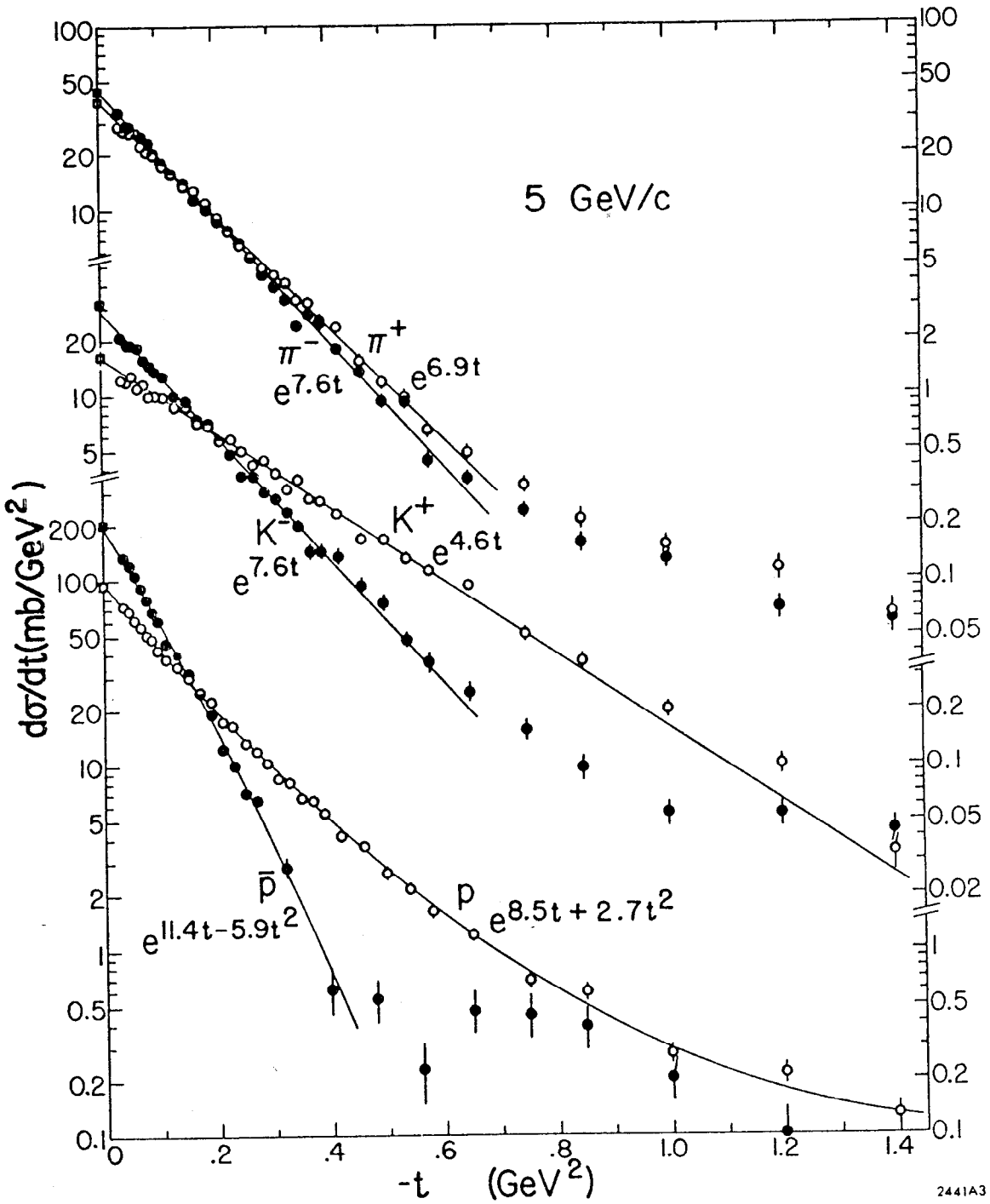
5 GeV/c
π^+
$e^{6.9t}$
π^-
$e^{7.6t}$
K^+
$e^{4.6t}$
K^-
$e^{7.6t}$
p
$e^{8.5t+2.7t^2}$
$\bar{p}$
$e^{11.4t-5.9t^2}$
$d\sigma/dt(mb/GeV^2)$
$-t$ (GeV^2)
2441A3

Fig. 3

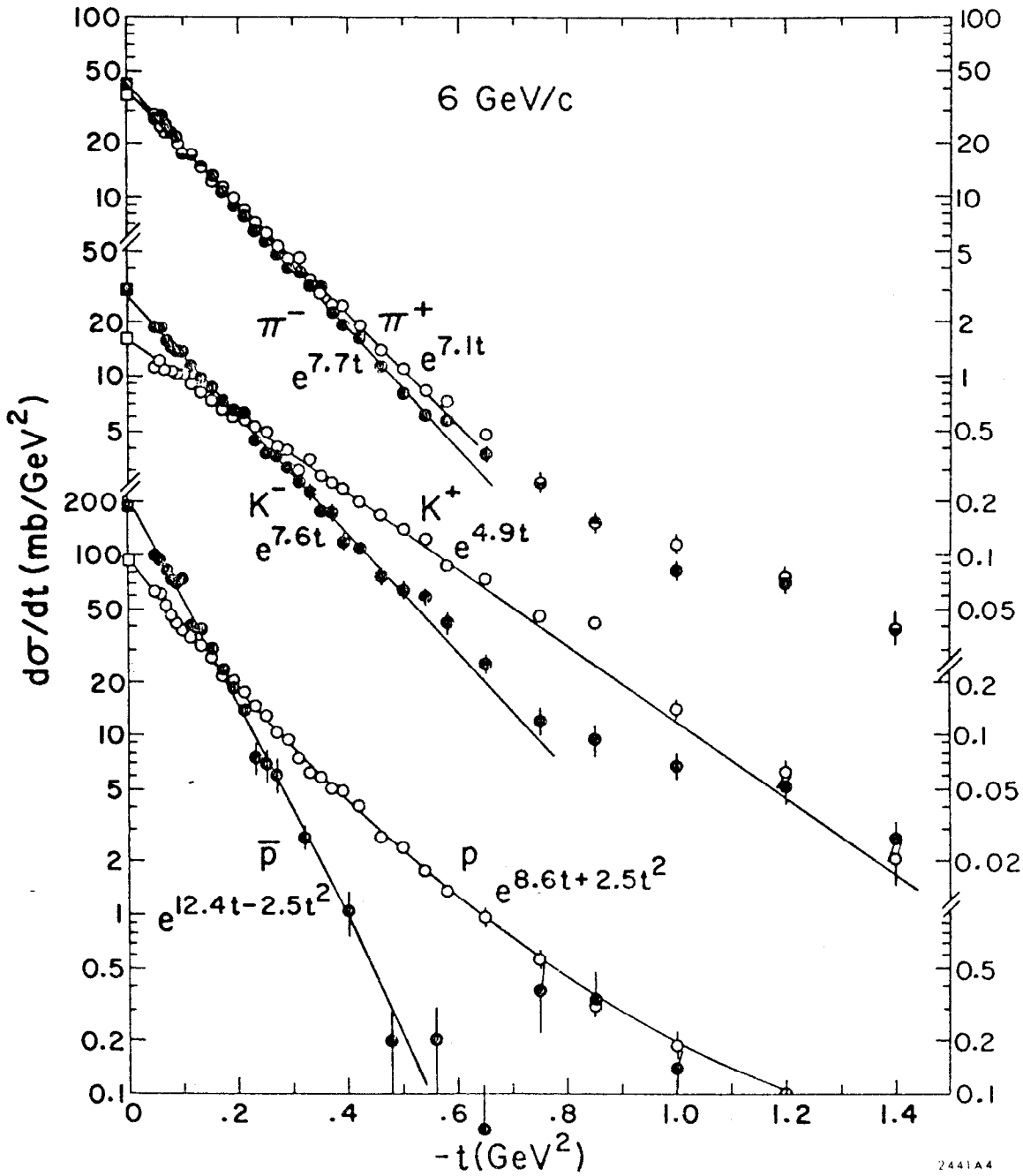
6 GeV/c
π^-
π^+
$e^{7.7t}$
$e^{7.1t}$
K^-
K^+
$e^{7.6t}$
$e^{4.9t}$
$\bar{p}$
p
$e^{12.4t-2.5t^2}$
$e^{8.6t+2.5t^2}$
$d\sigma/dt$ (mb/GeV^2)
$-t$(GeV^2)
2441A4

Fig. 4

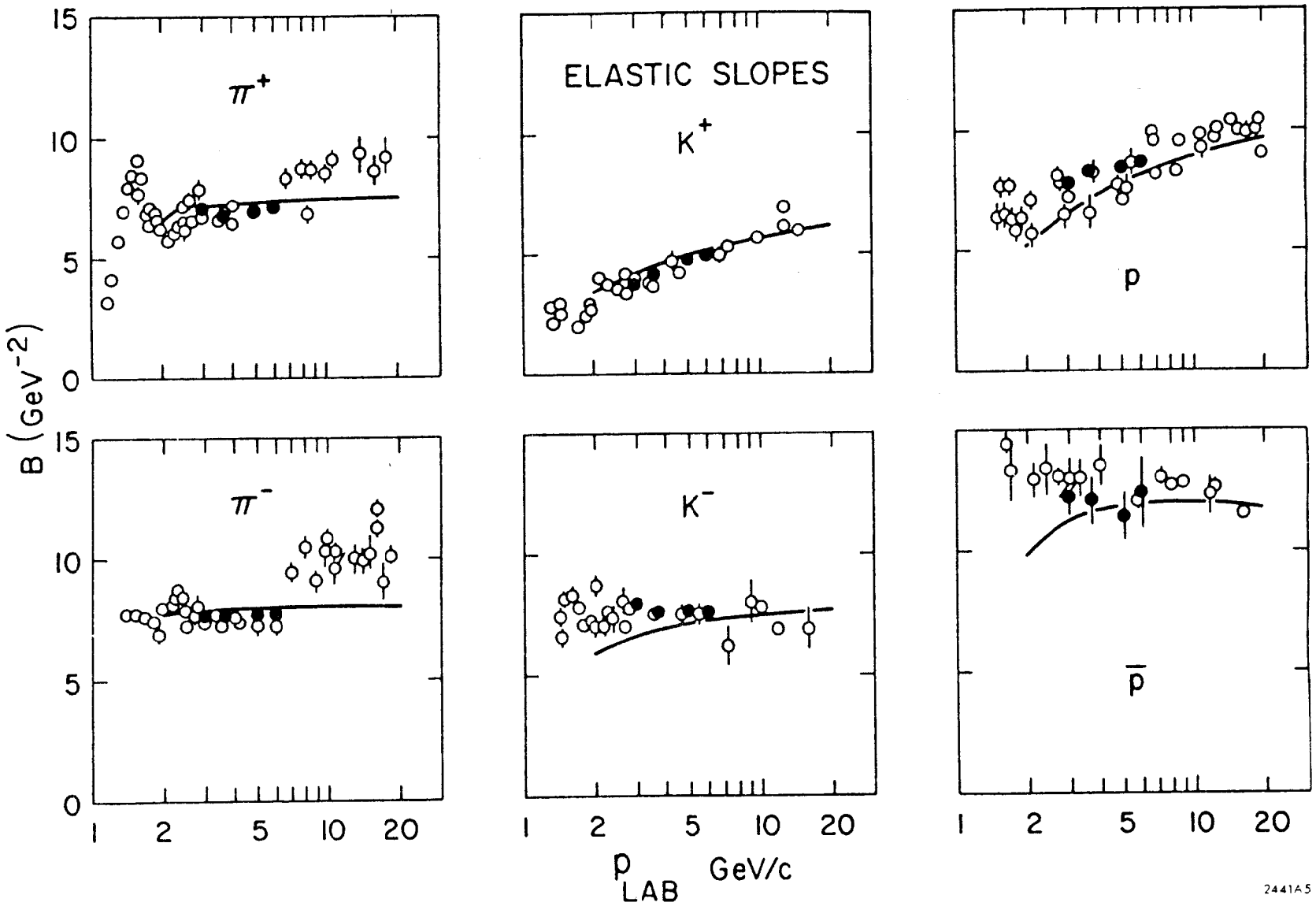
ELASTIC SLOPES
π^+
K^+
p
π^-
K^-
$\bar{p}$
B (GeV^{-2})
p_{LAB} GeV/c
0
5
10
15
1
2
5
10
20
2441A5

Fig. 5

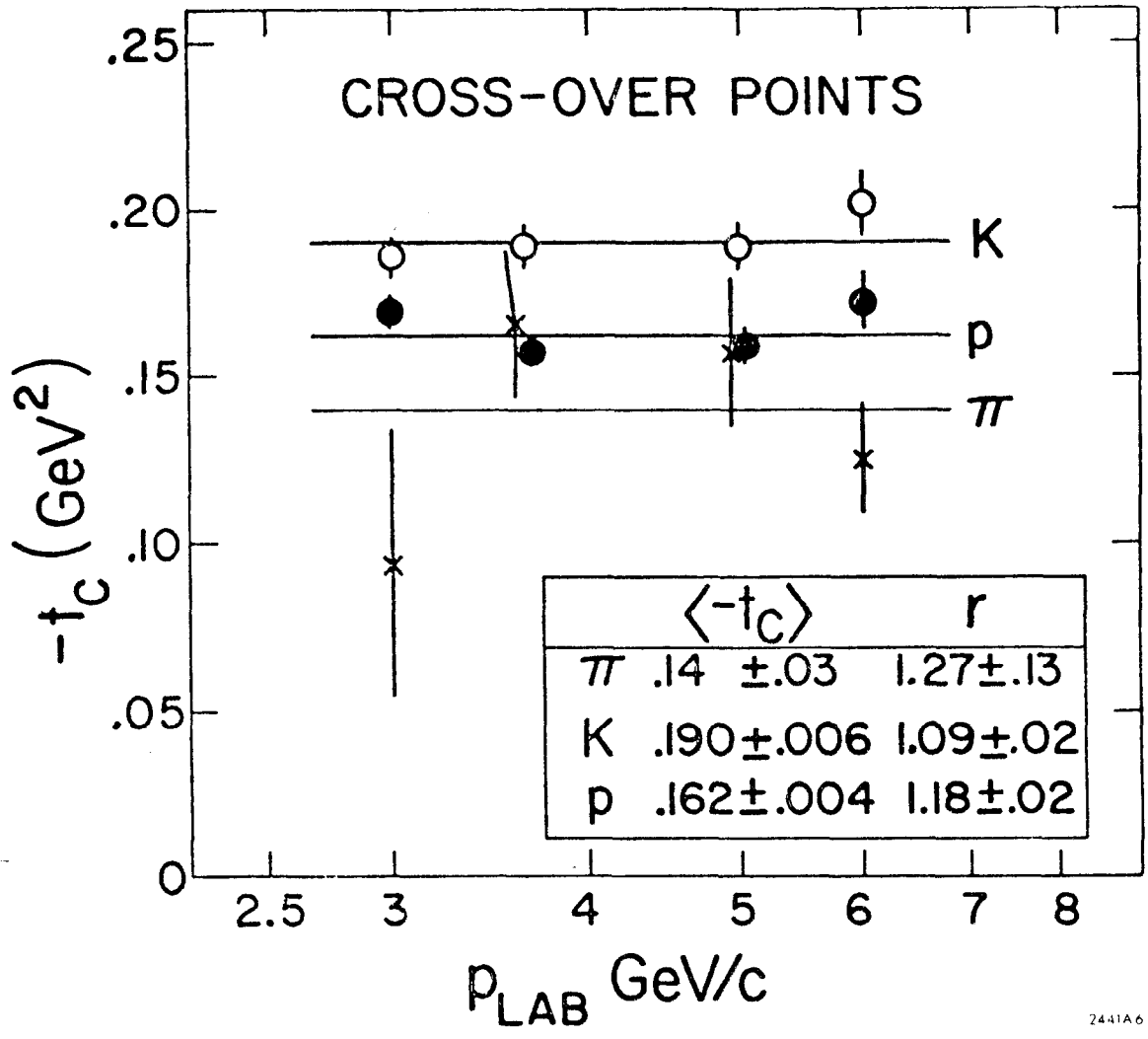
CROSS-OVER POINTS
K
p
π
$-t_c$ (GeV^2)
.25
.20
.15
.10
.05
0
2.5
3
4
5
6
7
8
p_{LAB} GeV/c
⟨$-t_c$⟩ r
π .14 ±.03 1.27±.13
K .190±.006 1.09±.02
p .162±.004 1.18±.02
2441A6

Fig. 6

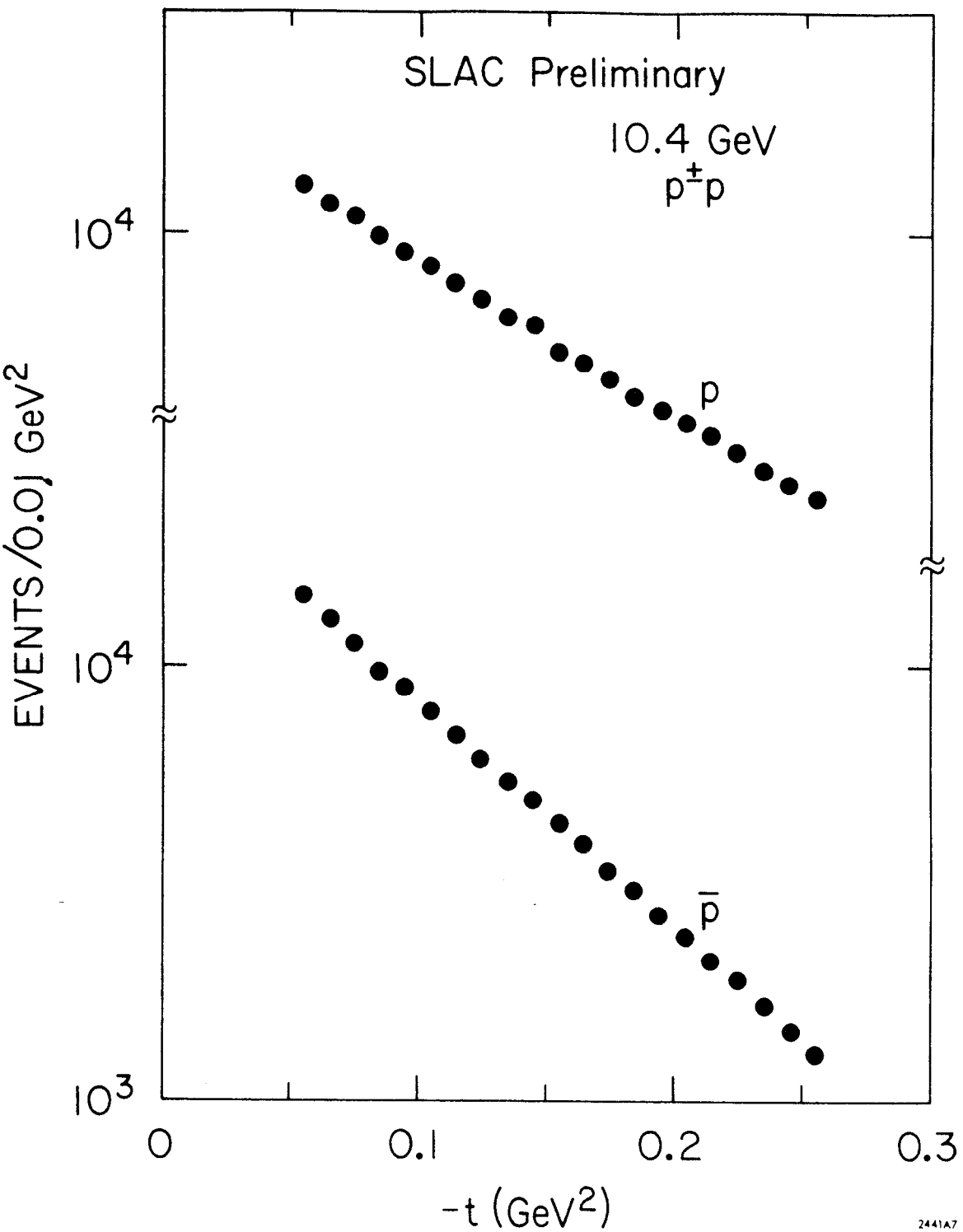
SLAC Preliminary
10.4 GeV
p±p
p
p̄
EVENTS/0.01 GeV²
10⁴
10⁴
10³
0
0.1
0.2
0.3
-t (GeV²)
2441A7

Fig. 7

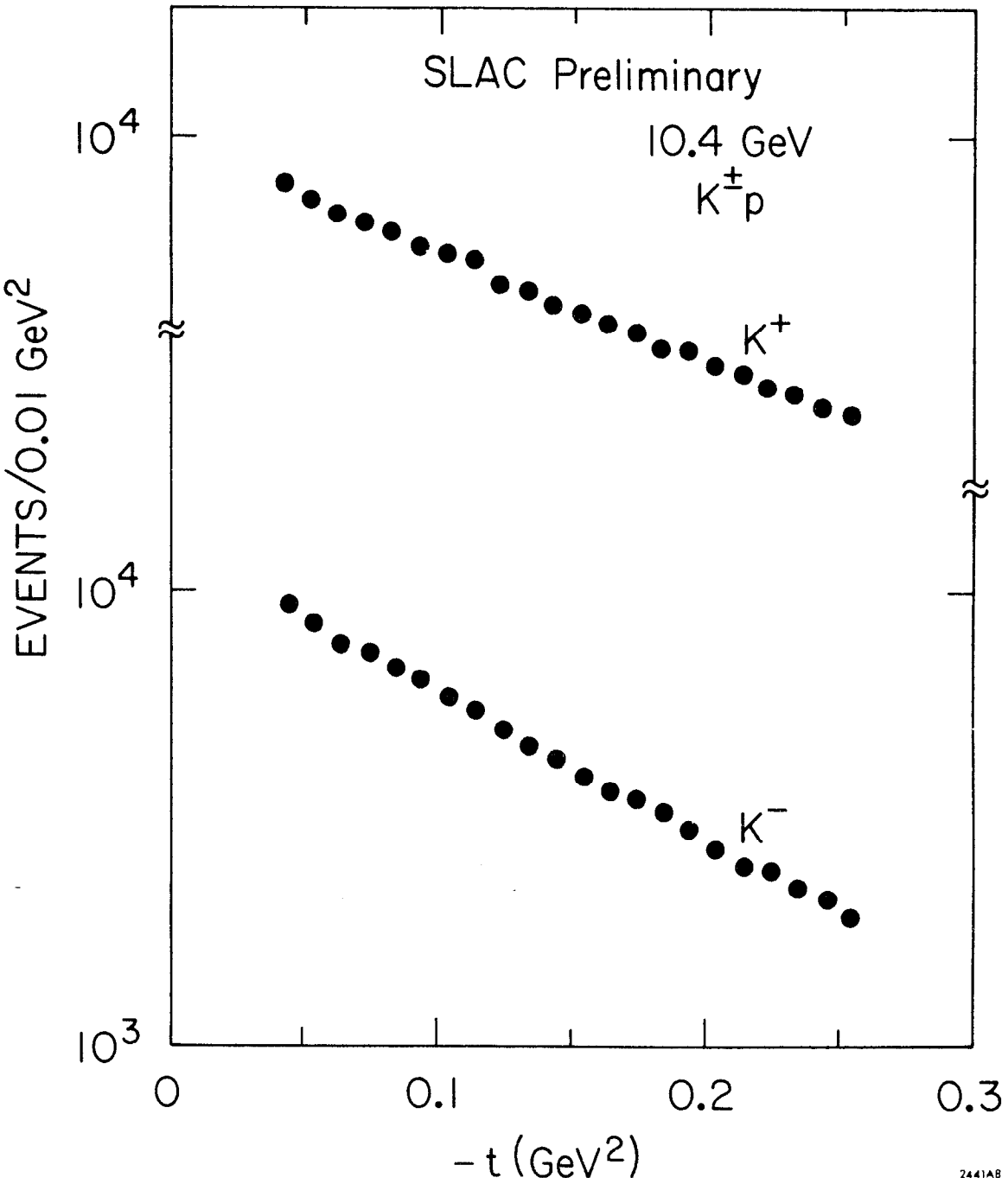
SLAC Preliminary
10.4 GeV
K±p
K+
K−
EVENTS/0.01 GeV2
10^4
10^4
10^3
0
0.1
0.2
0.3
−t (GeV2)
2441A8

Fig. 8

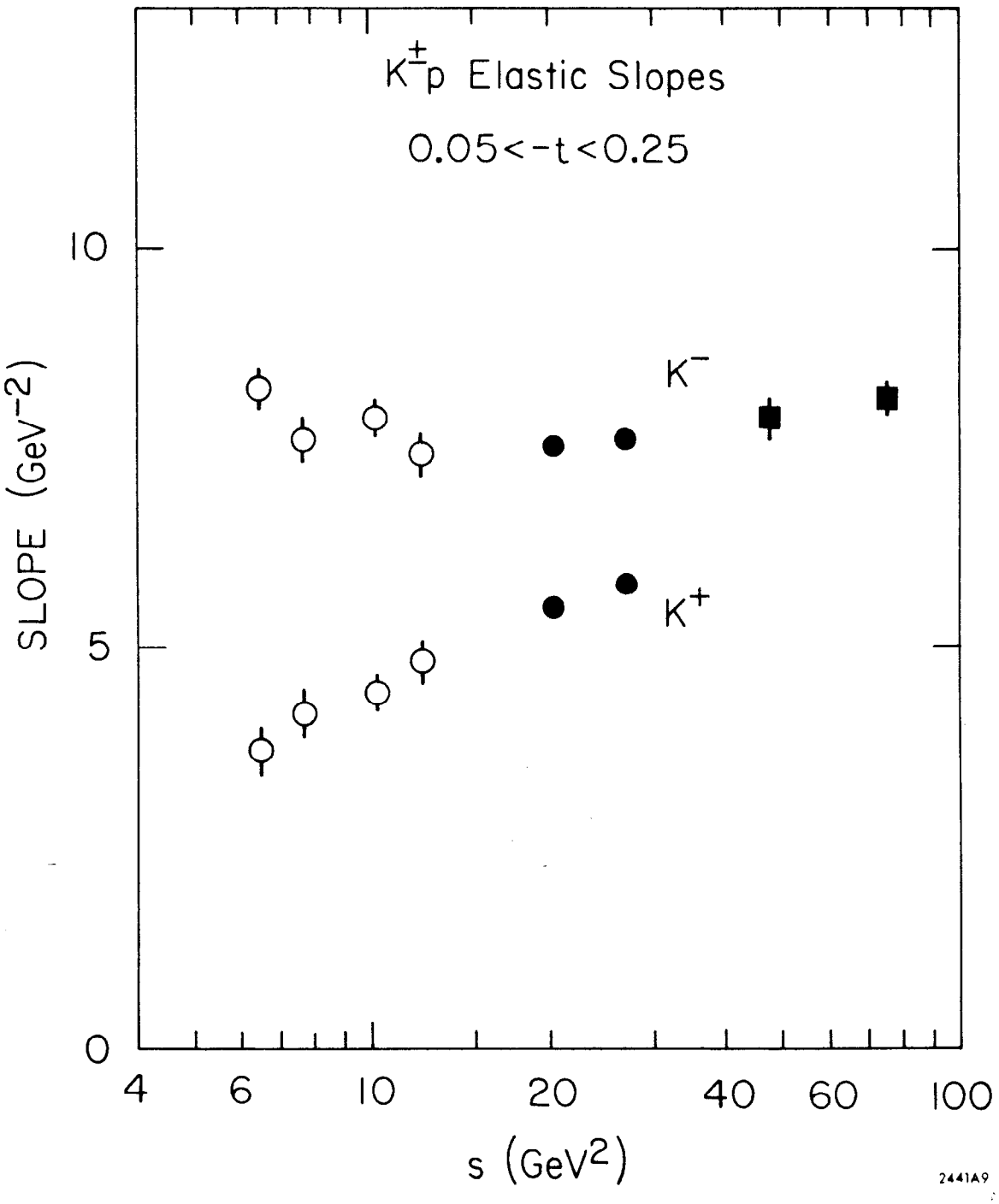
K±p Elastic Slopes
0.05<-t<0.25
SLOPE (GeV-2)
10
5
0
K-
K+
4
6
10
20
40
60
100
s (GeV2)
2441A9

Fig. 9

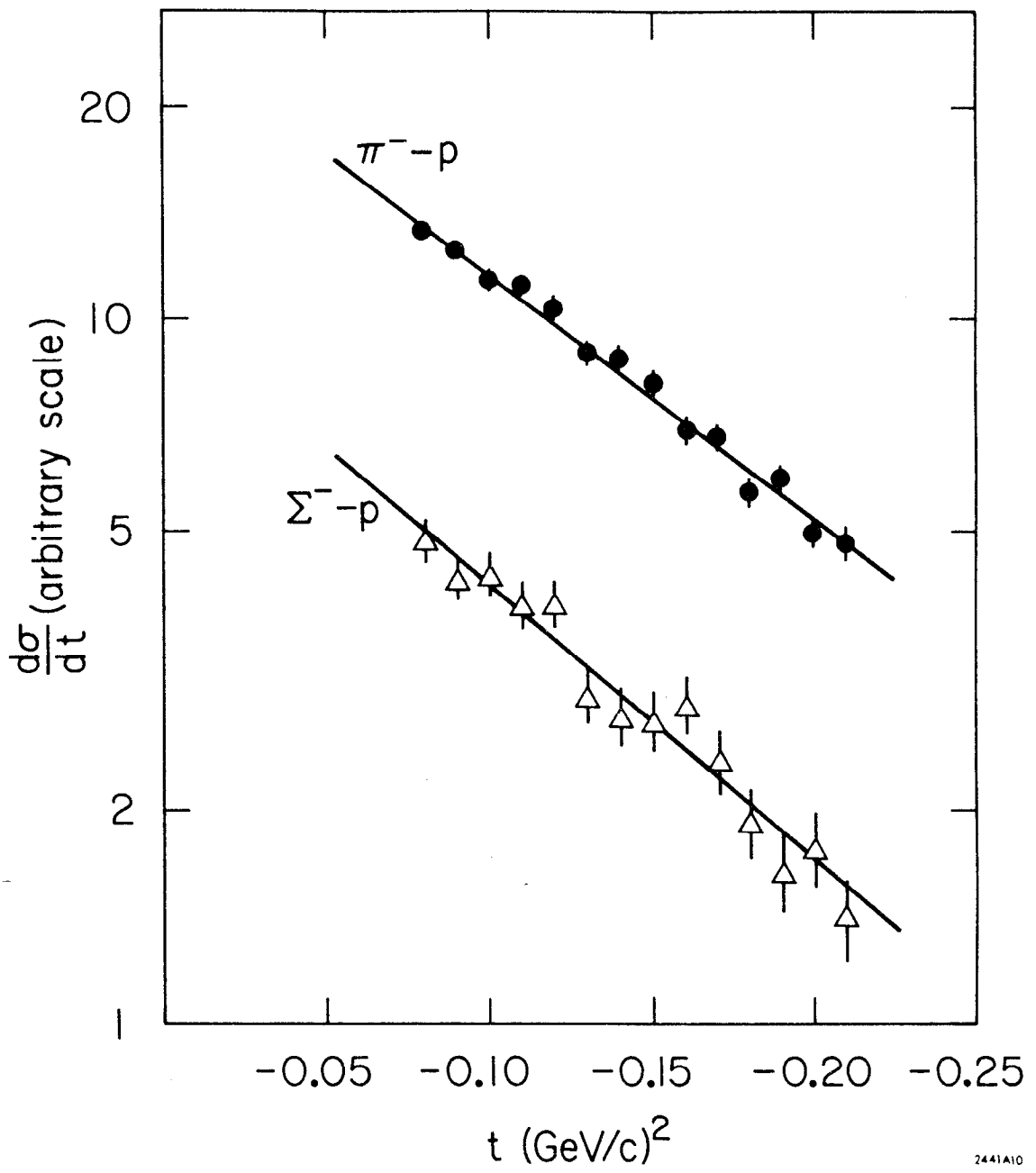
20
10
5
2
1
$\frac{d\sigma}{dt}$ (arbitrary scale)
$\pi^- - p$
$\Sigma^- - p$
-0.05
-0.10
-0.15
-0.20
-0.25
t (GeV/c)^2
2441A10

Fig. 10

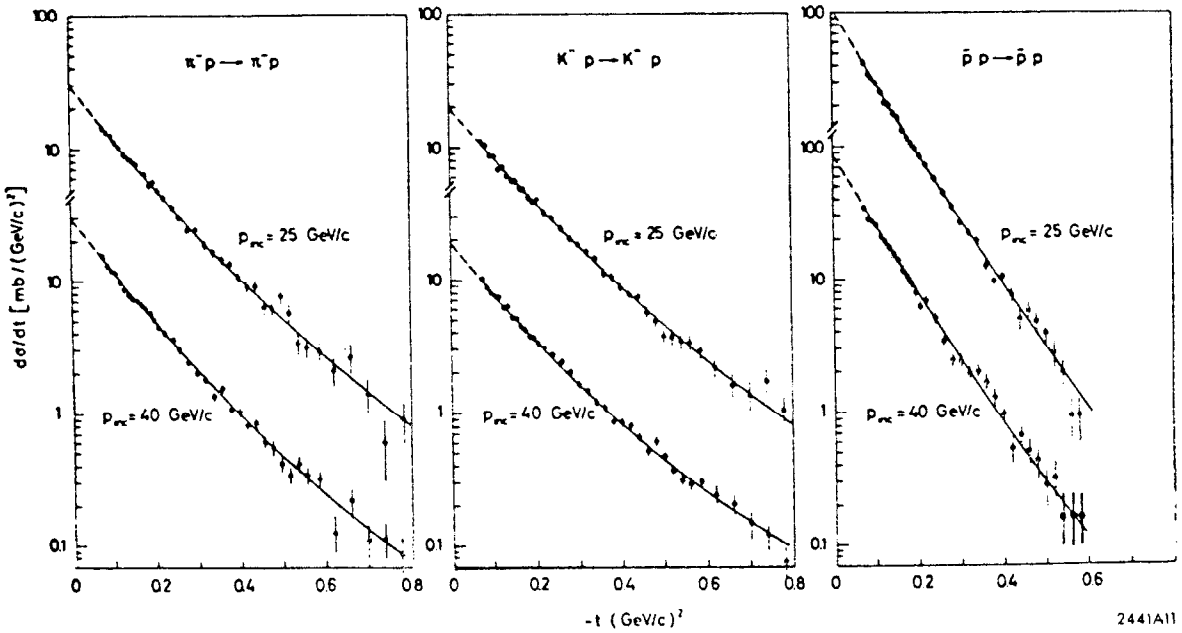
π⁻p → π⁻p
K⁻p → K⁻p
p̄p → p̄p
p_inc = 25 GeV/c
p_inc = 40 GeV/c
dσ/dt [mb/(GeV/c)²]
-t (GeV/c)²
2441A11

Fig. 11

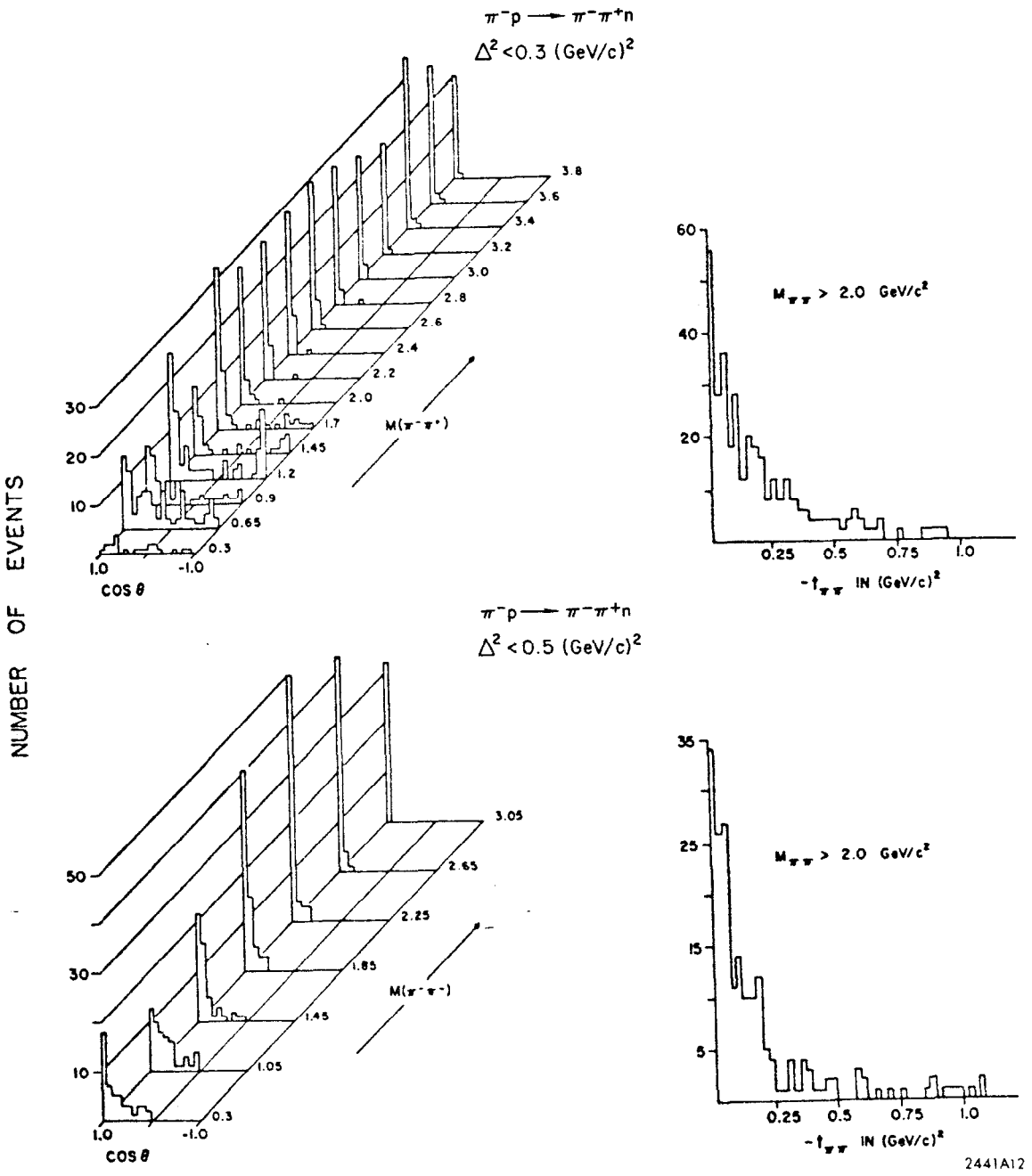
$\pi^- p \longrightarrow \pi^- \pi^+ n$
$\Delta^2 < 0.3$ (GeV/c)^2
NUMBER OF EVENTS
30
20
10
3.8
3.6
3.4
3.2
3.0
2.8
2.6
2.4
2.2
2.0
1.7
1.45
1.2
0.9
0.65
0.3
$M(\pi^-\pi^+)$
1.0
-1.0
COS θ
60
40
20
$M_{\pi\pi} > 2.0$ GeV/c^2
0.25
0.5
0.75
1.0
$-t_{\pi\pi}$ IN (GeV/c)^2
$\pi^- p \longrightarrow \pi^- \pi^+ n$
$\Delta^2 < 0.5$ (GeV/c)^2
50
30
10
3.05
2.65
2.25
1.85
1.45
1.05
0.3
$M(\pi^-\pi^-)$
1.0
-1.0
COS θ
35
25
15
5
$M_{\pi\pi} > 2.0$ GeV/c^2
0.25
0.5
0.75
1.0
$-t_{\pi\pi}$ IN (GeV/c)^2
2441A12

Fig. 12

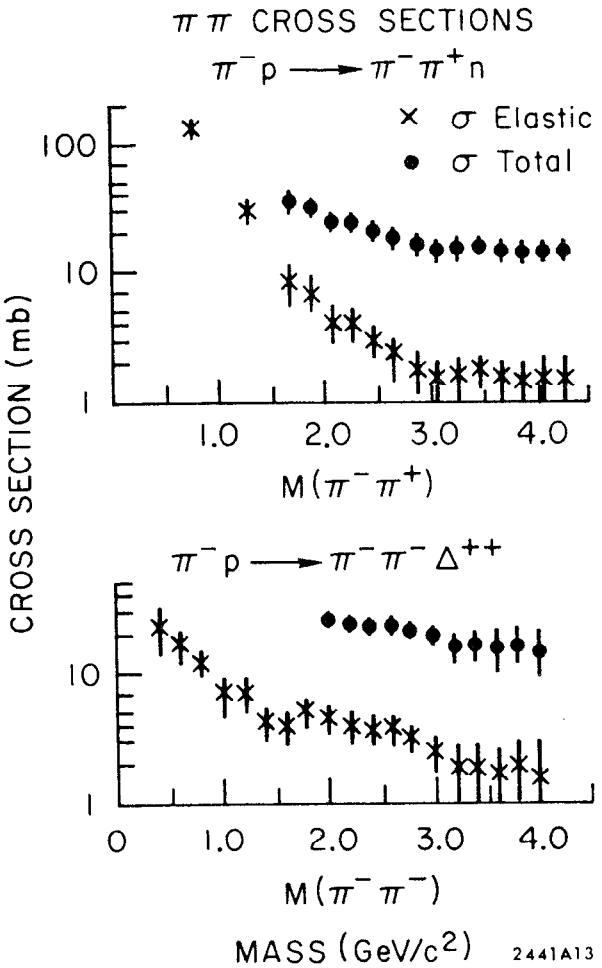
ππ CROSS SECTIONS
π⁻p → π⁻π⁺n
× σ Elastic
● σ Total
100
10
1
1.0
2.0
3.0
4.0
M(π⁻π⁺)
CROSS SECTION (mb)
π⁻p → π⁻π⁻Δ⁺⁺
10
1
0
1.0
2.0
3.0
4.0
M(π⁻π⁻)
MASS (GeV/c²)
2441A13

Fig. 13

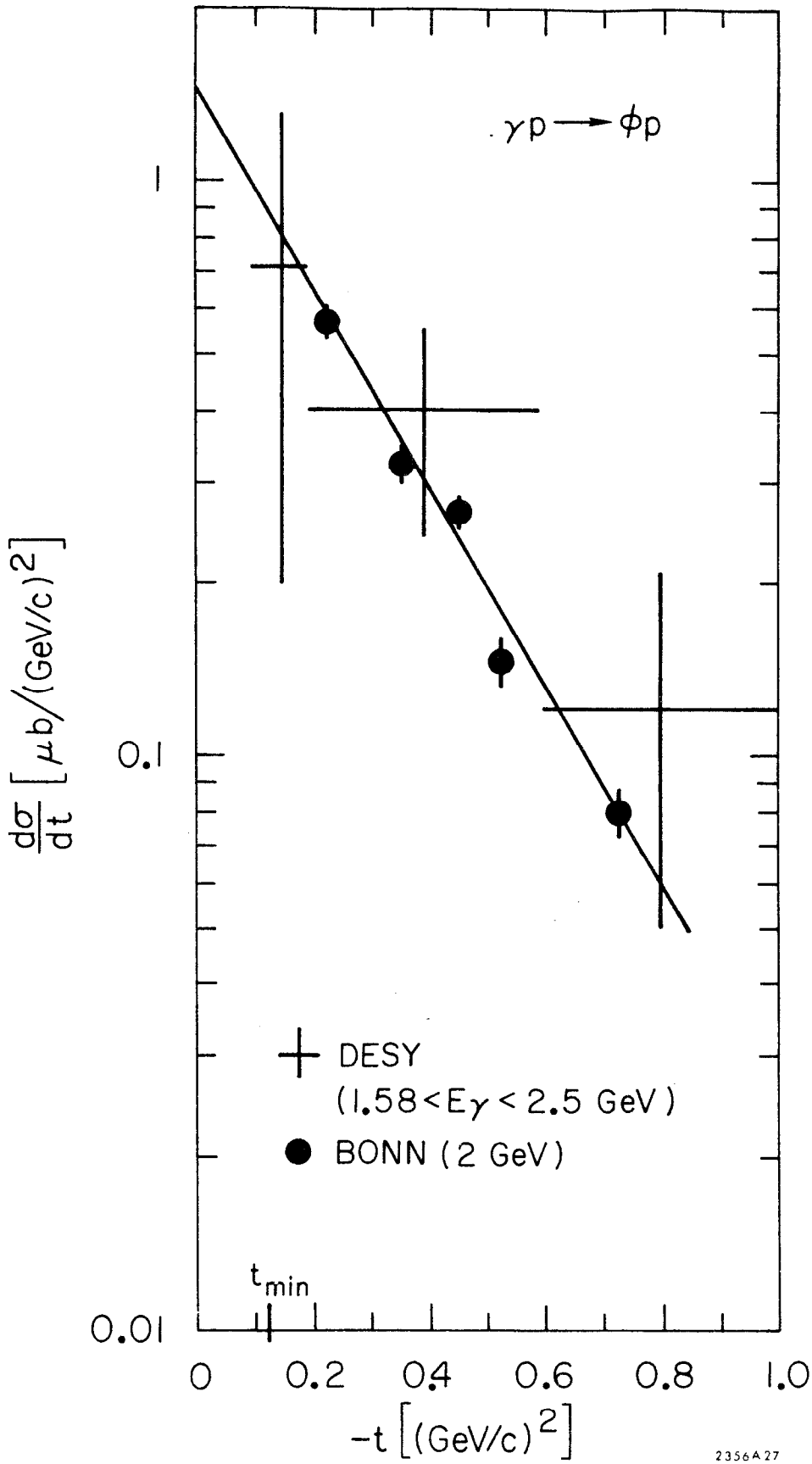
γp → φp
1
0.1
0.01
dσ/dt [μb/(GeV/c)²]
DESY
(1.58 < Eγ < 2.5 GeV)
BONN (2 GeV)
t_min
0
0.2
0.4
0.6
0.8
1.0
−t [(GeV/c)²]
2356A27

Fig. 14

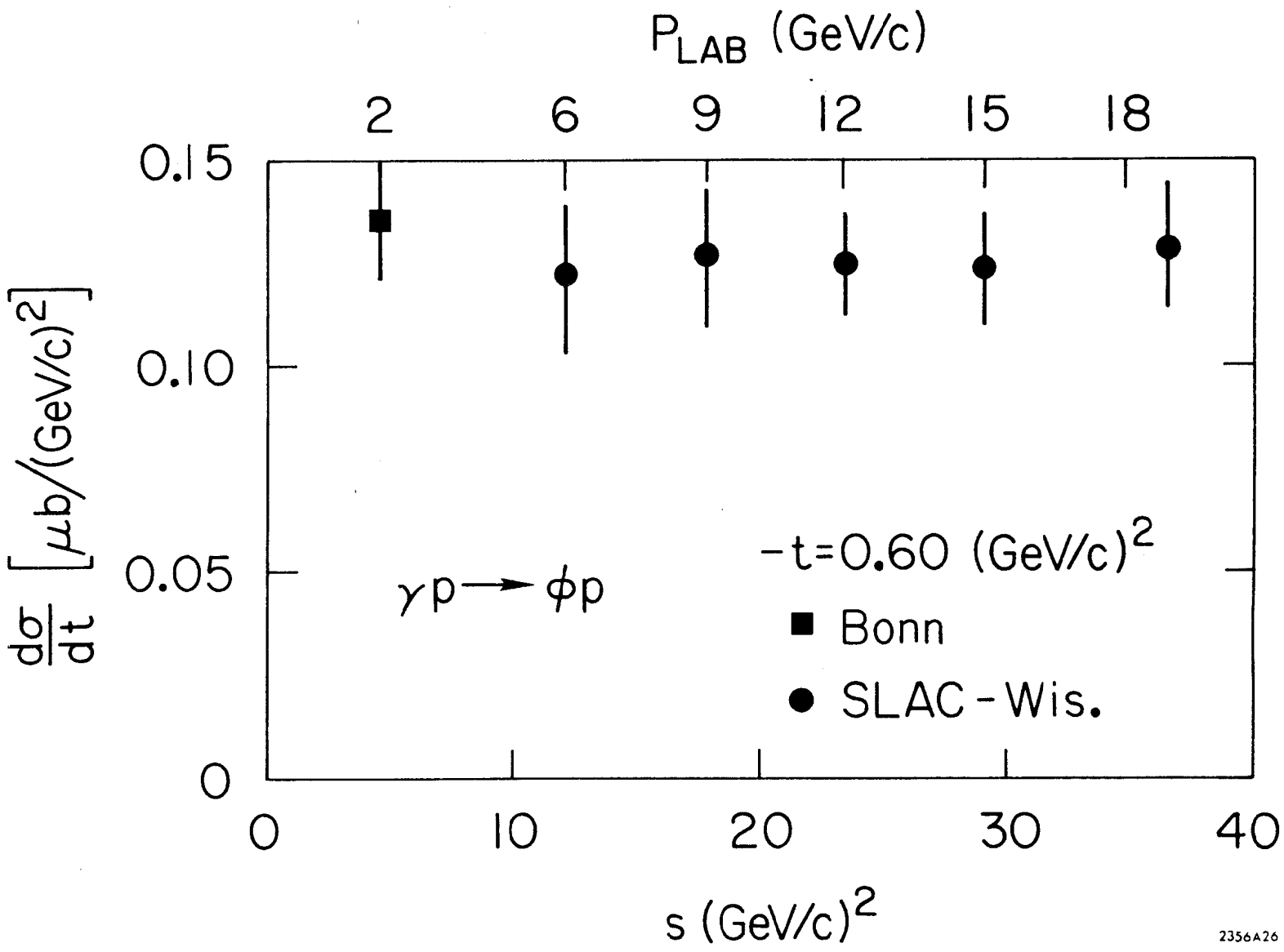
P_{LAB} (GeV/c)
2
6
9
12
15
18
0.15
0.10
0.05
0
$\frac{d\sigma}{dt}$ [μb/(GeV/c)^2]
$\gamma p \rightarrow \phi p$
$-t=0.60$ (GeV/c)^2
Bonn
SLAC-Wis.
0
10
20
30
40
s (GeV/c)^2
2356A26

Fig. 15

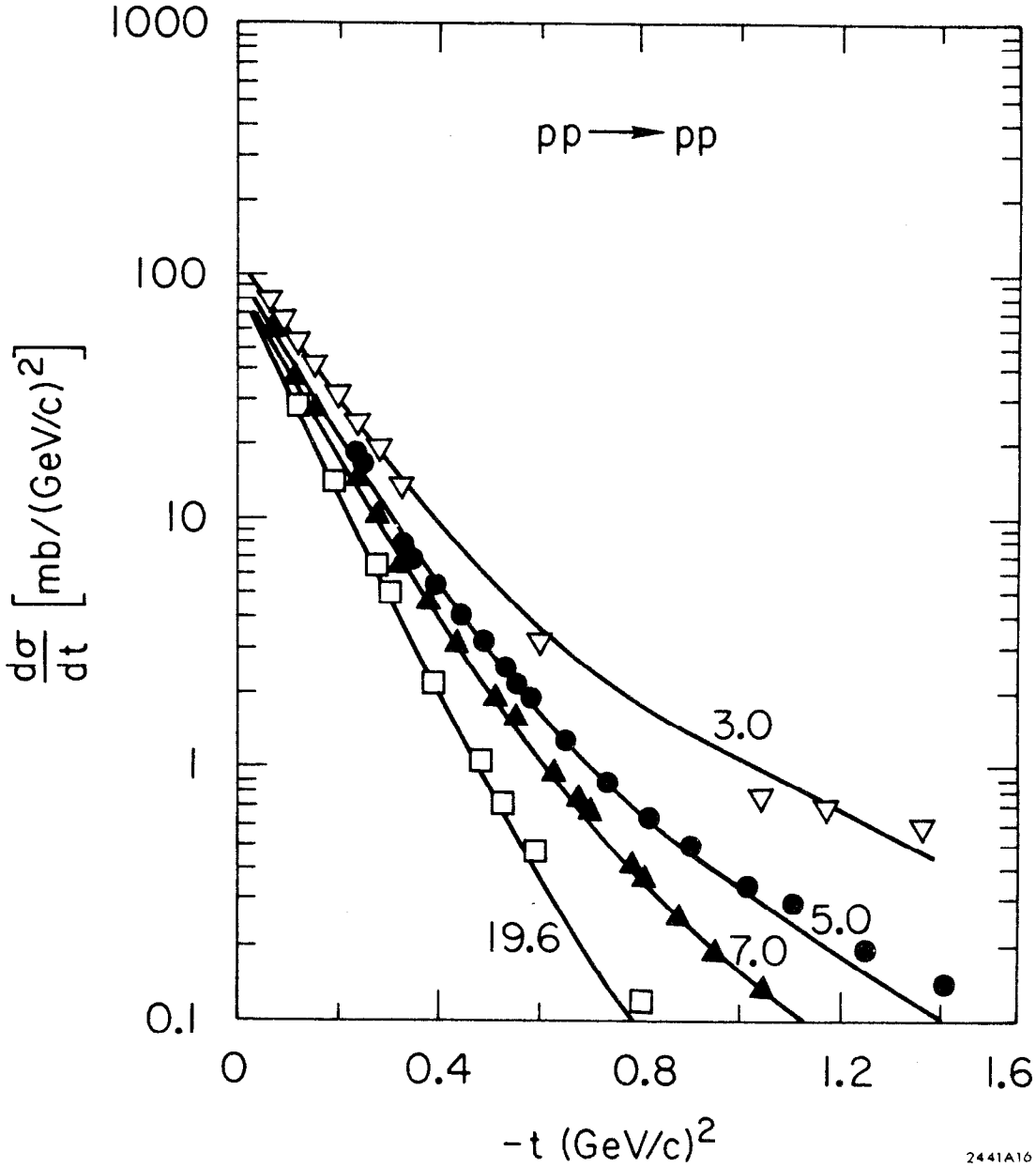
1000
100
10
1
0.1
pp → pp
3.0
5.0
7.0
19.6
0
0.4
0.8
1.2
1.6
$\frac{d\sigma}{dt}$ [mb/(GeV/c)^2]
$-t$ (GeV/c)^2
2441A16

Fig. 16

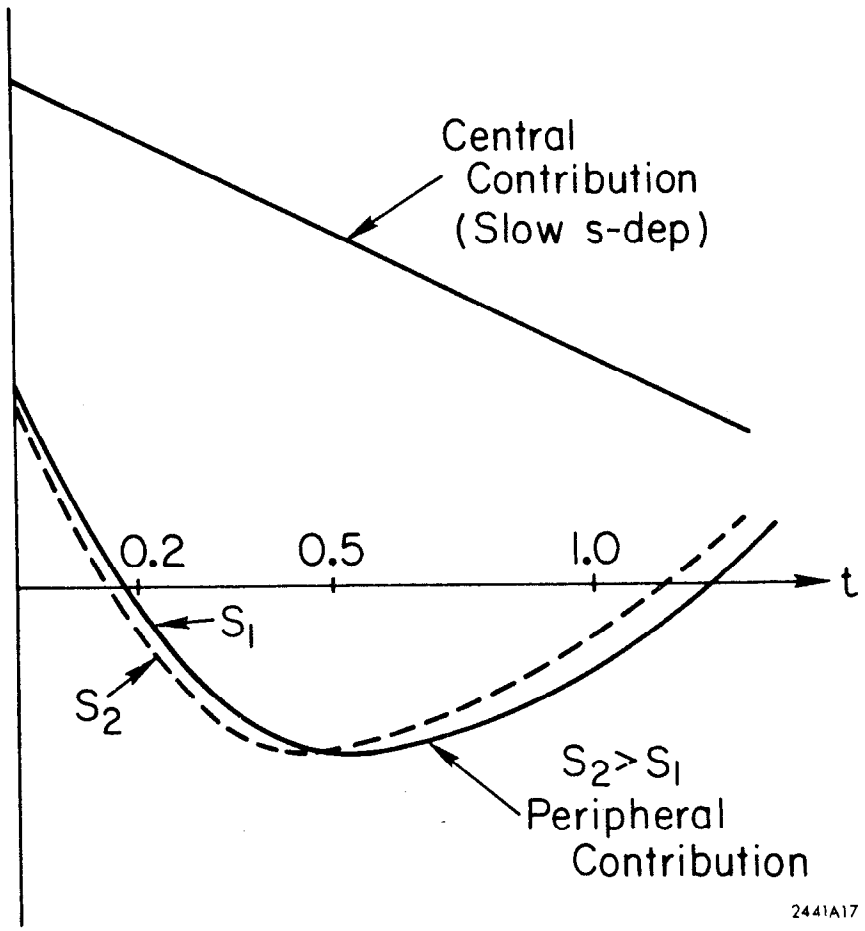
Central
Contribution
(Slow s-dep)
0.2
0.5
1.0
t
S_1
S_2
$S_2 > S_1$
Peripheral
Contribution
2441A17

Fig. 17

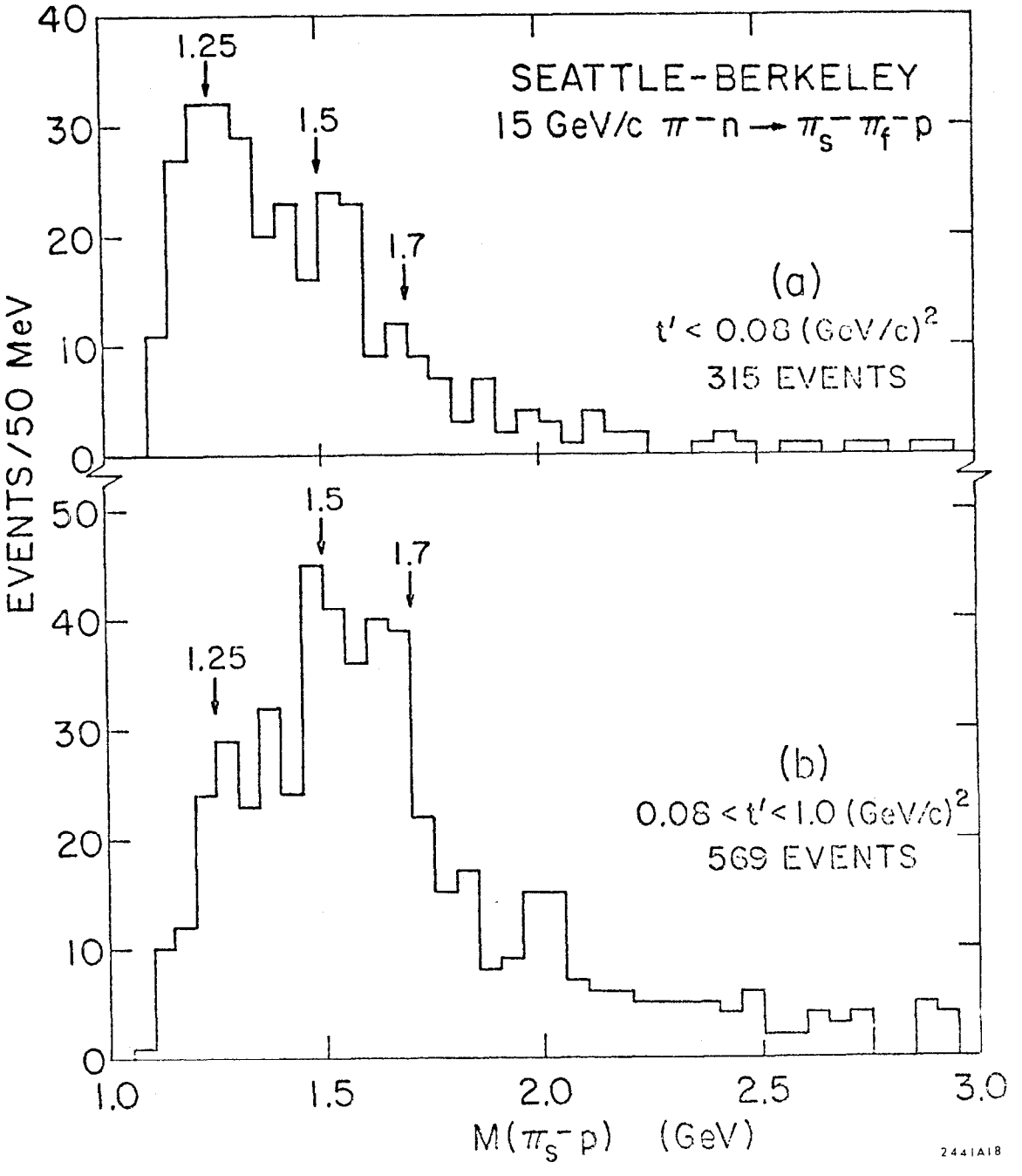
SEATTLE-BERKELEY
15 GeV/c $\pi^- n \rightarrow \pi_s^- \pi_f^- p$
(a)
$t' < 0.08\ (GeV/c)^2$
315 EVENTS
(b)
$0.08 < t' < 1.0\ (GeV/c)^2$
569 EVENTS
1.25
1.5
1.7
EVENTS/50 MeV
$M(\pi_s^- p)$ (GeV)
2441A18

Fig. 18

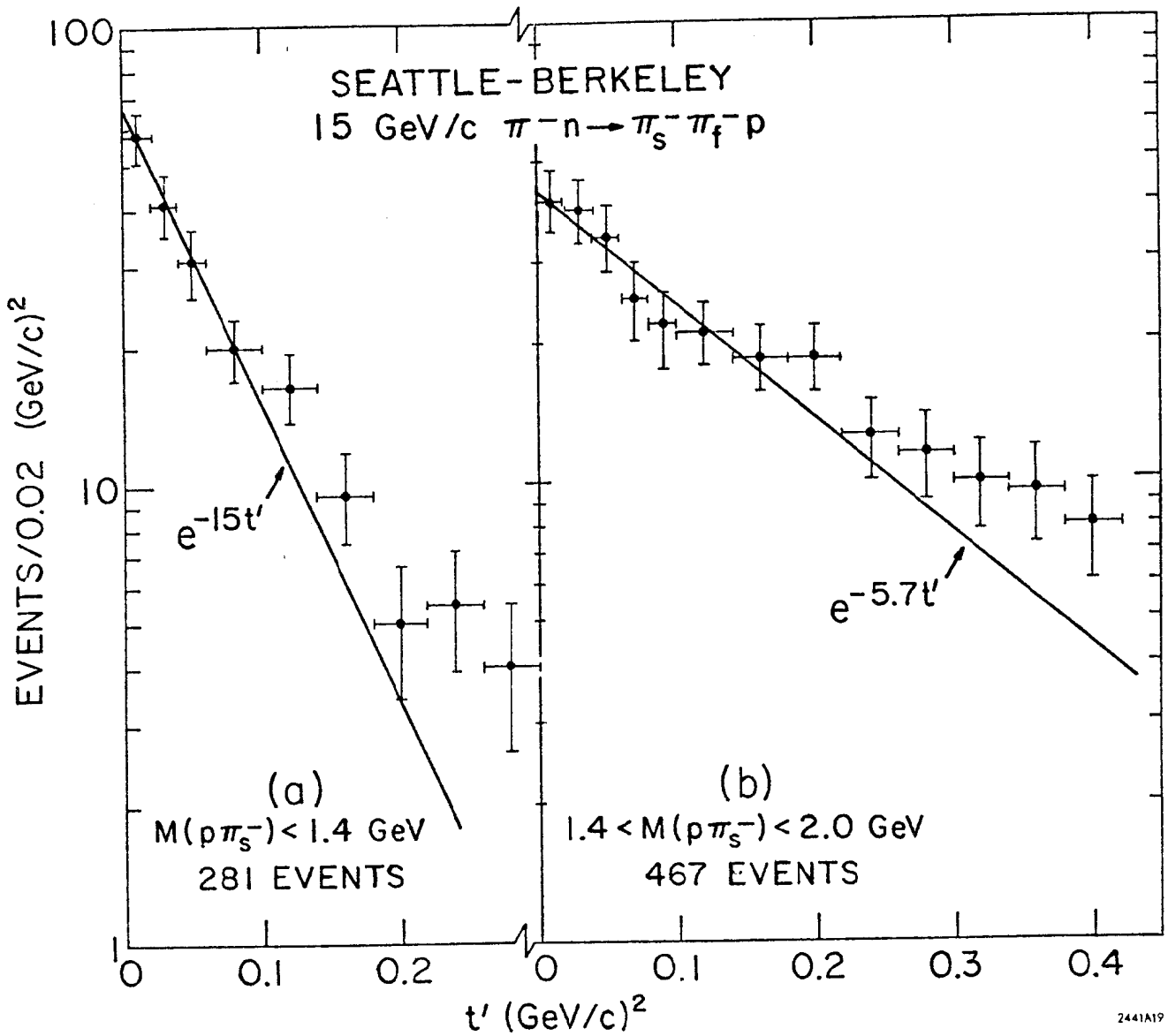
SEATTLE-BERKELEY
15 GeV/c $\pi^- n \rightarrow \pi_s^- \pi_f^- p$
EVENTS/0.02 (GeV/c)^2
100
10
1
$e^{-15t'}$
$e^{-5.7t'}$
(a)
$M(p\pi_s^-) < 1.4$ GeV
281 EVENTS
(b)
$1.4 < M(p\pi_s^-) < 2.0$ GeV
467 EVENTS
0
0.1
0.2
0.3
0.4
t' (GeV/c)^2
2441A19

Fig. 19

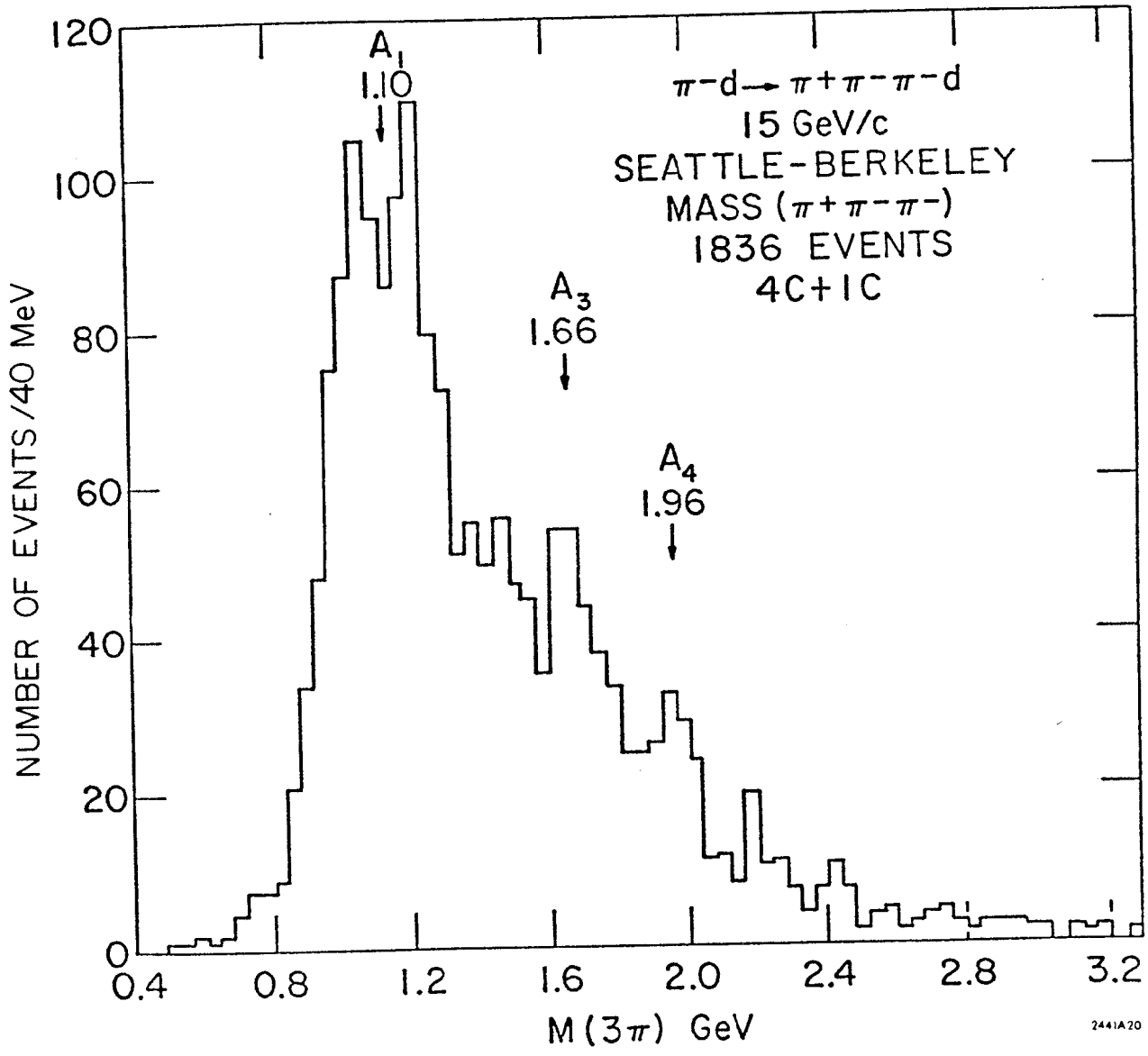
$\pi^- d \rightarrow \pi^+ \pi^- \pi^- d$
15 GeV/c
SEATTLE-BERKELEY
MASS ($\pi^+ \pi^- \pi^-$)
1836 EVENTS
4C+1C
A_1
1.10
A_3
1.66
A_4
1.96
NUMBER OF EVENTS/40 MeV
0
20
40
60
80
100
120
0.4
0.8
1.2
1.6
2.0
2.4
2.8
3.2
M (3π) GeV
2441A20

Fig. 20

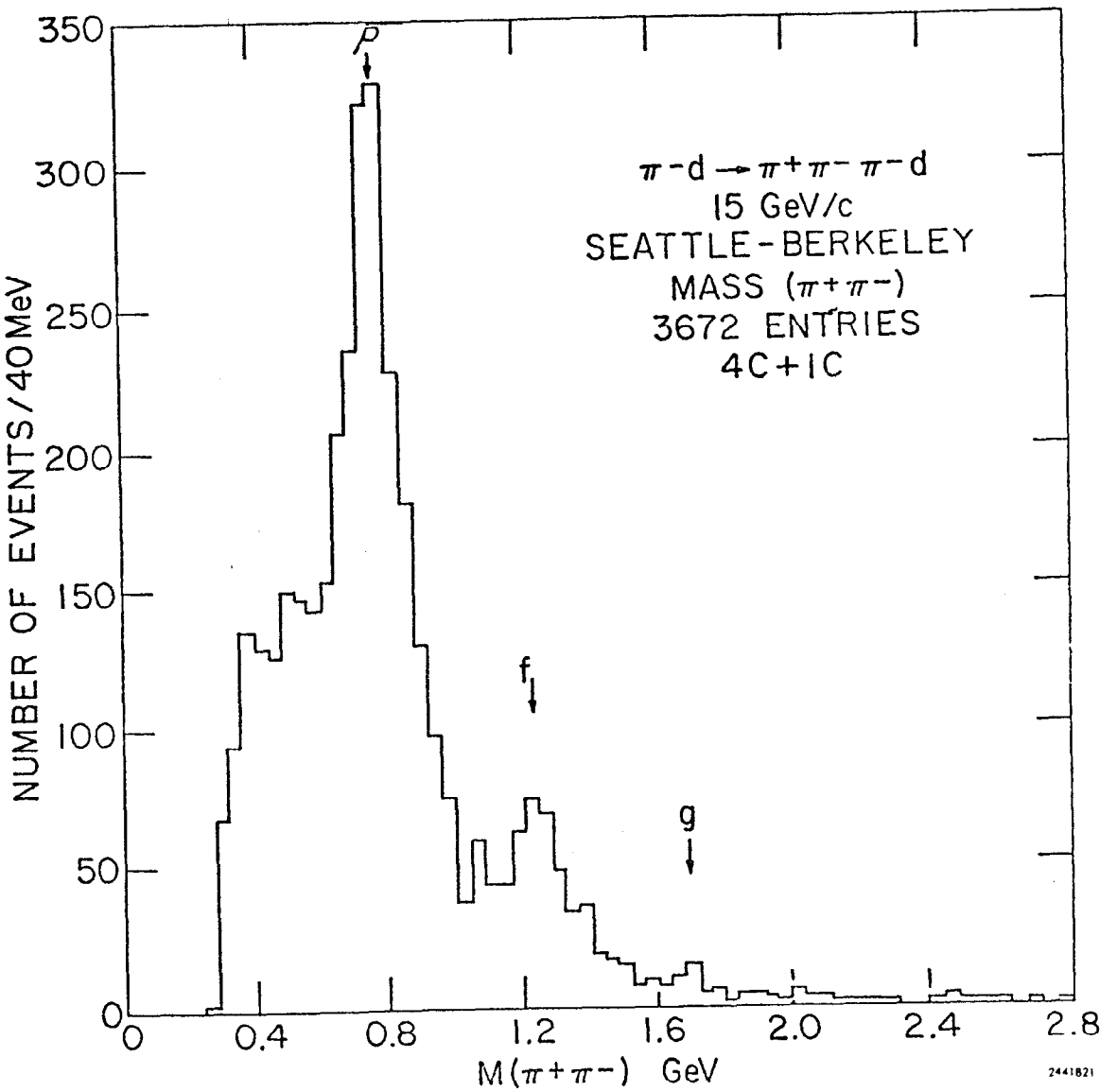
π-d → π+π- π-d
15 GeV/c
SEATTLE-BERKELEY
MASS (π+π-)
3672 ENTRIES
4C+1C
ρ
f
g
NUMBER OF EVENTS/40MeV
M(π+π-) GeV
0
50
100
150
200
250
300
350
0.4
0.8
1.2
1.6
2.0
2.4
2.8
2441B21

Fig. 21

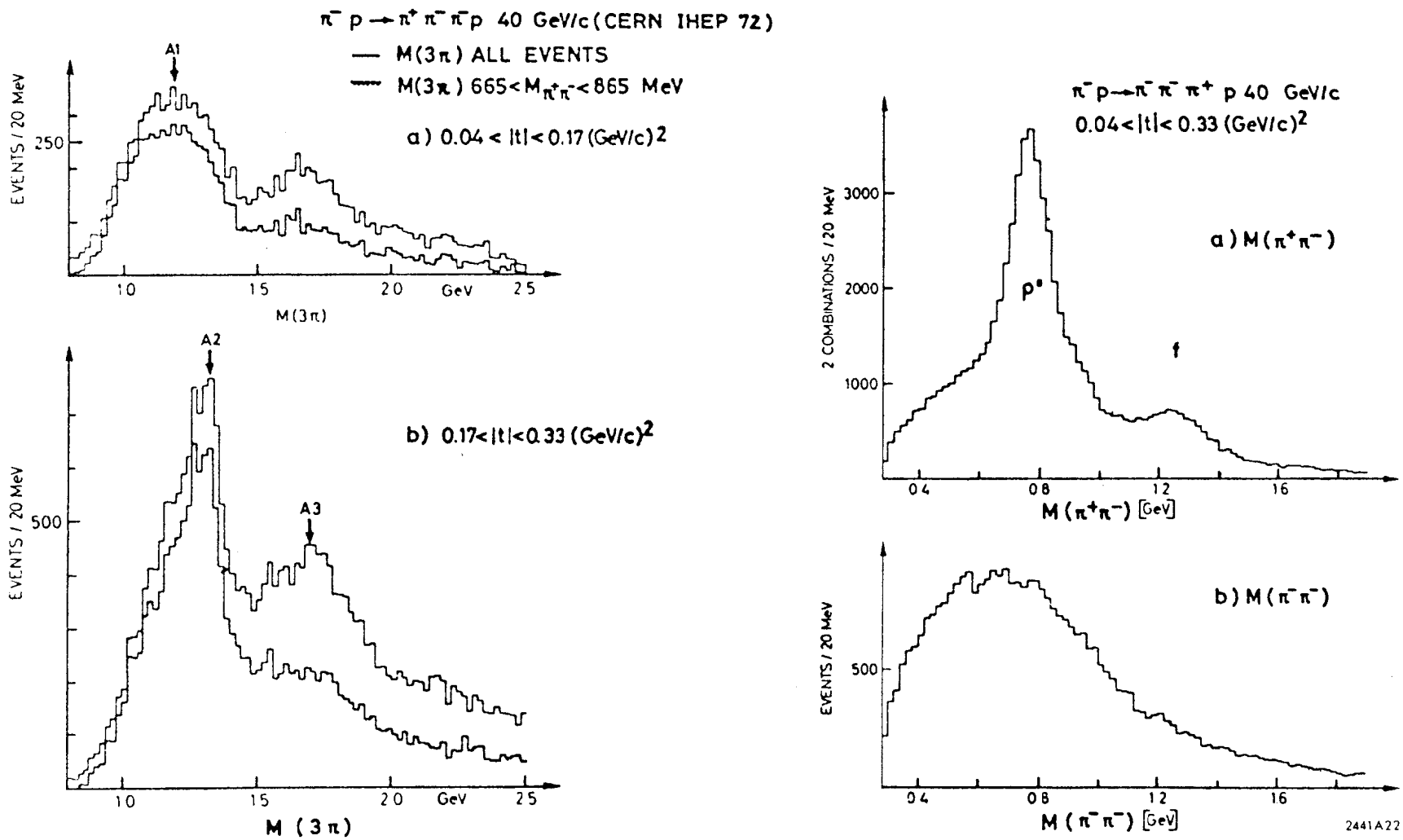
π⁻ p → π⁺ π⁻ π⁻ p 40 GeV/c (CERN IHEP 72)
— M(3π) ALL EVENTS
M(3π) 665 < M π⁺π⁻ < 865 MeV
a) 0.04 < |t| < 0.17 (GeV/c)²
A1
EVENTS / 20 MeV
250
10
15
20
GeV
25
M(3π)
b) 0.17 < |t| < 0.33 (GeV/c)²
A2
A3
500
M (3π)
π⁻ p → π⁻ π⁻ π⁺ p 40 GeV/c
0.04 < |t| < 0.33 (GeV/c)²
a) M(π⁺π⁻)
2 COMBINATIONS / 20 MeV
3000
2000
1000
ρ°
f
0.4
0.8
1.2
1.6
M (π⁺π⁻) [GeV]
b) M(π⁻π⁻)
M (π⁻π⁻) [GeV]
2441A22

Fig. 22

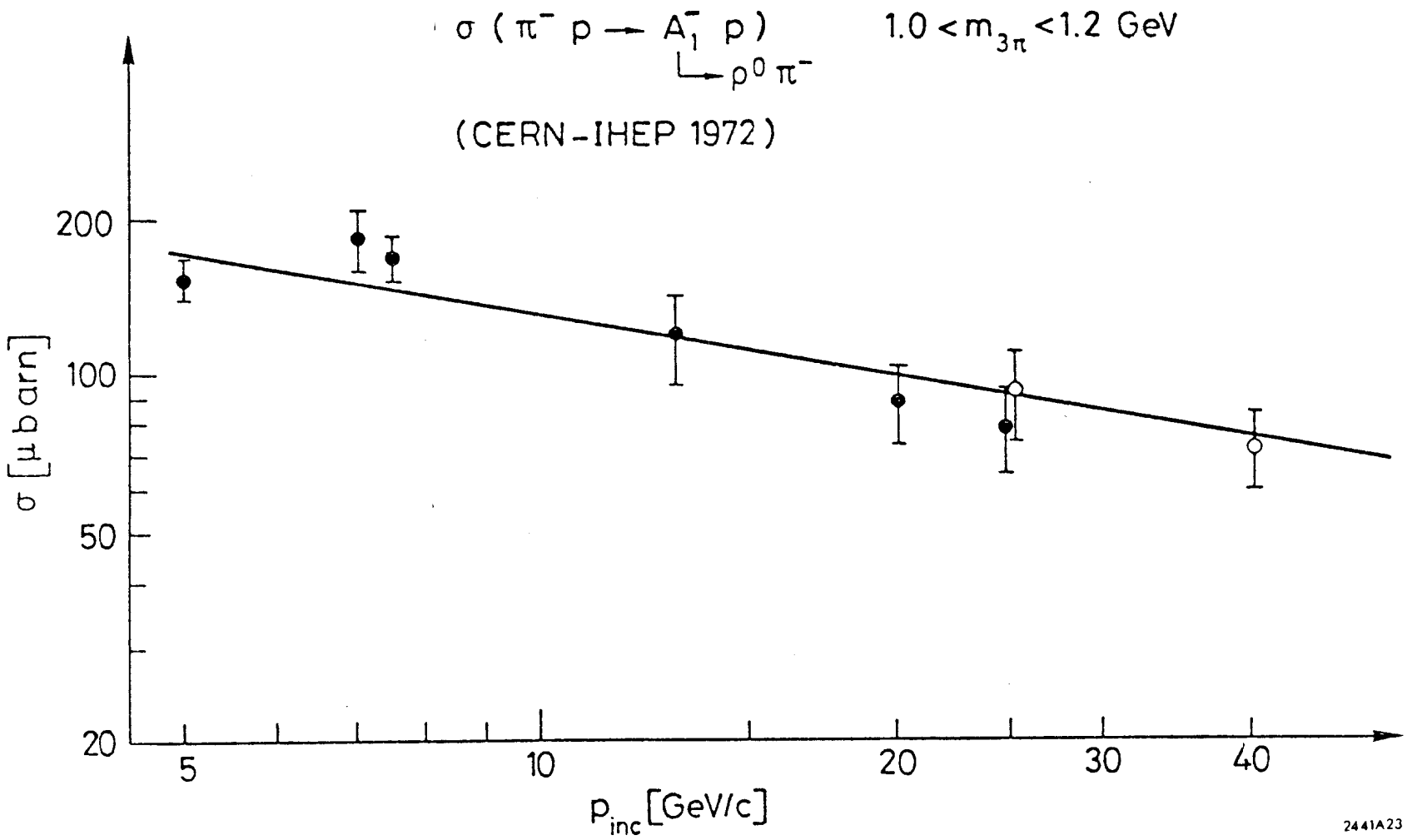
σ (π⁻ p → A₁⁻ p)
1.0 < m3π < 1.2 GeV
ρ⁰ π⁻
(CERN-IHEP 1972)
200
100
50
20
σ [μbarn]
5
10
20
30
40
p_inc [GeV/c]
2441A23

Fig. 23

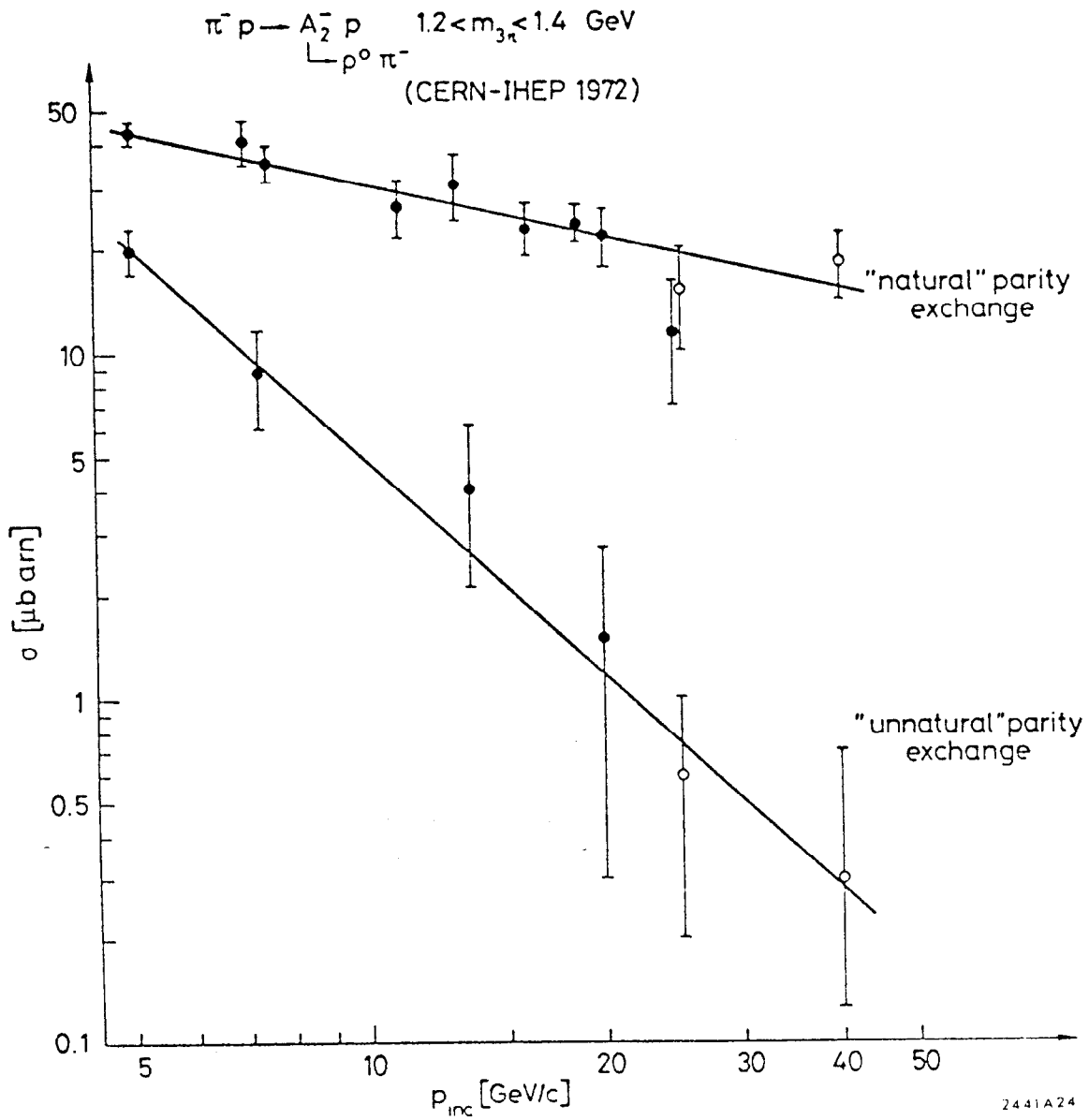
$\pi^- p \to A_2^- p$ 1.2 < $m_{3\pi}$ < 1.4 GeV
$\rho^0 \pi^-$
(CERN-IHEP 1972)
"natural" parity exchange
"unnatural" parity exchange
σ [μb arn]
p_{inc} [GeV/c]
50
10
5
1
0.5
0.1
5
10
20
30
40
50
2441A24

Fig. 24

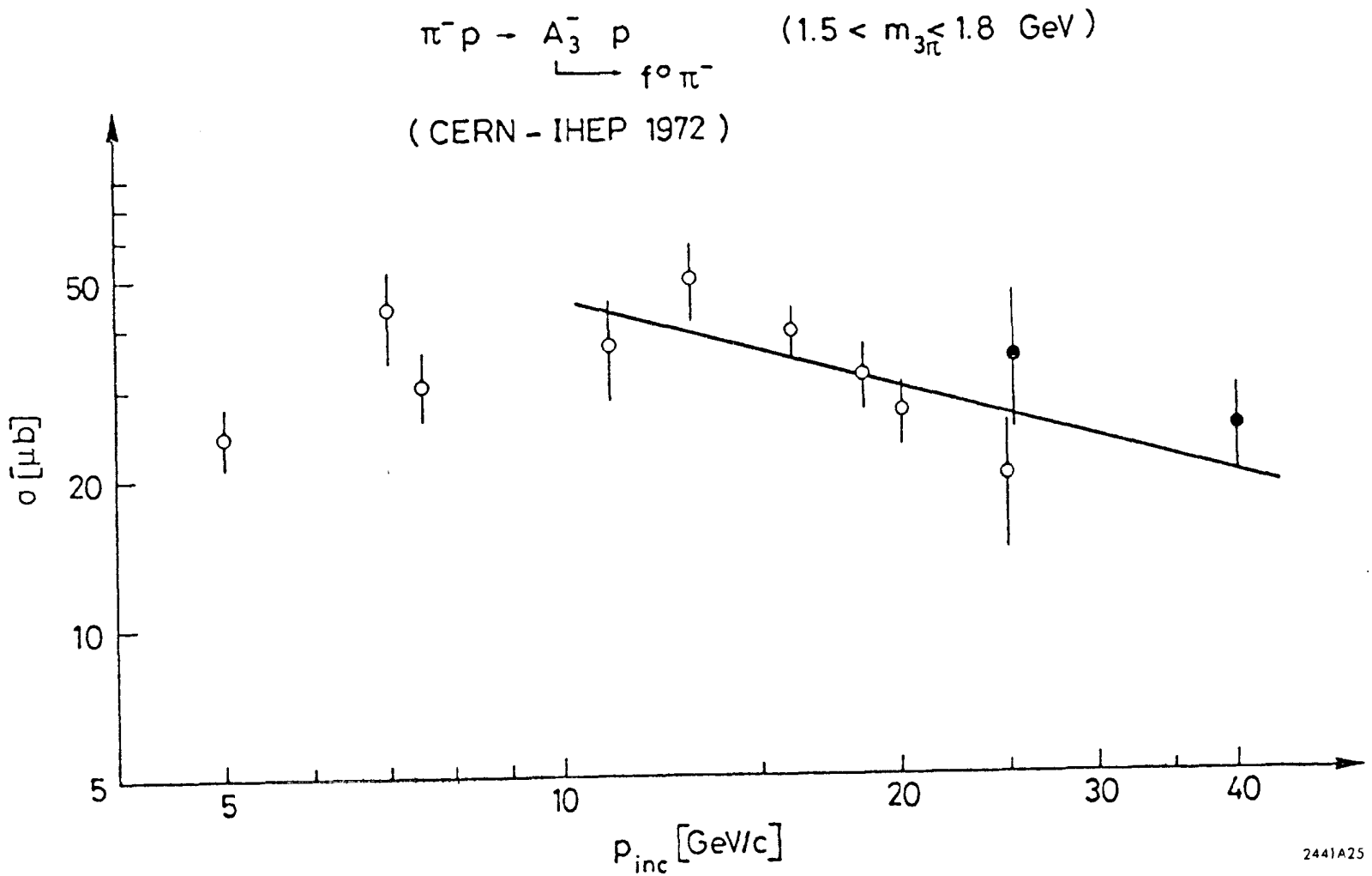
$\pi^- p \to A_3^- p$ $(1.5 < m_{3\pi} < 1.8$ GeV$)$
$\hookrightarrow f^0 \pi^-$
(CERN - IHEP 1972)
50
20
10
5
σ [μb]
5
10
20
30
40
p_{inc} [GeV/c]
2441A25

Fig. 25

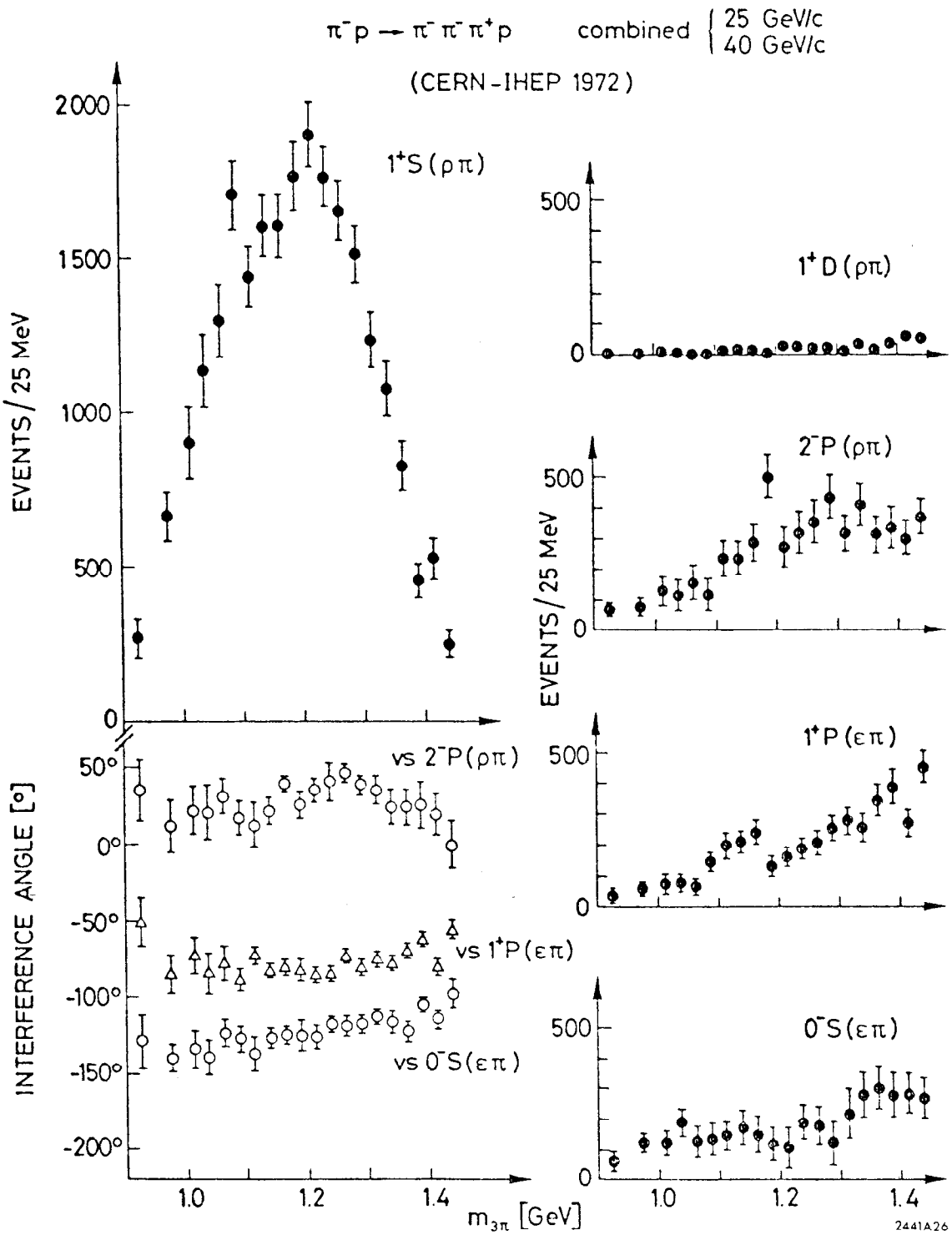
π⁻p → π⁻π⁻π⁺p
combined 25 GeV/c 40 GeV/c
(CERN-IHEP 1972)
1⁺S(ρπ)
1⁺D(ρπ)
2⁻P(ρπ)
1⁺P(επ)
0⁻S(επ)
vs 2⁻P(ρπ)
vs 1⁺P(επ)
vs 0⁻S(επ)
EVENTS/25 MeV
INTERFERENCE ANGLE [°]
m3π [GeV]
2441A26

Fig. 26

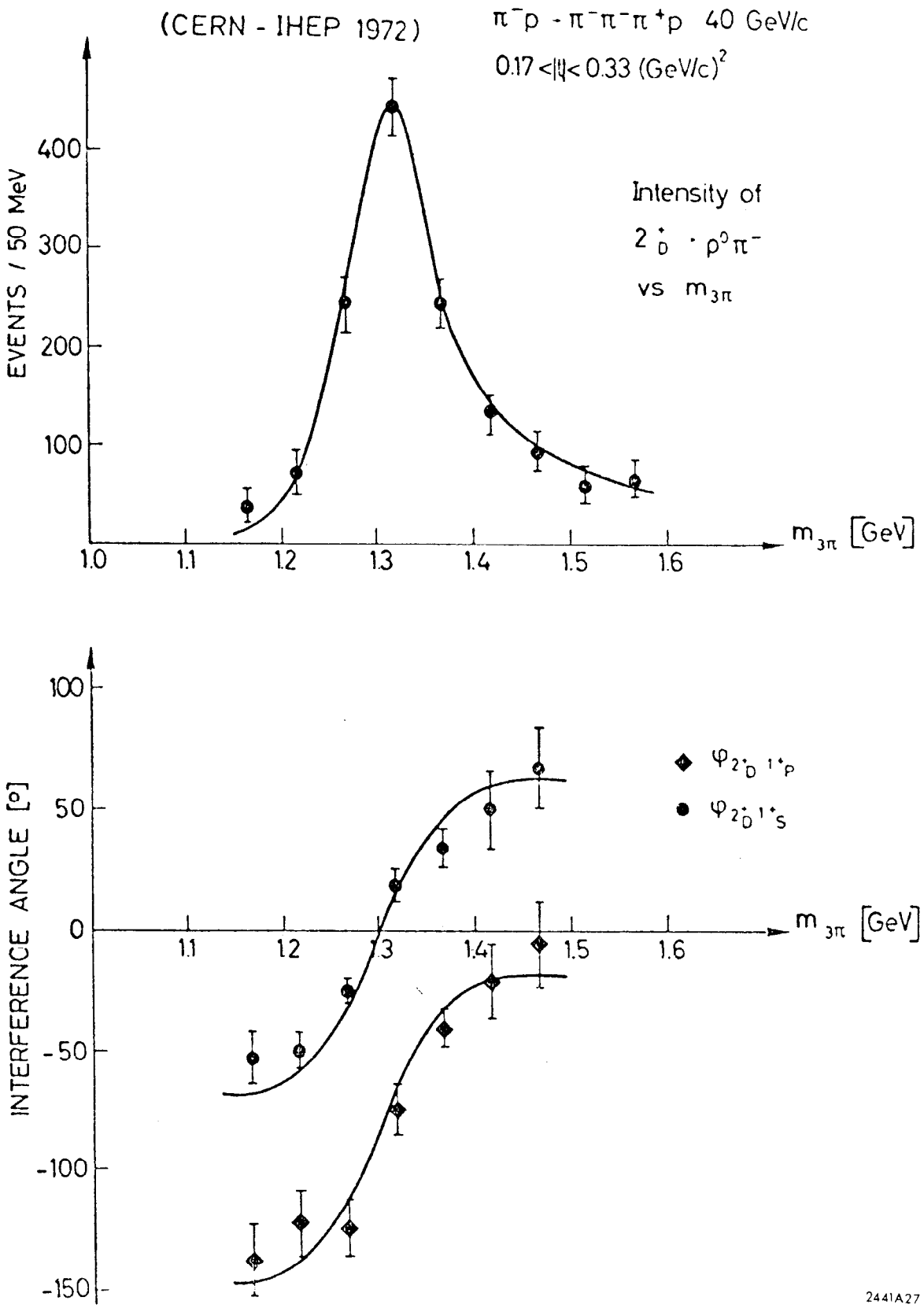
(CERN - IHEP 1972)
π⁻p → π⁻π⁻π⁺p 40 GeV/c
0.17 < |t| < 0.33 (GeV/c)²
Intensity of
2⁺D → ρ⁰π⁻
vs m3π
EVENTS / 50 MeV
400
300
200
100
1.0
1.1
1.2
1.3
1.4
1.5
1.6
m3π [GeV]
INTERFERENCE ANGLE [°]
100
50
0
-50
-100
-150
φ2⁺D 1⁺P
φ2⁺D 1⁺S
2441A27

Fig. 27

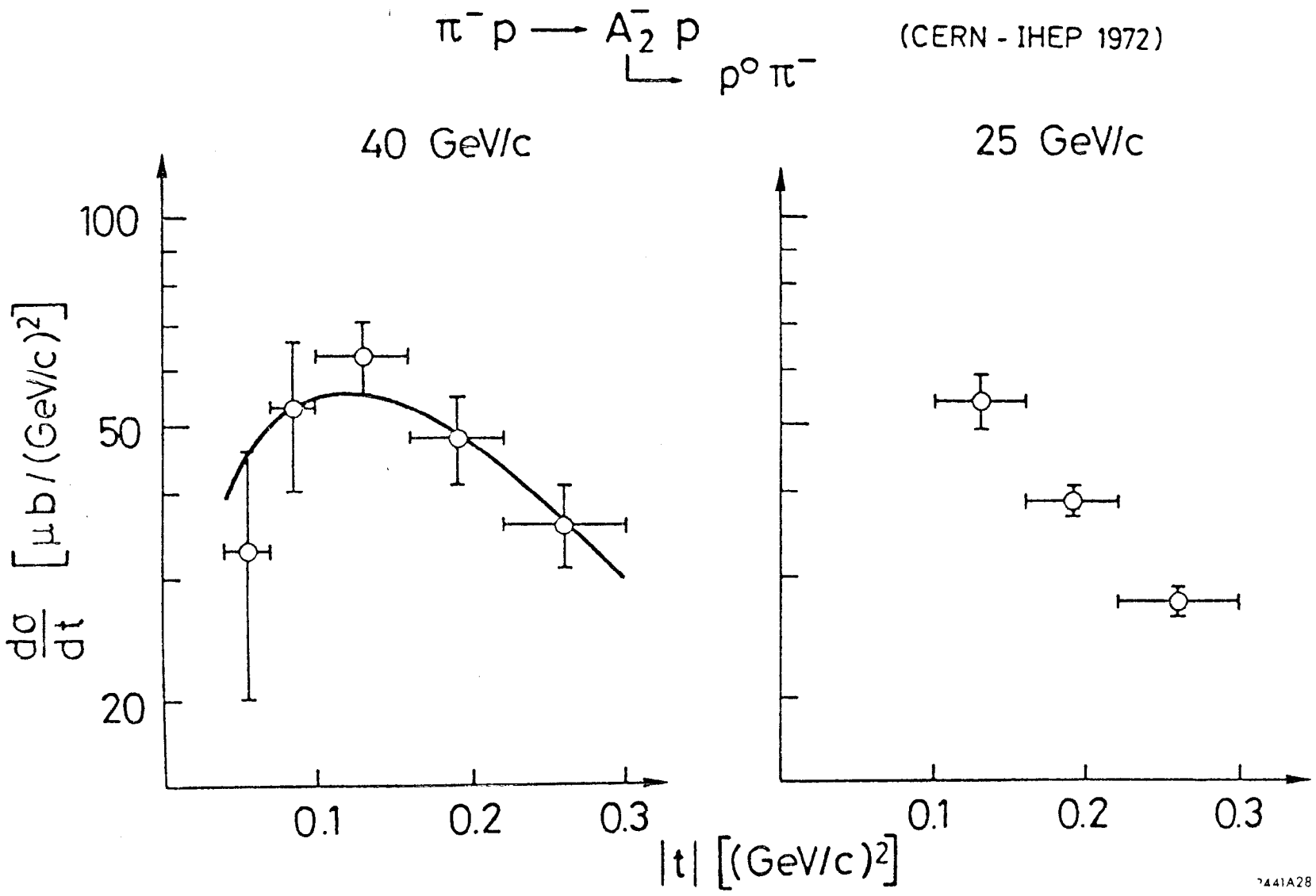
π⁻ p → A₂⁻ p
ρ° π⁻
(CERN - IHEP 1972)
40 GeV/c
25 GeV/c
100
50
20
dσ/dt [μb/(GeV/c)²]
0.1
0.2
0.3
|t| [(GeV/c)²]
2441A28

Fig. 28

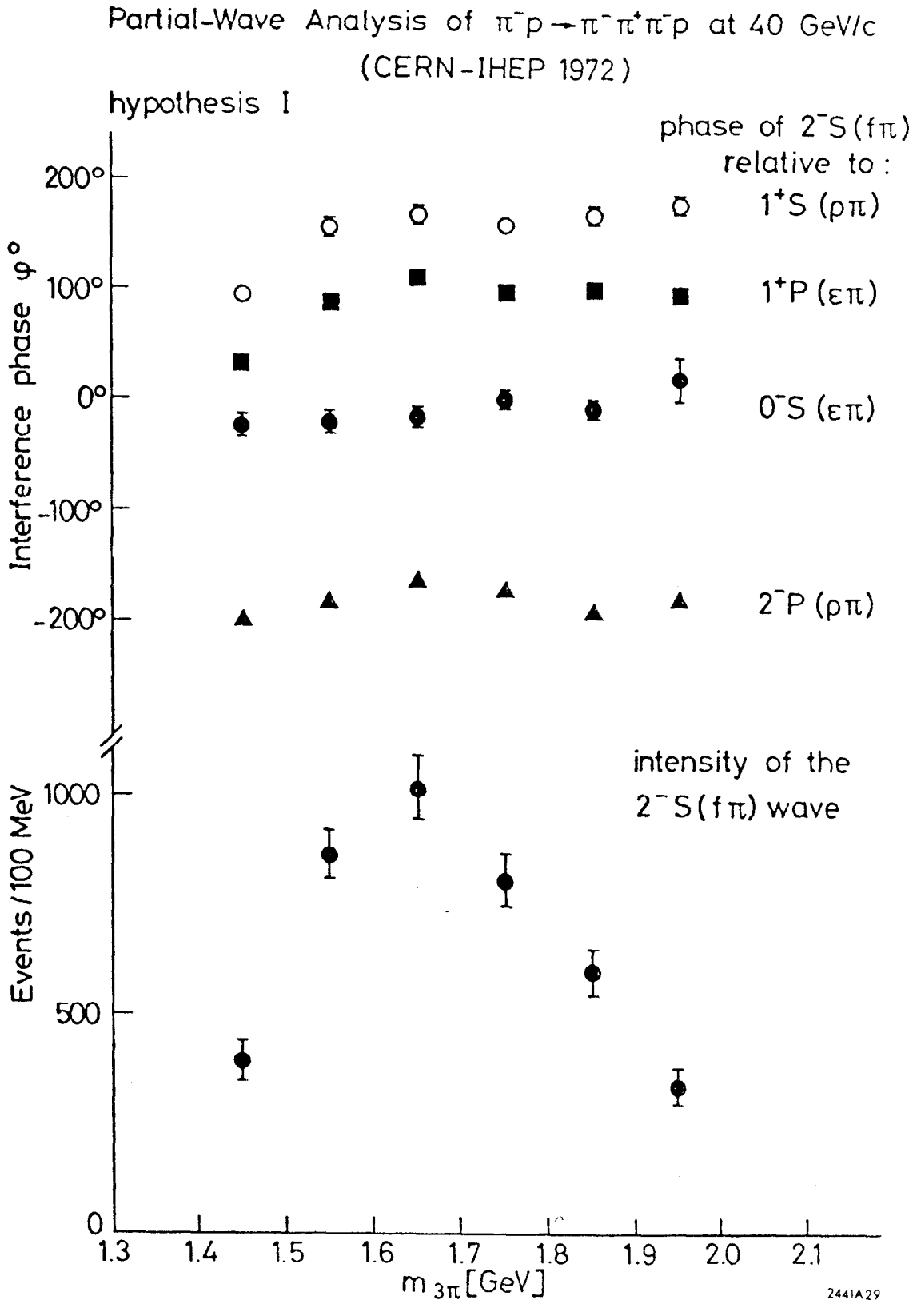
Partial-Wave Analysis of $\pi^- p \to \pi^- \pi^+ \pi^- p$ at 40 GeV/c
(CERN-IHEP 1972)
hypothesis I
phase of $2^-S(f\pi)$ relative to:
$1^+S(\rho\pi)$
$1^+P(\varepsilon\pi)$
$0^-S(\varepsilon\pi)$
$2^-P(\rho\pi)$
Interference phase $\varphi°$
200°
100°
0°
-100°
-200°
intensity of the $2^-S(f\pi)$ wave
Events / 100 MeV
1000
500
0
1.3
1.4
1.5
1.6
1.7
1.8
1.9
2.0
2.1
$m_{3\pi}$ [GeV]
2441A29

Fig. 29

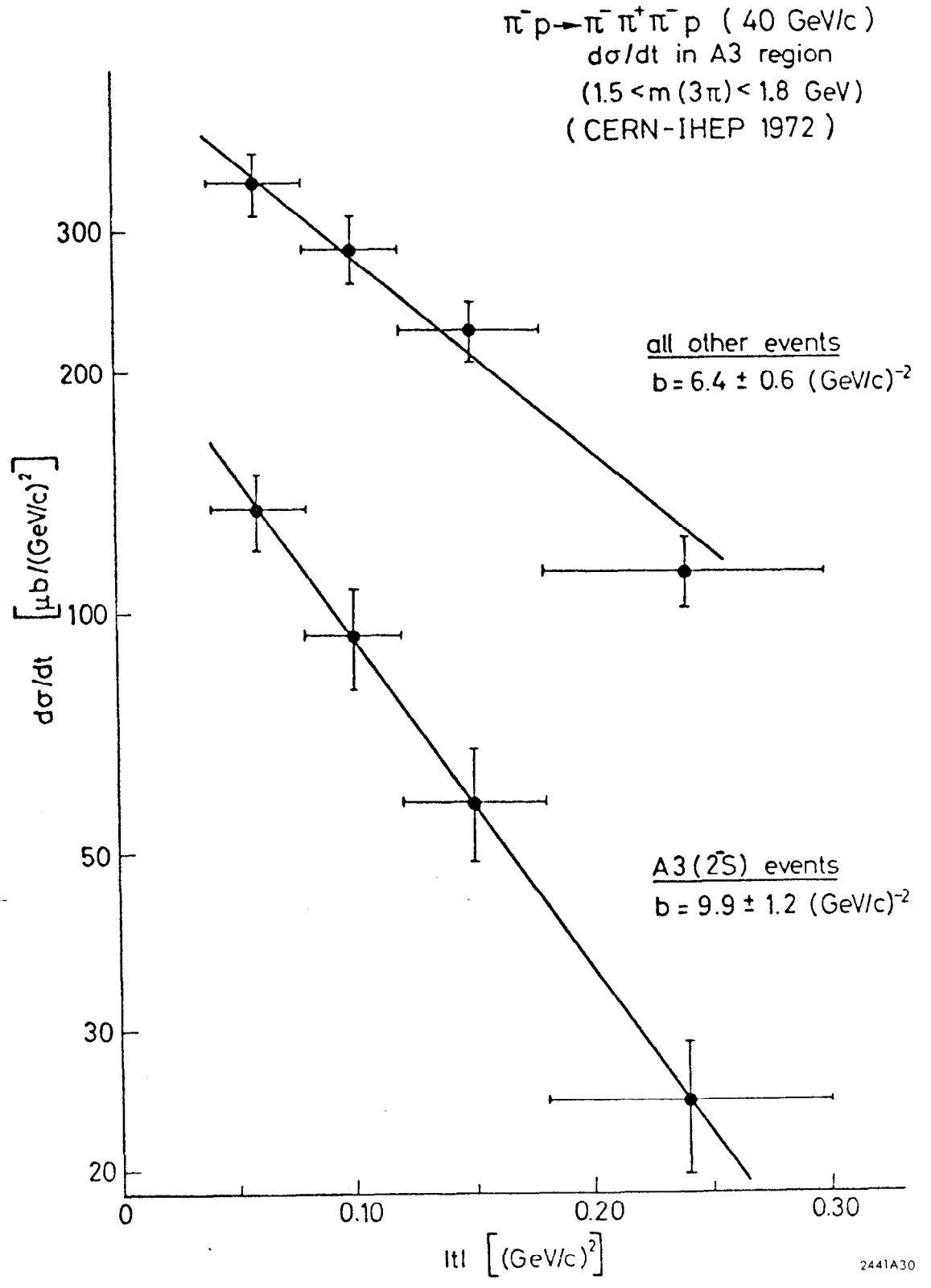
π⁻p→π⁻π⁺π⁻p (40 GeV/c)
dσ/dt in A3 region
(1.5 < m(3π) < 1.8 GeV)
(CERN-IHEP 1972)
all other events
b = 6.4 ± 0.6 (GeV/c)⁻²
A3(2⁻S) events
b = 9.9 ± 1.2 (GeV/c)⁻²
dσ/dt [μb/(GeV/c)²]
300
200
100
50
30
20
0
0.10
0.20
0.30
|t| [(GeV/c)²]
2441A30

Fig. 30

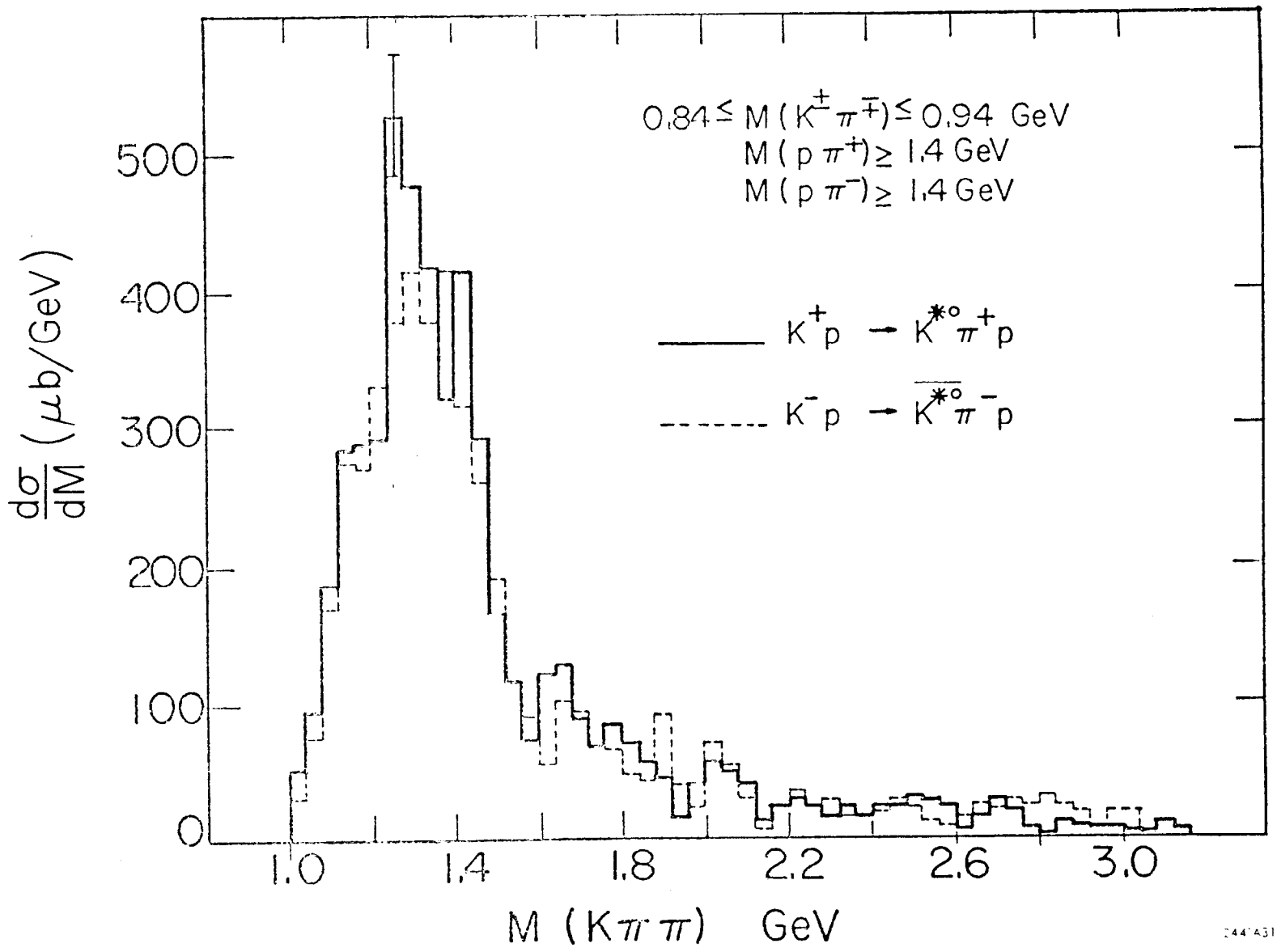
0.84 ≤ M (K± π∓) ≤ 0.94 GeV
M (p π+) ≥ 1.4 GeV
M (p π−) ≥ 1.4 GeV
K+ p → K*° π+ p
K− p → K̄*° π− p
dσ/dM (μb/GeV)
500
400
300
200
100
0
1.0
1.4
1.8
2.2
2.6
3.0
M (Kπ π) GeV

Fig. 31

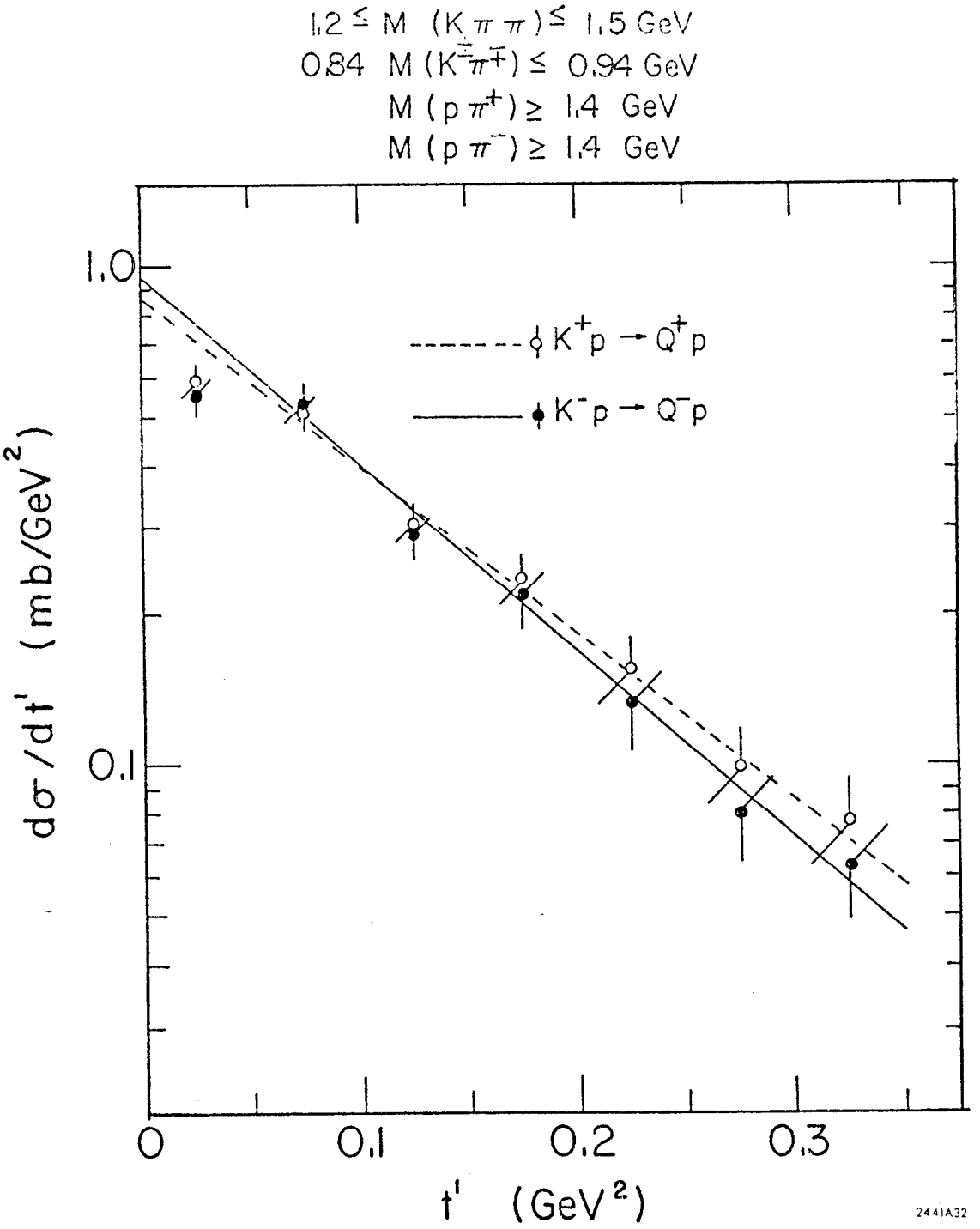
1.2 ≤ M (K π π) ≤ 1.5 GeV
0.84 M (K∓π∓) ≤ 0.94 GeV
M (p π+) ≥ 1.4 GeV
M (p π−) ≥ 1.4 GeV
K+p → Q+p
K−p → Q−p
dσ/dt' (mb/GeV²)
1.0
0.1
0
0.1
0.2
0.3
t' (GeV²)
2441A32

Fig. 32

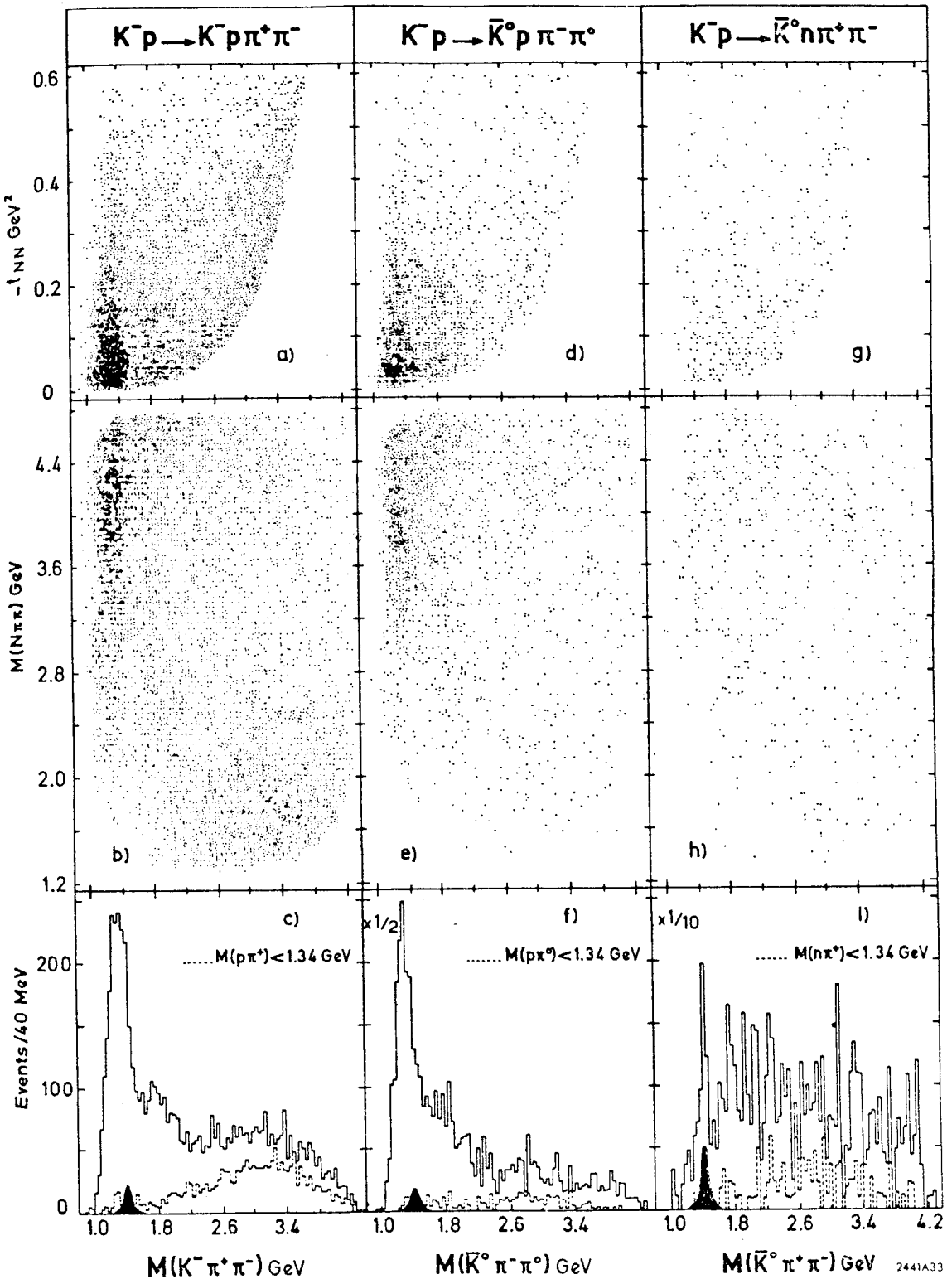
K⁻p → K⁻pπ⁺π⁻
K⁻p → K̄°pπ⁻π°
K⁻p → K̄°nπ⁺π⁻
-t NN GeV²
M(Nππ) GeV
Events/40 MeV
a)
b)
c)
d)
e)
f)
g)
h)
i)
x1/2
x1/10
.....M(pπ⁺)<1.34 GeV
.....M(pπ°)<1.34 GeV
.....M(nπ⁺)<1.34 GeV
M(K⁻π⁺π⁻) GeV
M(K̄°π⁻π°) GeV
M(K̄°π⁺π⁻) GeV
2441A33

Fig. 33

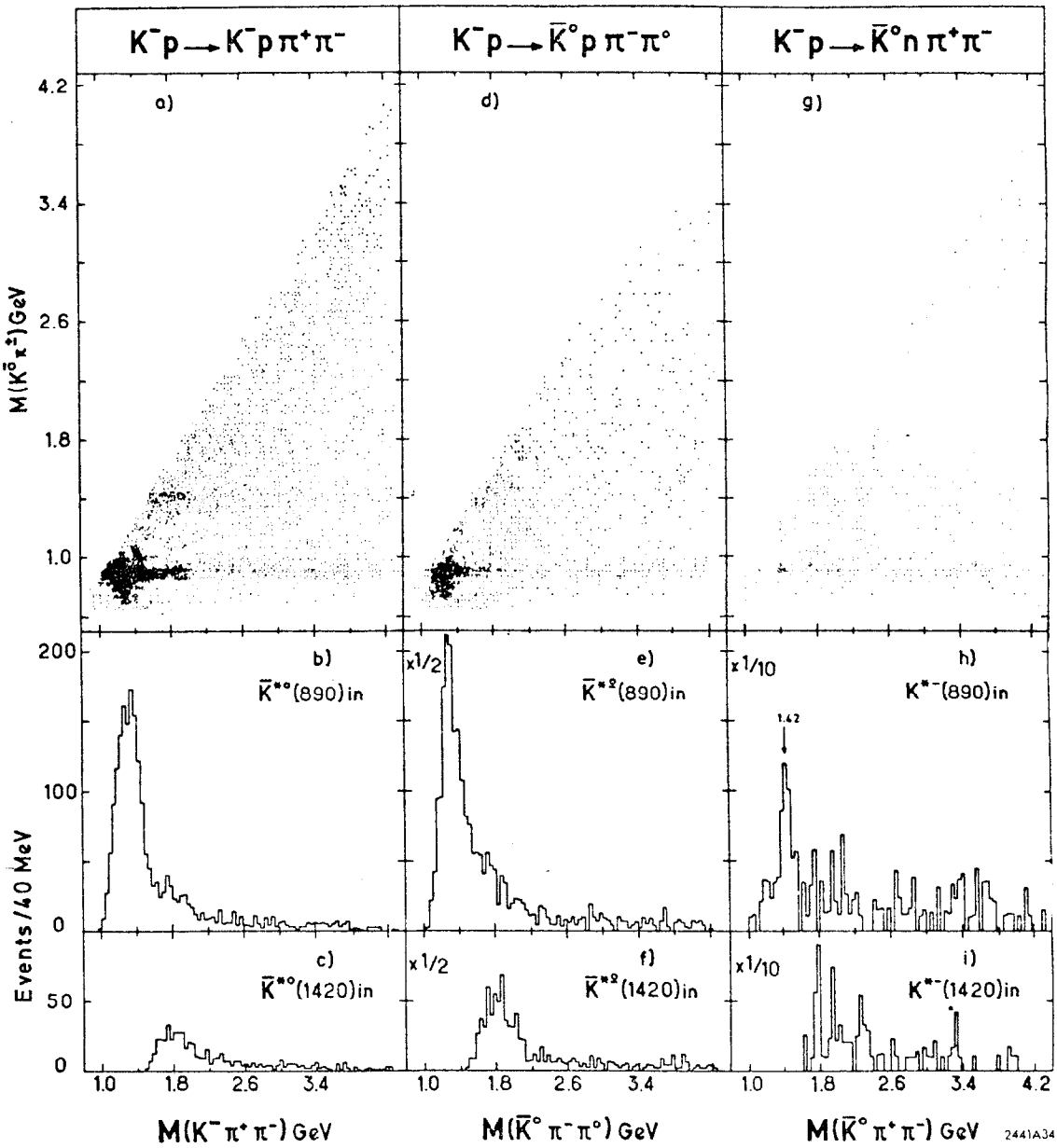
K⁻p → K⁻p π⁺π⁻
K⁻p → K̄°p π⁻π°
K⁻p → K̄°n π⁺π⁻
a)
d)
g)
M(K̄°π±) GeV
4.2
3.4
2.6
1.8
1.0
b)
K̄*°(890)in
e)
K̄*°(890)in
x1/2
h)
K*⁻(890)in
x1/10
1.42
c)
K̄*°(1420)in
f)
K̄*°(1420)in
x1/2
i)
K*⁻(1420)in
x1/10
Events/40 MeV
200
100
0
50
0
1.0
1.8
2.6
3.4
4.2
M(K⁻π⁺π⁻) GeV
M(K̄°π⁻π°) GeV
M(K̄°π⁺π⁻) GeV
2441A34

Fig. 34

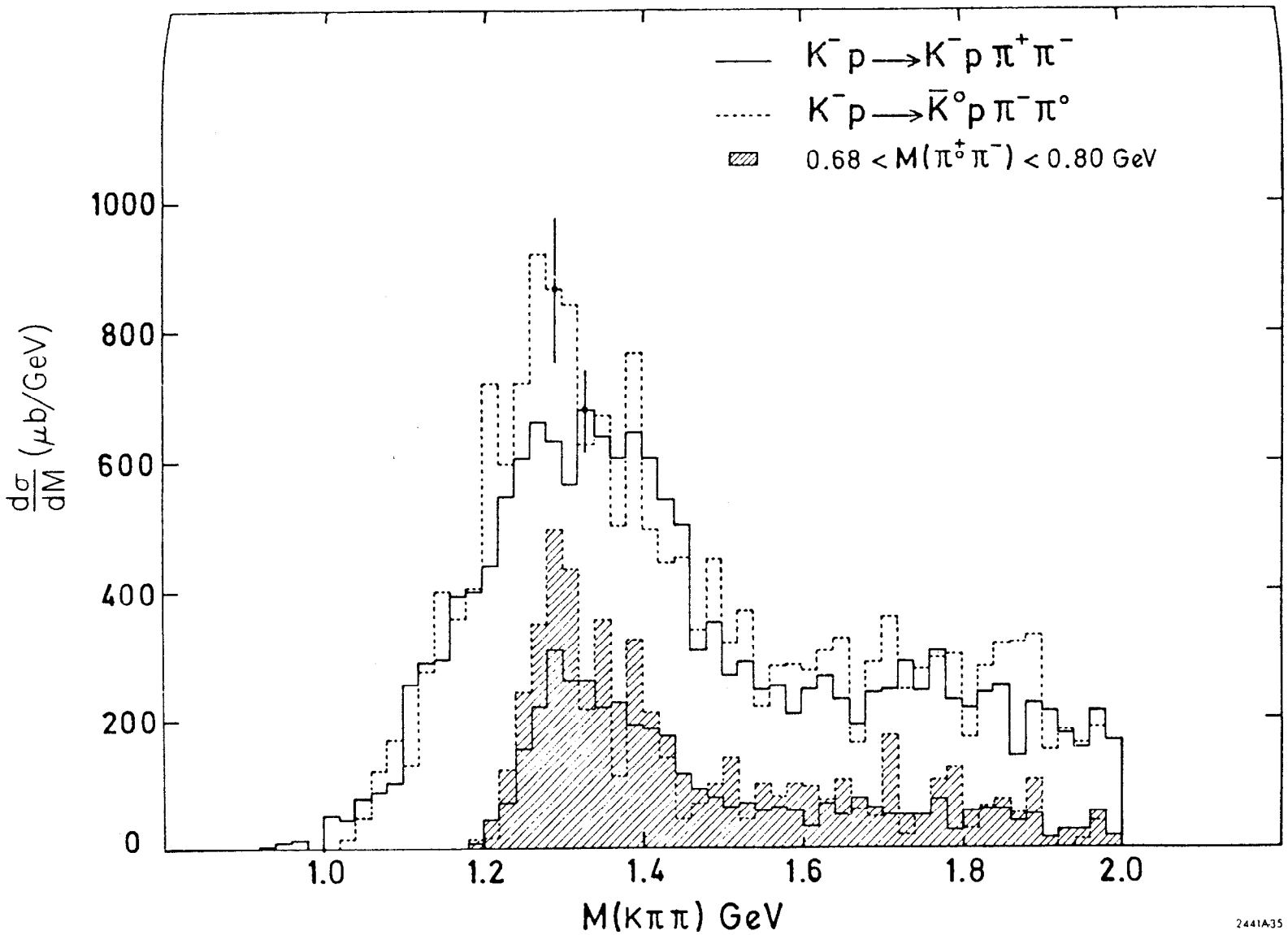
$K^- p \longrightarrow K^- p \pi^+ \pi^-$
$K^- p \longrightarrow \bar{K}^0 p \pi^- \pi^0$
$0.68 < M(\pi^{\pm 0} \pi^-) < 0.80$ GeV
$\frac{d\sigma}{dM}$ (μb/GeV)
1000
800
600
400
200
0
1.0
1.2
1.4
1.6
1.8
2.0
$M(K\pi\pi)$ GeV
2441A-35

Fig. 35

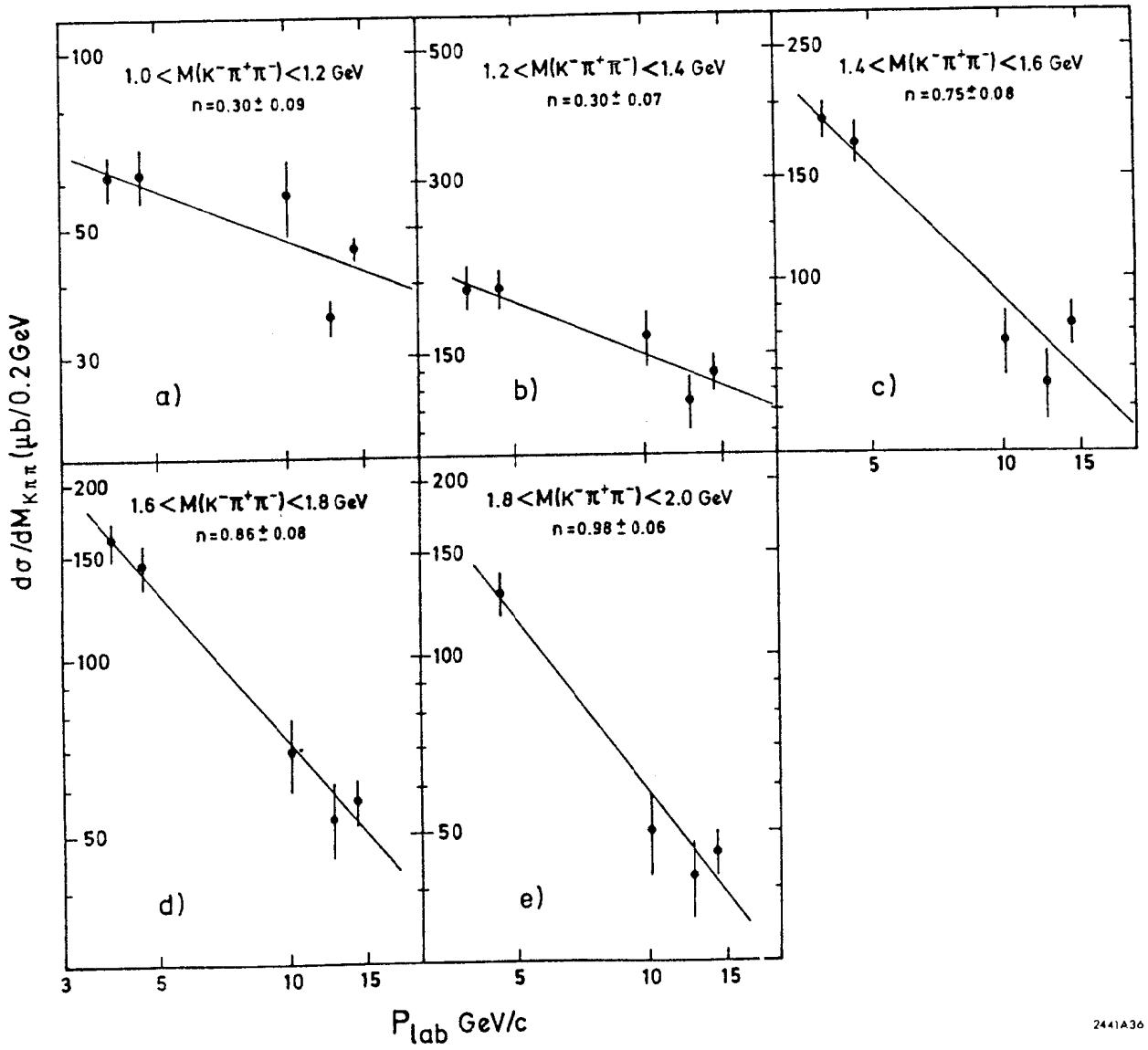
1.0 < M(K⁻π⁺π⁻) < 1.2 GeV
n = 0.30 ± 0.09
a)
1.2 < M(K⁻π⁺π⁻) < 1.4 GeV
n = 0.30 ± 0.07
b)
1.4 < M(K⁻π⁺π⁻) < 1.6 GeV
n = 0.75 ± 0.08
c)
1.6 < M(K⁻π⁺π⁻) < 1.8 GeV
n = 0.86 ± 0.08
d)
1.8 < M(K⁻π⁺π⁻) < 2.0 GeV
n = 0.98 ± 0.06
e)
dσ/dM_Kππ (μb/0.2GeV)
P_lab GeV/c
2441A36

Fig. 36

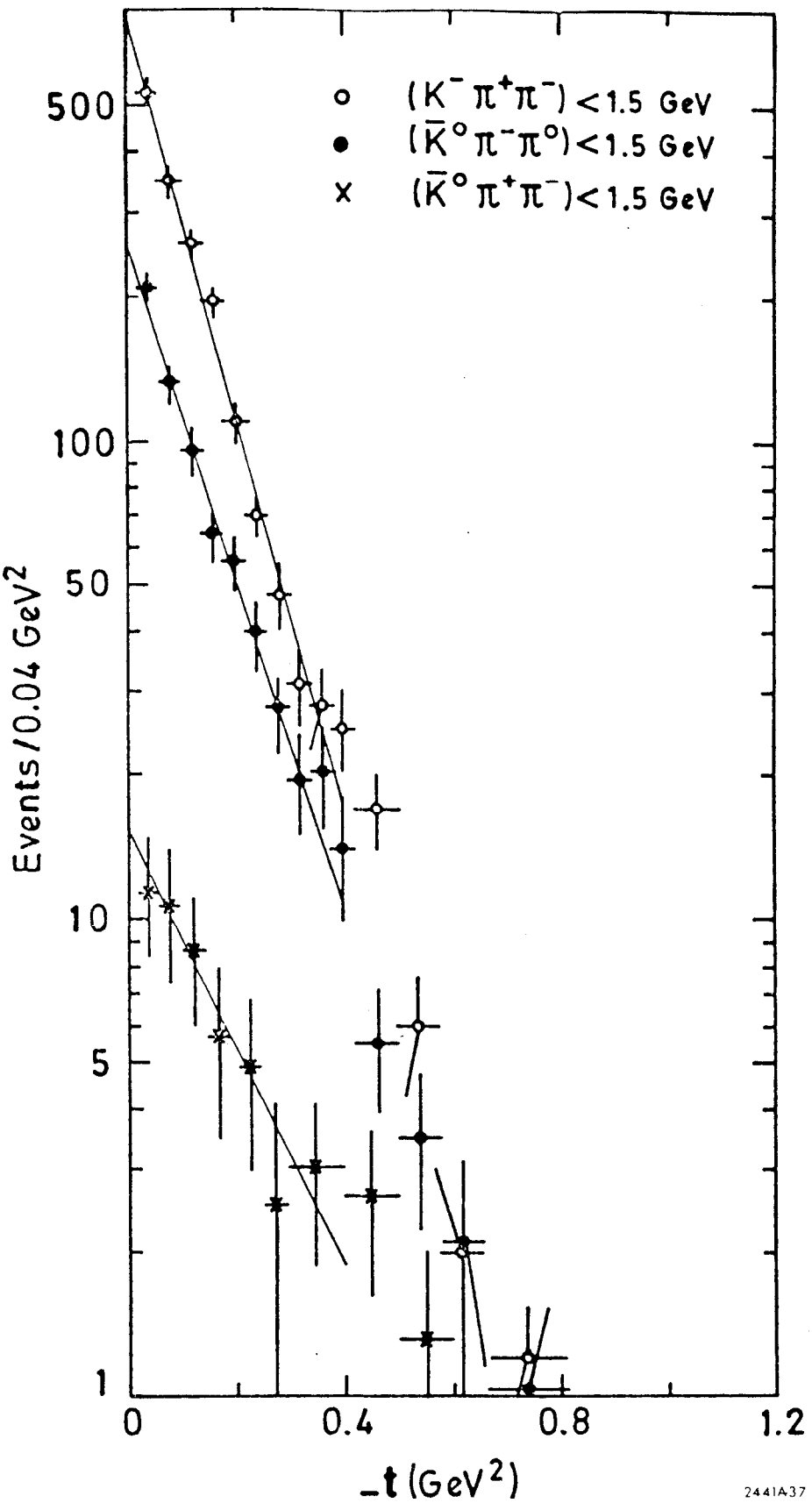
500
100
50
10
5
1
Events/0.04 GeV²
0
0.4
0.8
1.2
-t (GeV²)
(K⁻π⁺π⁻) < 1.5 GeV
(K̄°π⁻π°) < 1.5 GeV
(K̄°π⁺π⁻) < 1.5 GeV
2441A37

Fig. 37

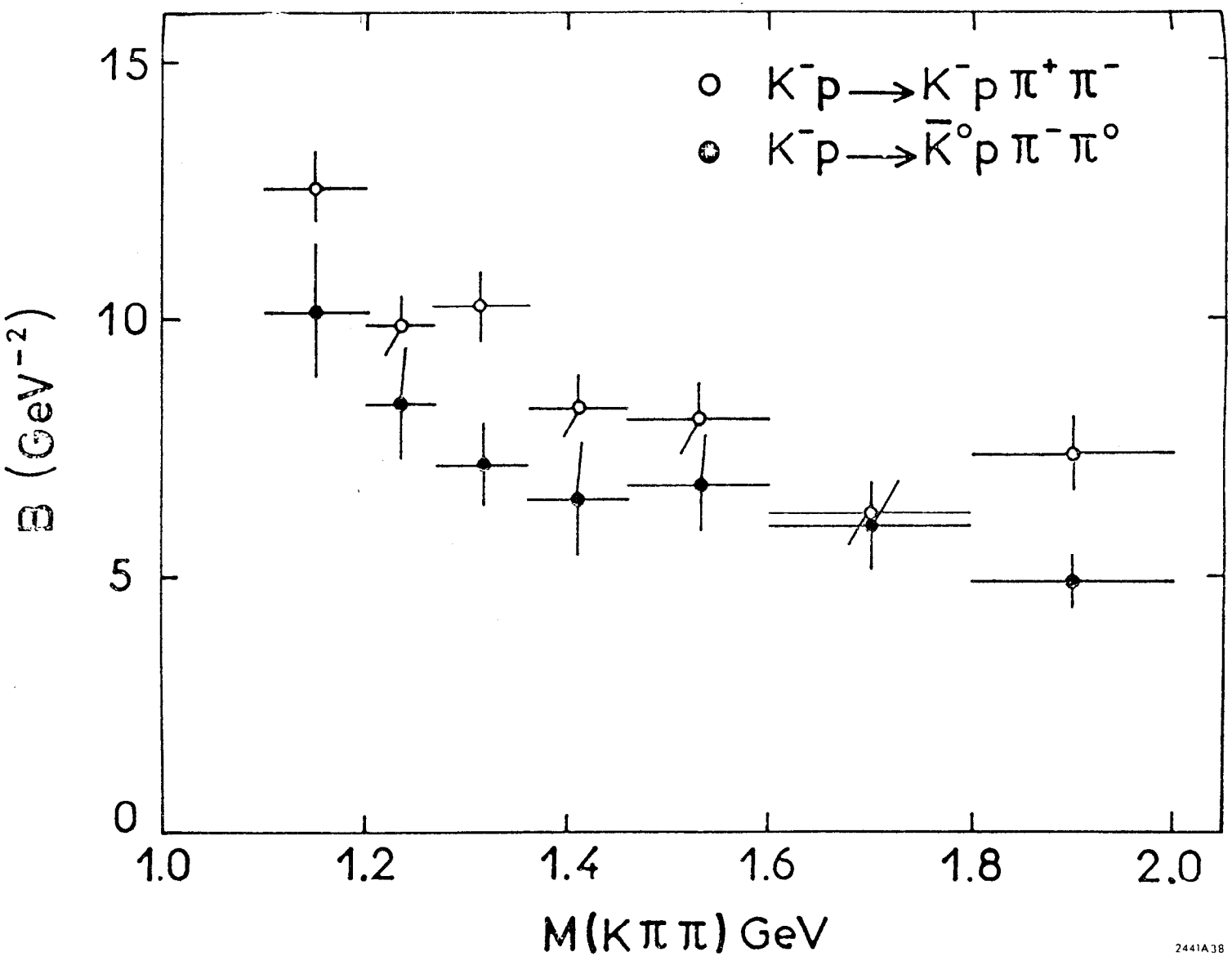
15
10
5
0
B (GeV^{-2})
1.0
1.2
1.4
1.6
1.8
2.0
M(Kππ) GeV
$K^-p \rightarrow K^-p\pi^+\pi^-$
$K^-p \rightarrow \bar{K}^0p\pi^-\pi^0$
2441A38

Fig. 38

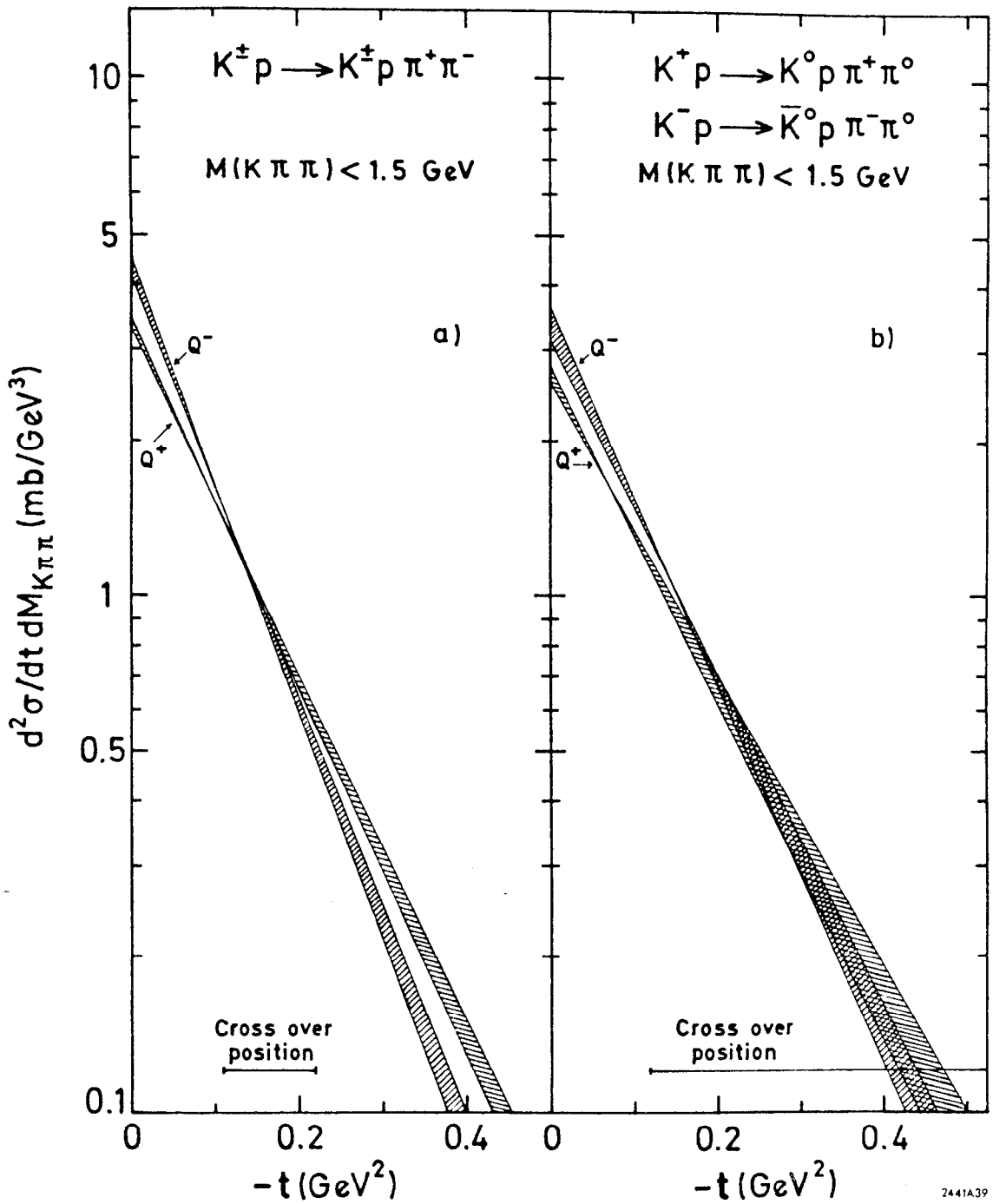
$K^{\pm}p \longrightarrow K^{\pm}p\,\pi^{+}\pi^{-}$
$M(K\pi\pi) < 1.5$ GeV
a)
Q^-
Q^+
Cross over position
$K^{+}p \longrightarrow K^{0}p\,\pi^{+}\pi^{0}$
$K^{-}p \longrightarrow \bar{K}^{0}p\,\pi^{-}\pi^{0}$
$M(K\pi\pi) < 1.5$ GeV
b)
Q^-
Q^+
Cross over position
$d^2\sigma/dt\,dM_{K\pi\pi}$ (mb/GeV^3)
10
5
1
0.5
0.1
0
0.2
0.4
$-t$ (GeV^2)
2441A39

Fig. 39

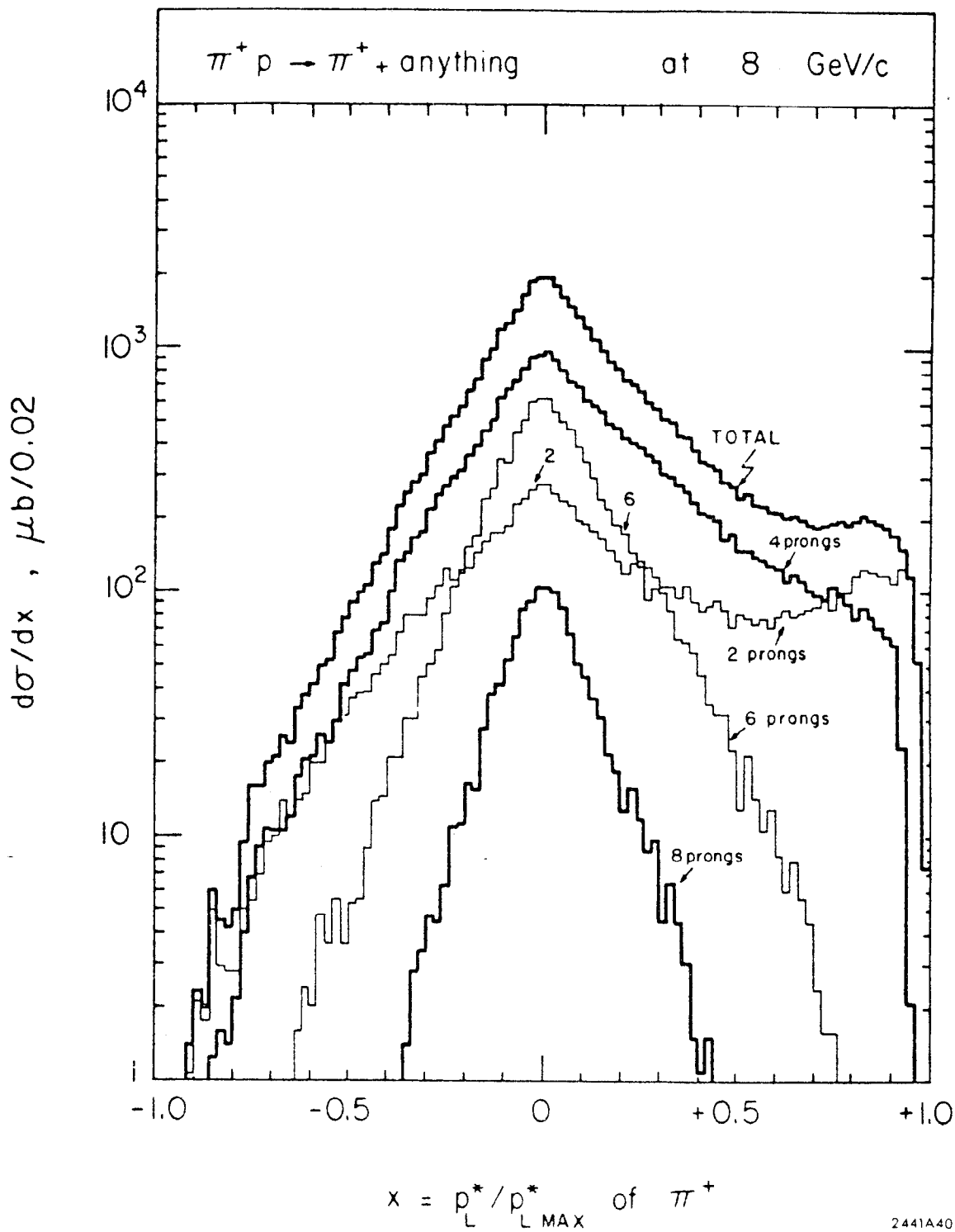
$\pi^+ p \rightarrow \pi^+ +$ anything at 8 GeV/c
10^4
10^3
10^2
10
1
$d\sigma/dx$, $\mu b/0.02$
TOTAL
2
6
4 prongs
2 prongs
6 prongs
8 prongs
-1.0
-0.5
0
+0.5
+1.0
$x = p^*_L / p^*_{L\,MAX}$ of π^+
2441A40

Fig. 40

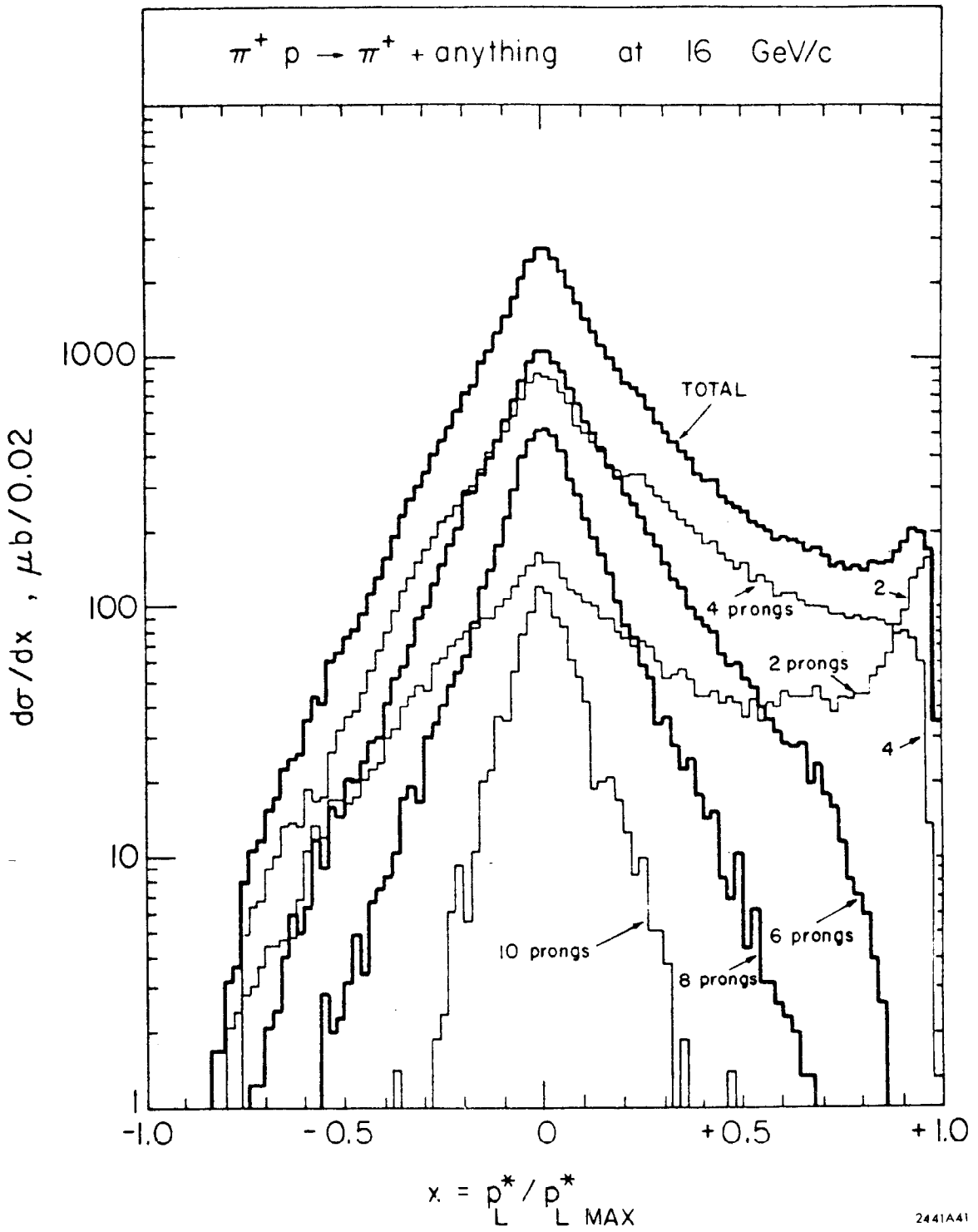
$\pi^+ p \rightarrow \pi^+$ + anything at 16 GeV/c
TOTAL
4 prongs
2
2 prongs
4
6 prongs
8 prongs
10 prongs
1000
100
10
1
-1.0
-0.5
0
+0.5
+1.0
$d\sigma/dx$, $\mu b/0.02$
$x = p_L^* / p_{L\ MAX}^*$
2441A41

Fig. 41

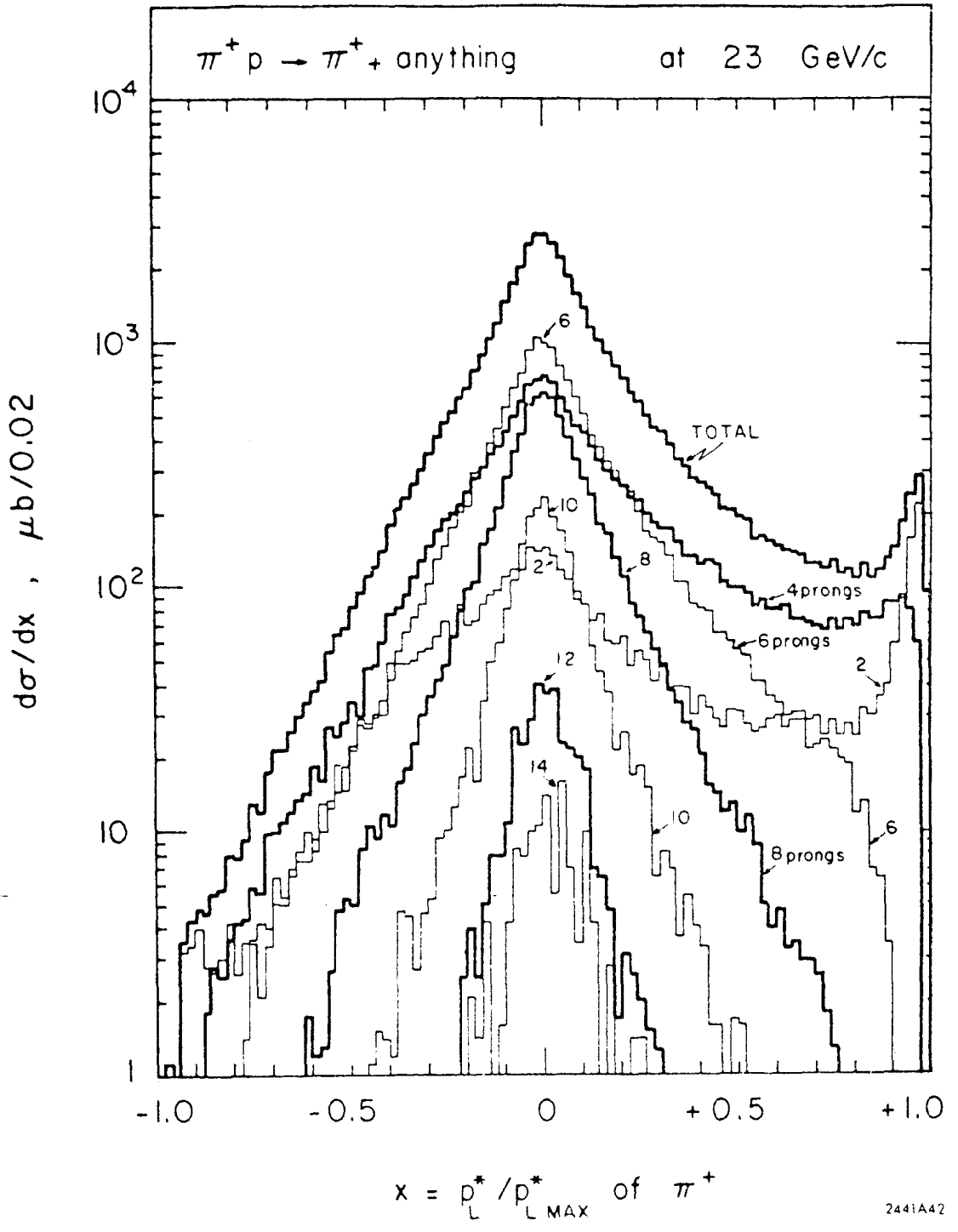
$\pi^+ p \rightarrow \pi^+ +$ anything at 23 GeV/c
10^4
10^3
10^2
10
1
$d\sigma/dx$, $\mu b/0.02$
TOTAL
4 prongs
6 prongs
8 prongs
2
6
8
10
12
14
-1.0
-0.5
0
+0.5
+1.0
$x = p_L^* / p_{L\,MAX}^*$ of π^+
2441A42

Fig. 42

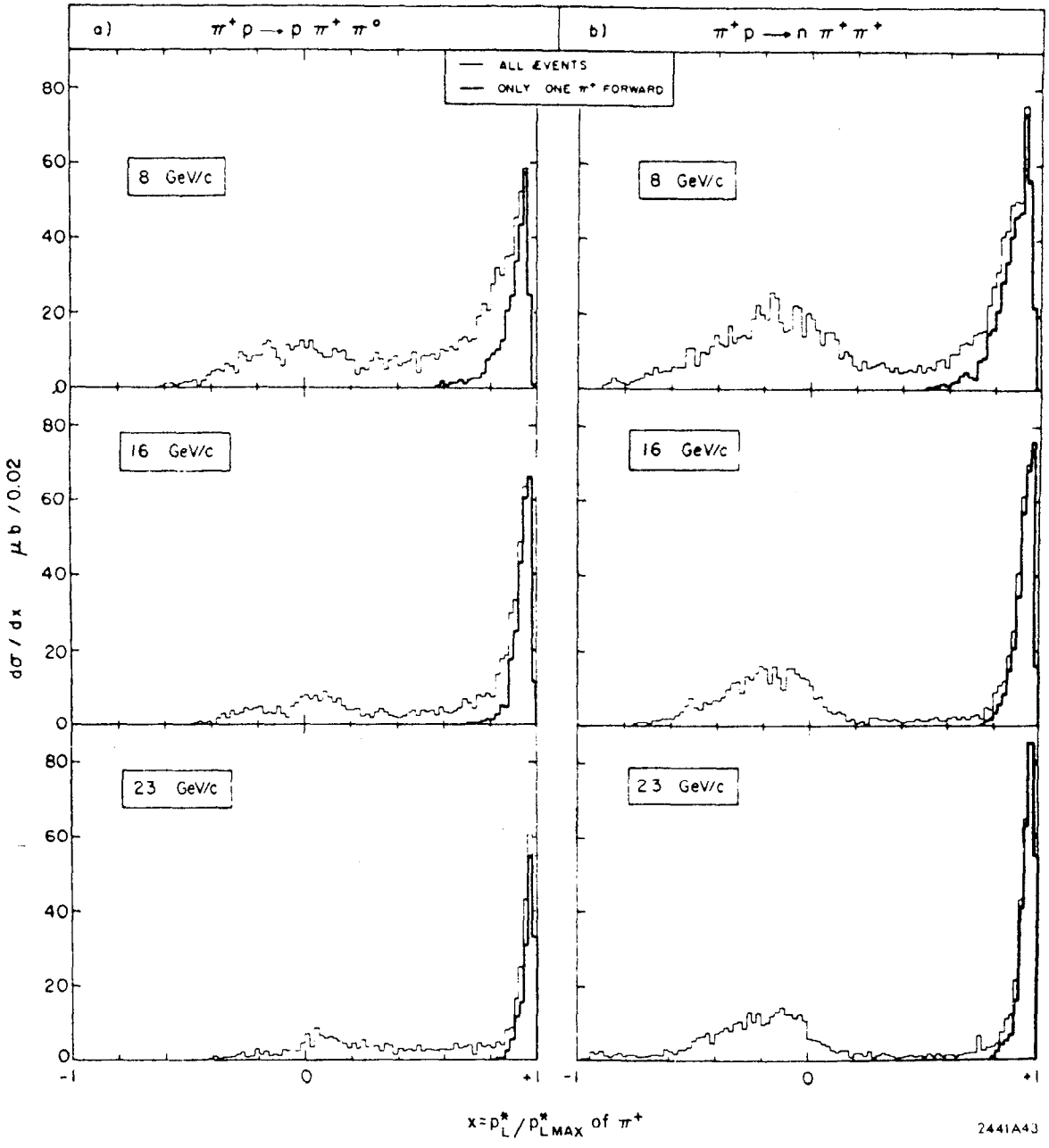
a) $\pi^+ p \rightarrow p \pi^+ \pi^0$
b) $\pi^+ p \rightarrow n \pi^+ \pi^+$
ALL EVENTS
ONLY ONE π^+ FORWARD
8 GeV/c
16 GeV/c
23 GeV/c
$d\sigma / dx$ $\mu b / 0.02$
$x = p^*_L / p^*_{LMAX}$ of π^+
2441A43

Fig. 43

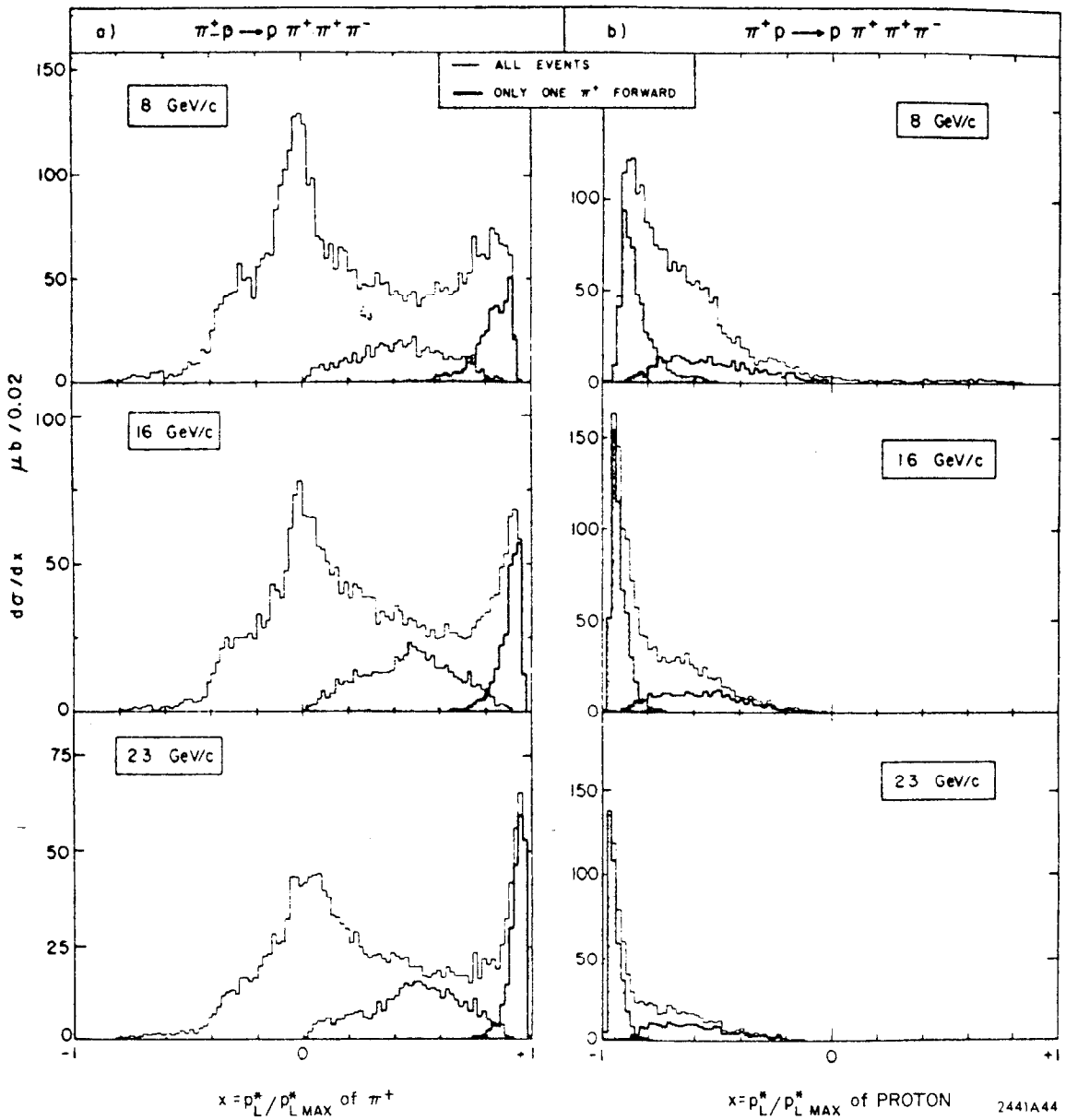
a) $\pi^{\pm}p \rightarrow p\,\pi^+\pi^+\pi^-$
b) $\pi^+p \rightarrow p\,\pi^+\pi^+\pi^-$
ALL EVENTS
ONLY ONE π^+ FORWARD
8 GeV/c
16 GeV/c
23 GeV/c
$d\sigma/dx$ $\mu b/0.02$
$x = p^*_L/p^*_{L\,MAX}$ of π^+
$x = p^*_L/p^*_{L\,MAX}$ of PROTON
2441A44

Fig. 44

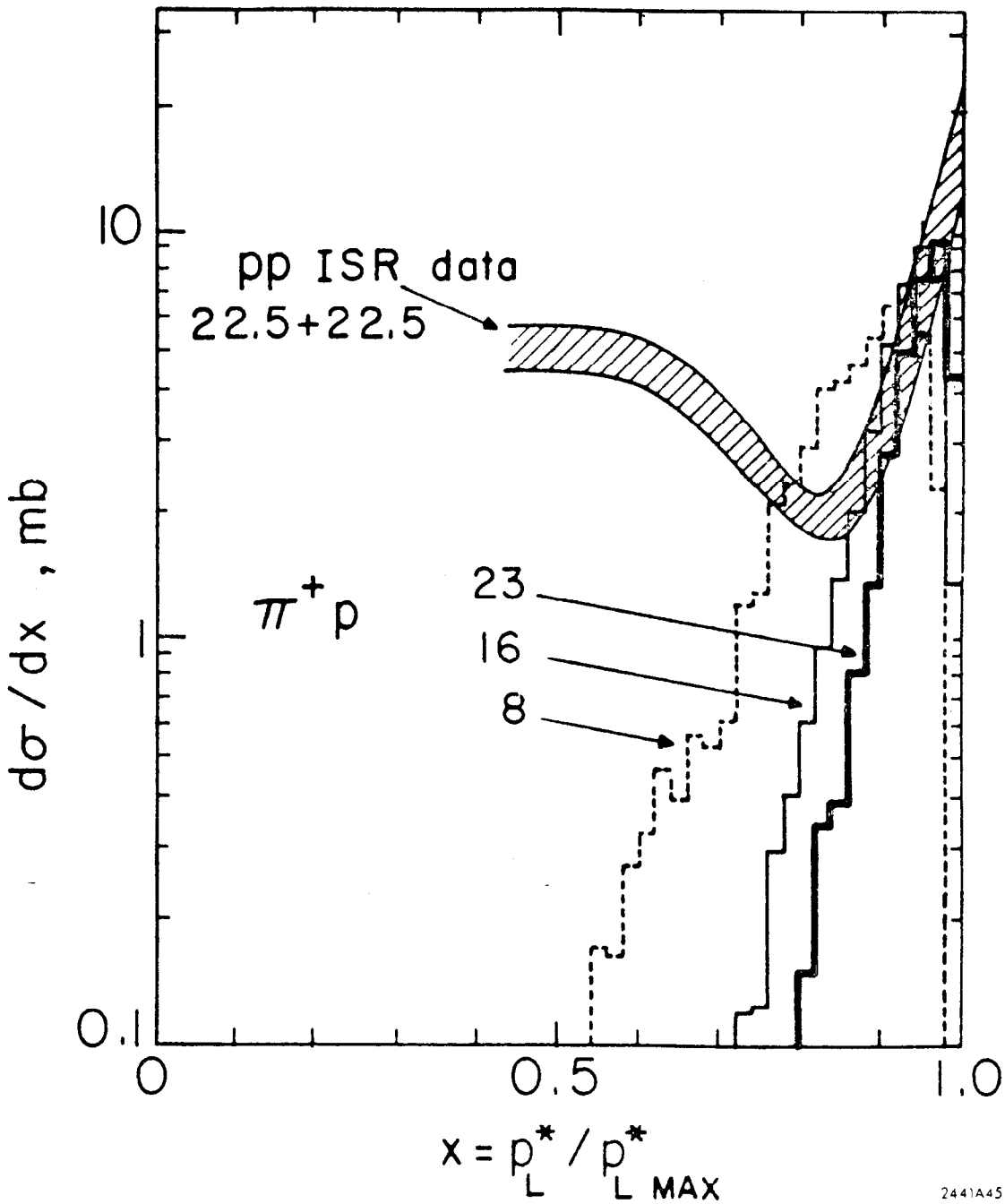
10
1
0.1
0
0.5
1.0
pp ISR data
22.5+22.5
$\pi^+ p$
23
16
8
$d\sigma/dx$, mb
$x = p_L^* / p_{L\ MAX}^*$
2441A45

Fig. 45

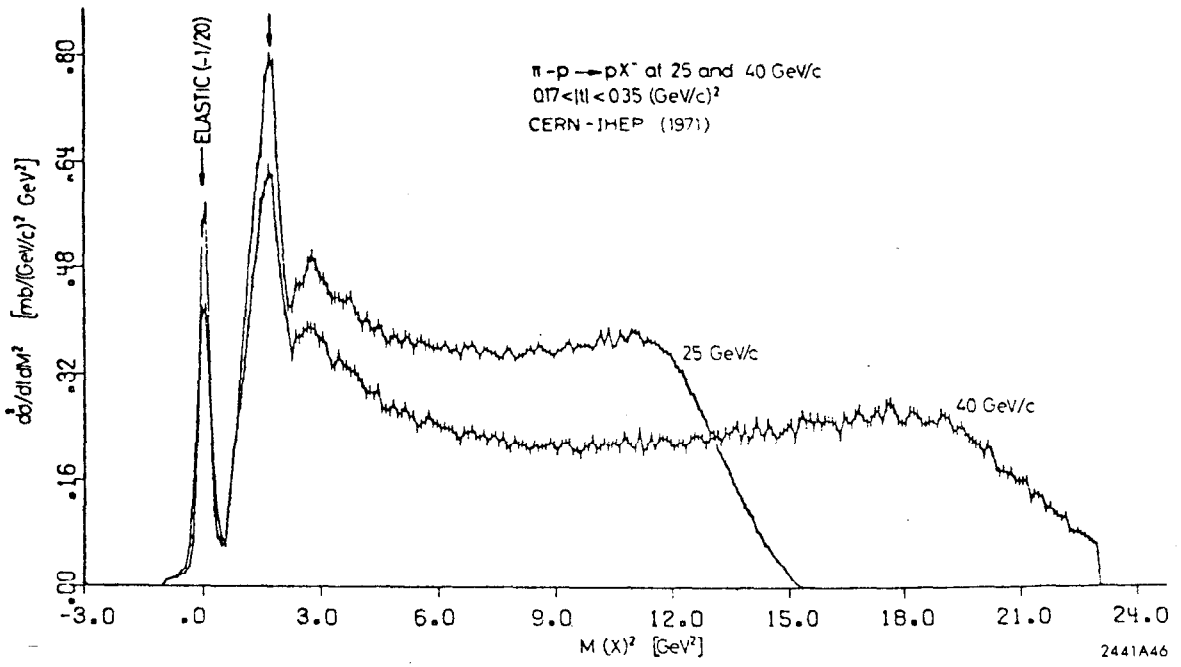
π⁻p → pX⁻ at 25 and 40 GeV/c
0.17<|t|<0.35 (GeV/c)²
CERN - IHEP (1971)
ELASTIC (-1/20)
25 GeV/c
40 GeV/c
dσ/dtdM² [mb/(GeV/c)² GeV²]
.00
.16
.32
.48
.64
.80
-3.0
.0
3.0
6.0
9.0
12.0
15.0
18.0
21.0
24.0
M (X)² [GeV²]
2441A46

Fig. 46

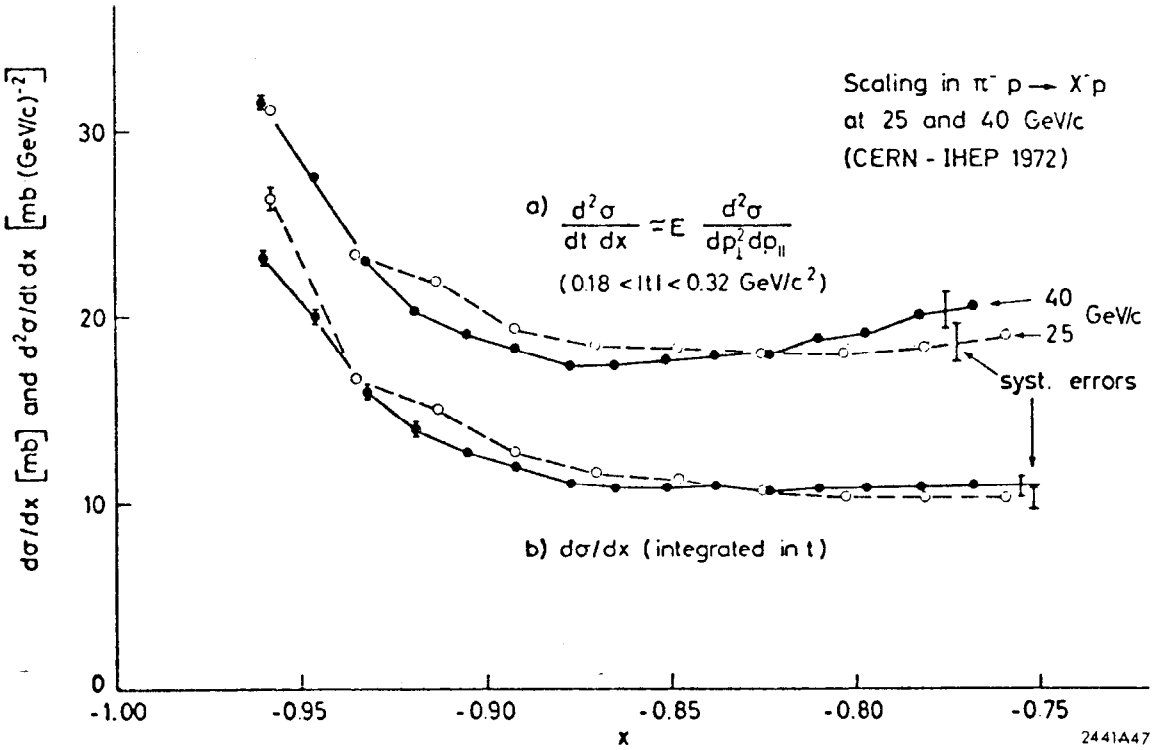
Scaling in $\pi^- p \rightarrow X^- p$
at 25 and 40 GeV/c
(CERN - IHEP 1972)
a) $\frac{d^2\sigma}{dt\,dx} \simeq E \frac{d^2\sigma}{dp_\perp^2 dp_\parallel}$
$(0.18 < |t| < 0.32\ GeV/c^2)$
40
25
GeV/c
syst. errors
b) $d\sigma/dx$ (integrated in t)
$d\sigma/dx$ [mb] and $d^2\sigma/dt\,dx$ [mb (GeV/c)$^{-2}$]
30
20
10
0
-1.00
-0.95
-0.90
-0.85
-0.80
-0.75
x
2441A47

Fig. 47

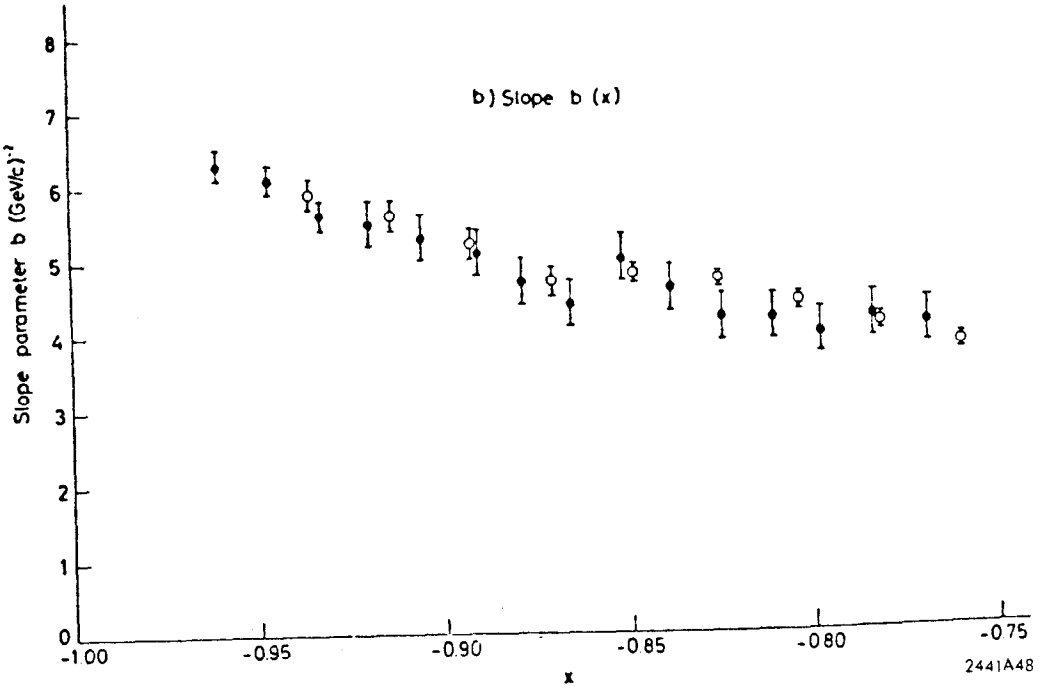
b) Slope b (x)
Slope parameter b (GeV/c)$^{-2}$
8
7
6
5
4
3
2
1
0
-1.00
-0.95
-0.90
-0.85
-0.80
-0.75
x
2441A48

Fig. 48

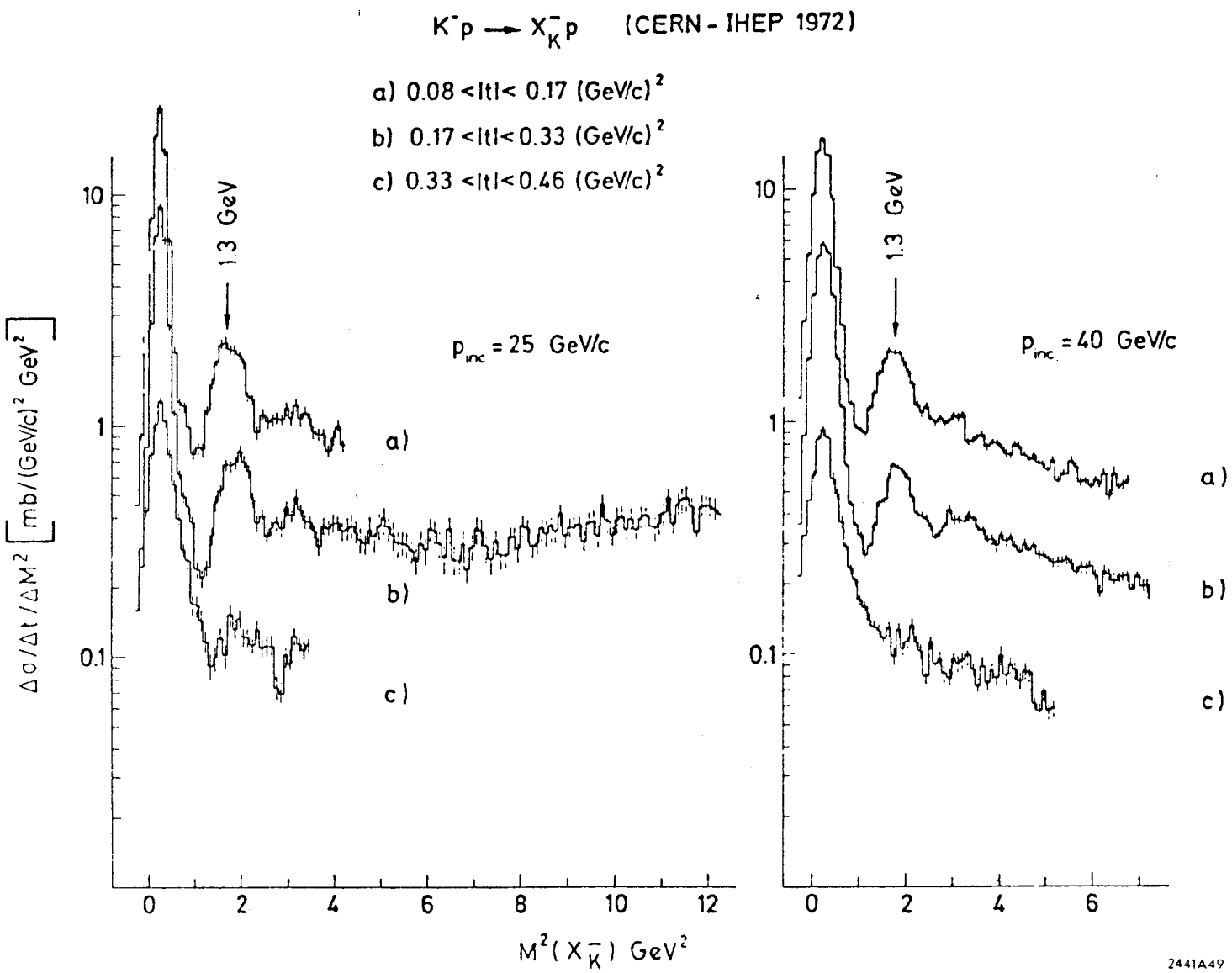
K⁻p → X⁻K p (CERN - IHEP 1972)
a) 0.08 <|t|< 0.17 (GeV/c)²
b) 0.17 <|t|< 0.33 (GeV/c)²
c) 0.33 <|t|< 0.46 (GeV/c)²
1.3 GeV
p_inc = 25 GeV/c
p_inc = 40 GeV/c
a)
b)
c)
Δσ/Δt/ΔM² [mb/(GeV/c)² GeV²]
M²(X⁻K) GeV²
2441A49

Fig. 49

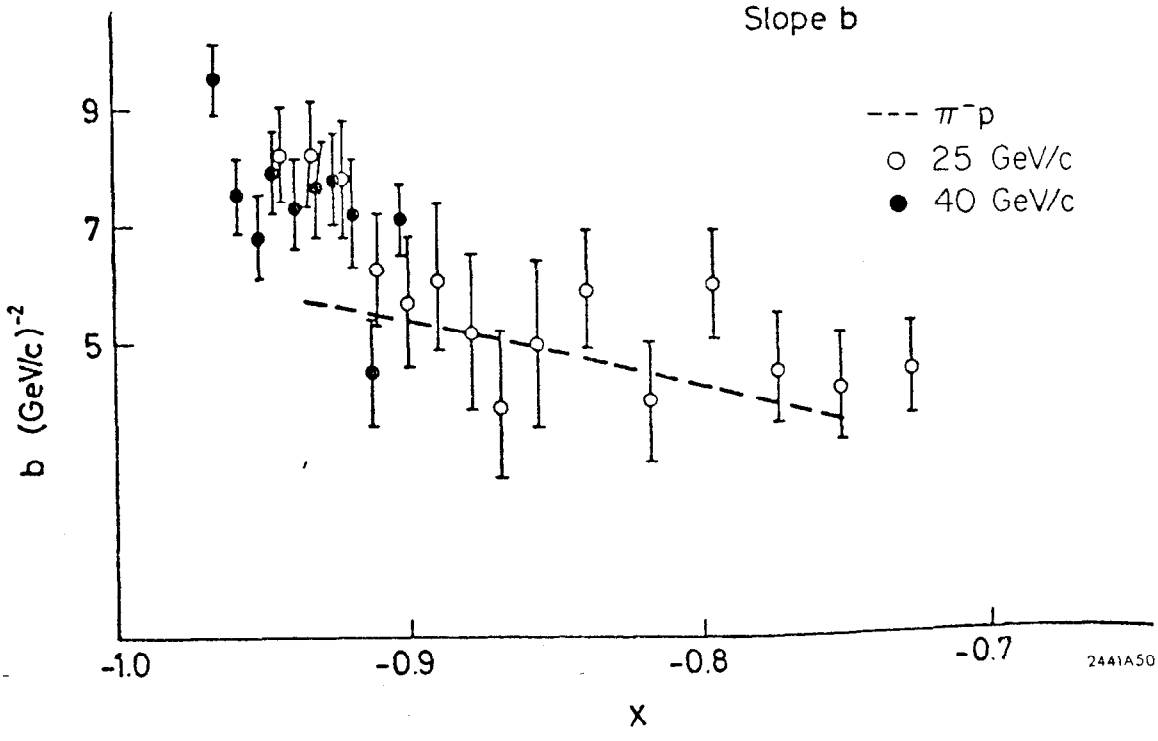

Fig. 50

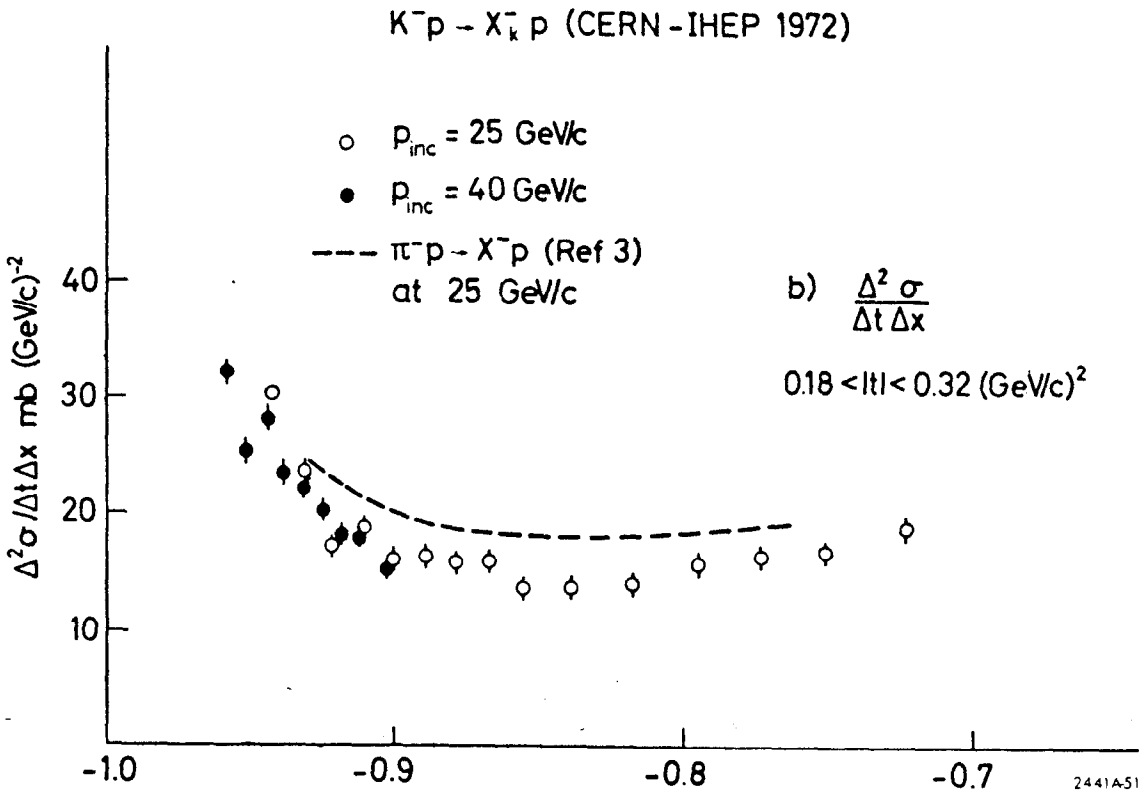
K⁻p → X⁻k p (CERN-IHEP 1972)
p_inc = 25 GeV/c
p_inc = 40 GeV/c
π⁻p → X⁻p (Ref 3)
at 25 GeV/c
b) Δ² σ / Δt Δx
0.18 < |t| < 0.32 (GeV/c)²
Δ²σ/ΔtΔx mb (GeV/c)⁻²
40
30
20
10
-1.0
-0.9
-0.8
-0.7
2441A-51

Fig. 51